Representation of individual finger movements in macaque areas AIP, F5 and M1

Dissertation

For the award of the degree

“Doctor rerum naturalium”

of the Georg-August-Universität Göttingen

within the doctoral program *Systems Neuroscience*
of the Georg-August University School of Science (GAUSS)

submitted by

Wei-An Sheng (盛維安)

from Hsinchu, Taiwan

Göttingen, 2018

Doctoral thesis committee

First reviewer:
Prof. Dr. Hansjörg Scherberger
Research Group Neurobiology
German Primate Center
Kellnerweg 4, 37077 Göttingen

Second reviewer:
Prof. Dr. Alexander Gail
Sensorimotor Group
German Primate Center
Kellnerweg 4, 37077 Göttingen

Prof. Dr. Florentin Wörgötter
Georg-August University Göttingen
Third Institute of Physics Biophysics
Friedrich-Hund-Platz 1, 37077 Göttingen

Members of the examination board

Dr. Igor Kagan
Decision and Awareness Group
German Primate Center
Kellnerweg 4, 37077 Göttingen

Prof. Dr. Ralf Heinrich
Dept. Cellular Neurobiology
Schwann-Schleiden Research Centre
Julia-Lermontowa-Weg 3, 37077 Göttingen

Prof. Dr. Julia Fischer
Cognitive Ethology
German Primate Center
Kellnerweg 4, 37077 Göttingen

Date of oral examination: June 21st, 2018

Herewith I declare that I have written this thesis independently and with no other aids and sources than quoted.

Göttingen, April 30th, 2018 Wei-An Sheng

Acknowledgments

First of all, I would like to thank my supervisor, Hans Scherberger, who gave me the opportunity to work in his laboratory in the past five years. He provided me with fascinating scientific ideas and great support ranging from theoretical background for data analyses to technical details of experimental design. I am also grateful to Alex Gail and Florentin Wörgötter for being on my thesis committee, giving constructive suggestions and criticism.

I express my thanks to Andres Toro-Agudelo, whose engineering background enhances mine, for collaborating the decoding study and numerous mathematical, programming and technical supports; to Benjamin Dann for teaching me data analysis from the very beginning and giving advice on both project and career planning; to Veera Katharina Menz, who patiently taught me as a master student without any programming experience how to use Matlab; to Rijk in 't Veld for sharing and nicely explaining his Matlab and Labview codes, and showing me animal training; to Swathi Sheshadri for mathematical and programming supports; to Stefan Schaffelhofer for sharing ideas of designing the manipulandum used in this study.
Special thanks go to Matthias Dörge for designing, building and repairing the experimental setup and Natalie Bobb for teaching, discussing and helping me with animal training. Thank you to all other former and current colleagues in the Neurobiology laboratory, to Ricarda, Sabine, Anja, Sebastian, Yves, Jonathan, Jeroen, Daniela, Anne-Do, Stefan G, and Andrej. It is my honor to work with all of you in such a nice and friendly atmosphere. Thank you, my rotation and master students, Fenja and Helge, for helping with animal training and granting me the chance to learn to teach in German.

Special thanks also go to the two monkeys I worked with, Moe and Nelson. Without their sacrifice as experimental animals, collecting valuable neural signals from non-human primates and understanding more about the motor system are not possible.
Thank you, all my former teachers, who ignited my endless fascinations in biology and initiated my devotion to science, especially Chien-Yuen Pan

(潘建源), Ling-Long Kuo-Huang (黃玲瓏), Shue-Mei Wang (王淑美), Su-Hwa Chen (陳淑華), Shih-Chung Chang (張世宗), and Chuan-Chin Chiao (焦傳金).

My thanks to Felicia and Gizem, for proofreading this thesis and all the good time spent in Göttingen discussing science, music, and other things while sharing your passion for life; to Cornelia and Christian for their hospitality as "German hosts." I would like to thank all the friends in Göttingen, in Taiwan, and around the world who cherish our friendship. The short time meeting all of you was valuable, no matter in Berlin, Oxford, Chicago or San Diego.

Finally, I thank my parents for always supporting and motivating me to pursue excellence; and Sheng-Yen, whom I am grateful to have as my companion.

Table of Contents

1. Introduction

1.1 Grasping and individuated finger movements

Our hands play a central role in our daily life. We use hands to grasp objects and manipulate them. Hand usage is also associated with various cognitive skills, like writing or playing instruments. These activities require sophisticated control of individual finger kinematics. Depending on whether fingers move simultaneously, or one finger moves relatively more than the others, hand use can be divided into two categories: grasping and individuated finger movements (Schieber and Santello, 2004).

Grasping is the major usage of the hand. During reaching, the hand starts to "preshape", so the fingers are at good positions to make contact with the surface of the object to be grasped. It is not difficult to image that a large number of natural hand shapes could be reconstructed by a few statistically identified synergies (Mason et al., 2001). The order of these synergy patterns (e.g. identified by principle components) shows a gradient of independence of individual fingers. The first few components represents the entire hand opening and closing, where the metacarpophalangeal (MCP) and proximal interphalangeal (PIP) joints (Fig. 1.1 A) of all the fingers move together (Santello et al., 1998). These observations indicate that the number of DOFs we need during natural grasping is significantly lower than the numbers of available DOFs of the hand.

The degree of finger individuation increases during manipulation of objects, for example, using chopsticks or opening a lid, but the fingers still tend to move together. Looking at more sophisticated tasks such as typing and playing piano, we understand conceptually that we press a key with a single finger, but kinematic studies showed that actually all other fingers moved simultaneously (Fish and Soechting, 1992; Engel et al., 1997). This can be explained by the fact that these tasks only require one finger to move more than the others, so the intended key can be pressed while avoiding pressing the unintended keys. Looking closer to the finger kinematics of these two tasks, movements of neighboring fingers are more highly correlated than movements of non-neighboring fingers. However, this is not

obligatory, since the correlation is weaker when one finger is pressing the key than when the subject is not intended to press any key (Fish and Soechting, 1992). This implies the neural control can actively dissociate the adjacent fingers to some extent when one must act with out the other. Researchers further quantified this dissociation in both humans and monkeys by asking subjects to move a single finger explicitly (Schieber, 1991; Häger-Ross and Schieber, 2000). Nevertheless, the motion of other fingers can't be excluded thoroughly. Among the five digits, the thumb and the index finger can move most independently in such a task, whereas the middle and ring fingers are the least independent. Overall, humans have a higher degree of finger individuation than monkeys (Schieber, 1991; Häger-Ross and Schieber, 2000).

1.2 Anatomy and physiological constrains of finger movements

The individuated finger movements are mostly contributed by the extrinsic finger muscles (Schieber, 1995). Electromyographic (EMG) activity from 13 muscles was recorded from macaque monkey performing individuated finger movements. The relationship between EMG activity and individuated finger movements was illustrated in a model (Fig. 1.1 B). Among the 13 muscles, the extensor digitorum communis (EDC), the flexor digitorum profundus (FDP) and the flexor digitorum superficialis (FDS) are the most important. The EDC straightens the index, middle, ring, and small fingers by four separated tendons (Fig. 1.1 D). These tendons primarily extend the MCP joints but also extend partially the PIP and DIP joints. At the anterior side of the forearm, both FDP and FDS have tendons insert into the tips of the index, middle, ring, and small fingers (Fig. 1.1 C). Similar to the EDC acting on the MCP, PIP and DIP joints, the FDP can bend these joints. The FDS contributes the most to the individuated movement of each finger by having independent muscle bellies for all four tendons, while the FDP only has a separate muscle belly for index finger and a common muscle belly for the other three (website of American Society for Surgery of the Hand).

Figure 1.1 Finger joints and muscles of the hand (opposite page)

A) Joints of the five fingers and the thenar muscle group (TH) of a right hand. The thumb digit has only two phalanges (bones) so it only has one interphalangeal joint (IP), which is similar to the distal interphalangeal joint (DIP) of the other four fingers. The other four fingers have four joints: distal interphalangeal joint (DIP)**,** proximal interphalangeal joint (PIP), metacarpophalangeal joint (MCP) and carpometacarpal joint (CMC). B) Model of the production of individuated finger movements by EMG activity changes (Schieber, 1995). The model is based on a task with 12 instructed movements, including flexion (f) and extension (e) of the five digits (1-5) and wrist (w). EMG activities from 13 muscles were used to construct the movements of the five digits and wrist during each of the instructed movement. Flexor digitorum profundus (FDP) was recorded from the ulnar region (FDPu) and the radial region (FDPr). C) Flexor muscles in the anterior compartment of the forearm. The superficial compartment (left) includes flexor carpi radialis (FCR), palmaris longus (PL) and flexor carpi ulnaris (FCU). Flexor digitorum superficialis (FDS) and flexor digitorum profundus (FDP) are in the intermediate and deep compartment (right). D) Extensor muscles in the posterior compartment of the forearm include extensor pollicis longus (EPL), extensor digitorum communis (EDC), extensor carpi radialis longus (ECRL), extensor carpi radialis brevis (ECRB), and extensor carpi ulnaris (ECU). Macaque muscles extensor digiti secundi et tertii (ED23) and extensor digiti quarti et quinti (ED45) are the homologues to extensor indicus proprius and extensor digiti quinti proprius (also known as extensor digiti minimi) in humans. Muscles in B) are shown as abbreviations in A, C and D (adapted from website of American Society for Surgery of the Hand).

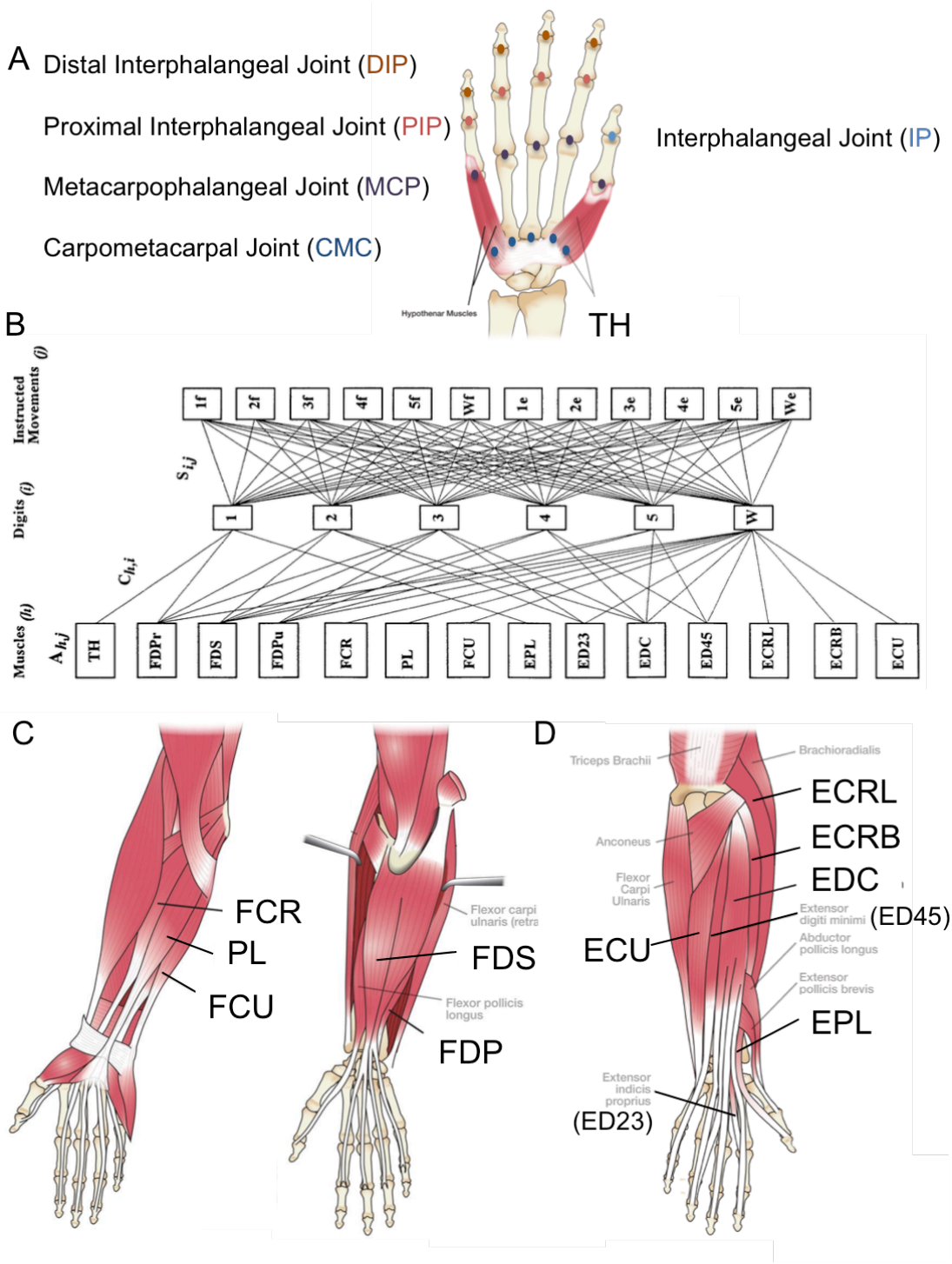

The interconnection between the tendons of the extrinsic finger muscles is an important biomechanical factor, which constrains the individuated finger movements. In macaque monkeys, these interconnections are more pronounced than in humans (Serlin and Schieber, 1993). Another potential biomechanical coupling of the multitendoned extrinsic finger muscles is the simultaneous activation

of muscle fibers from single motor units on tendons of adjacent digits. The macaque extensor digiti quarti et quinti (ED45) is an example of this category (Fig. 1.1 D), having single motor units acting on tendons of the ring and the little fingers (Schieber et al., 1997). In contrast, the human homologues muscle extensor digiti quinti proprius (also known as extensor digiti minimi) has no tendon to the ring finger and extend only the little finger.

Beyond the mechanical coupling from the multitendoned extrinsic finger muscles, there are also constrains produced by the innervation of spinal motor neuron pools. Motor units acting on different digits may be synchronized in short-term. This functional coupling can happen in the same or in different muscles (Bremner et al., 1991), and potentially cause the "spillover" of movements to the adjacent non-instructed fingers. When a subject flexes a finger, EMG activity of the FDP was not only recorded from the instructed finger, but also from adjacent fingers (Kilbreath and Gandevia, 1994; Reilly and Schieber, 2003).

The premotor neurons responsible for the synchronization described in the last paragraph could be theoretically any last-order inputs to the motor neuron pools, for example, corticomotoneuronal (CM) cells or spinal interneurons. However, evidence from a lesion study of the corticospinal system implies that cortex is the major contributor to the short-term synchronization (Datta et al., 1991). Neural activity from primary motor cortex (M1) recorded simultaneously with EMG activity shows that CM cells in this area have divergent output to the spinal motor neuron pools of several forearm and intrinsic hand muscles (Shinoda et al., 1979; Fetz and Cheney, 1980; Buys et al., 1986). In addition, CM cells can be both excitatory and inhibitory, when acting on motor neuron pools of different muscles (Cheney and Fetz, 1985; Cheney et al., 1985). The suppression is exerted via inhibitory interneurons, because M1 output neurons are excitatory. Furthermore, CM cell pairs with similar muscle fields showed greater synchronization than pairs with non-overlapping fields (Jackson et al., 2003). These are the upstream neural basis for the short-term synchronization of the spinal motor neuron pools.

Both biomechanical coupling and neural coupling limit the individuated movement of single fingers. To overcome this limitation, additional muscles are activated to

prevent the adjacent fingers from moving. For example, the extensor digiti secundi et tertii (ED23) contracts to prevent the flexion of the index and middle fingers when a monkey flexes its little finger. In Fig. 1.1 B, this is illustrated as ED23-3-5f and ED23-2-5f. In humans, the middle finger FDP contracts when extending the index or the middle finger (Reilly and Schieber, 2003).

In summary, the individuated movements of the primate digits are mainly controlled by the multitendoned extrinsic finger muscles. The mechanical coupling from the tendons and the neural coupling both constrain the fingers to move individually. Individuation is achieved by preventing the undesired fingers from moving simultaneously, and this requires a motor control which is more complex than controlling a pair of agonist and antagonist muscles (Schieber and Santello, 2004).

1.3 Individuated finger movement representation in primary motor cortex

In the past decades, the studies of finger movements in area M1 have been mainly focused on how the CM cells activate the forearm muscles (section 1.2) and the cortical territory mapping of the output cells.

The CM cells synapsing directly on the motor neurons of single muscles is a feature of primates (Porter, 1985). In humans, lesions of the corticospinal tract (CST) cuases hemiparesis, in which the voluntary movements at one side of the body are weakened and less individuated. For instance, the patient fails to move a single finger but has to move all the fingers simultaneously (Lang and Schieber, 2003). In monkeys, the weakening caused by CST lesions seems to be more transient, although the inability to perform independent finger movements was observed (Lawrence and Kuypers, 1968). Reversible inactivation of the M1 hand representation resulted in similar deficits (Kubota, 1996; Schieber and Poliakov, 1998; Brochier et al., 1999). These observations suggest that non-corticospinal descending pathways involving processing in subcortical centers can only generate more rudimentary and less individuated movements. Examples for these subcortical centers are red nucleus, the brainstem reticular formation and the gray matter of the spinal cord (Schieber, 2004).

In addition to how the CM cells innervate downstream muscles, the organization of output neurons in area M1 is another major research topic. Experimental evidence based on intracortical microstimulation (ICMS) indicates that the somatotopic arrangement for the hand and fingers in M1 is not like the iconic homunculus, which is spatially discrete and sequentially ordered (Fig. 1.2 A). The cortical regions innervating different muscles are largely overlapping (Andersen et al., 1975; Donoghue et al., 1992). At the neuronal level, single M1 neurons are tuned to multiple finger and wrist movements in monkeys (Schieber and Hibbard, 1993). From the distribution of neurons recorded during a wrist and individuated finger movement task, there is hardly any evidence of somatotopic segregation of the fingers (Fig. 1.2 B). This is also true in humans shown by magnetic resonance imaging

(fMRI), where similar cortical regions are activated during multiple digit movements (Sanes et al., 1995) (Fig. 1.2 C).

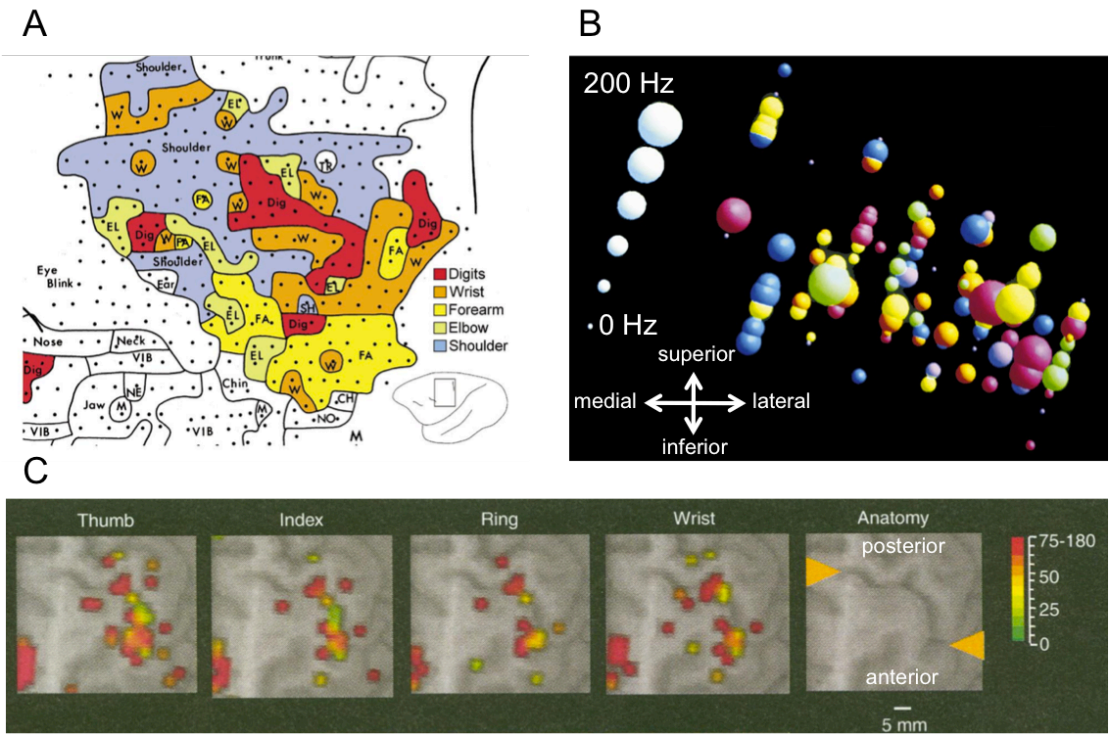

Figure 1.2 "Mosaic" maps of upper extremity and finger representation in M1

A) ICMS map of M1 in owl monkey. Black dots show stimulated points, and the lines mark boundaries of regions evoking different movements. Selected movements are marked in different colors as in the legend. Original from Gould et al., 1986 and adapted from Schieber, 2001. B) Activation pattern in M1 coronal section during multiple finger movements. The neurons are colored according to movements that they are tuned the most: thumb, red; index finger, orange; middle, yellow; ring, green; little, blue; wrist, violet. The size of a sphere represents a neuron's maximum firing rate change in Hz (adapted from Schieber and Hibbard, 1993). C) Single-slice examples of fMRI signal during repetitive finger or wrist movements of a human subject. Yellow arrowheads in the "Anatomy" panel indicate central sulcus. The color scale shows the change of signal in percentage. The view is from top of the head, with the same directions for medial and lateral as in B), while anterior is down and posterior is up (adapted from Sanes et al., 1995).

However, the level of M1 somatotopic segregation for digits is different in human than in macaque monkeys. In humans, a specific fMRI activation patterns for each finger can be found by subtracting the widespread common signal of all fingers (Beisteiner et al., 2001). Another example is observed from stroke patients, that in some patients, thumb and index finger were more affected and in other patients, it was the little and the ringer fingers (Schieber, 1999). In contrast, during partial inactivation of the M1 hand representation in monkey, adjacent fingers of the impaired fingers were not more affected than the non-adjacent ones (Schieber and

Poliakov, 1998). This somatotopic segregation in cortex and the more mechanically independent digits seem to be evolved in parallel and allow more individuated finger movements in humans than in monkeys.

Following the study of recording single neurons during finger movements, Poliakov and Schieber applied cluster analysis to search functional grouping of these neurons (Poliakov and Schieber, 1999). During the 12 movements of the finger and wrist (same as in Fig. 1.1 B), EMG activity from seven forearm muscles (nine muscles recorded in total) can be successfully grouped, while in three monkeys, only two consistent groups of neurons were found. A relatively large group where the neurons increase firing rates during most of the movements (broad field excitation), and another smaller group with neurons decreasing firing rates (broad field inhibition). Nevertheless, M1 neuronal populations do contain the information of specific finger movements. A series of studies used different algorithms to decode finger movements, including neuronal population vector analysis (Georgopoulos et al., 1999), optimal population vector, logistic regression, softmax estimator (Ben Hamed et al., 2007), and receiver operating characteristic (ROC) curves (Egan et al., 2012). These results show possible application for brain machine interface (BMI).

1.4 Sensorimotor transformation and the fronto-parietal grasping circuit

Previous studies of individuated finger movements have been mainly focused on the primary motor cortex. However, to have a more complete understanding of the neural mechanisms for controlling skilled hand actions, including finger movements, it is necessary to look at the cortical network involving different brain areas.

Visual information is important to guide the motion of the hand. We preshape our hand and fingers before grasping an object based on the shape, size and orientation of the object (Jeannerod, 1986). The process of transforming relevant visual information into a potential or planed motor action is the so called sensorimotor transformation (Janssen and Scherberger, 2015). The frontal and parietal cortices are important regions in the brain involving in this process. The visual processing for planning an action to grasp an object (prehesion) and for identifying the object (perception) seems to involve different parts of the brain. Goodale and Milner termed this two visual pathways the dorsal stream and the ventral stream (Goodale and Milner, 1992). Both starting from the primary visual cortex (V1) in the occipital lobe, the dorsal stream stretches into the parietal lobe, while the ventral stream goes through V2 and V4 to areas of the inferior temporal lobe (Fig. 1.3 A).

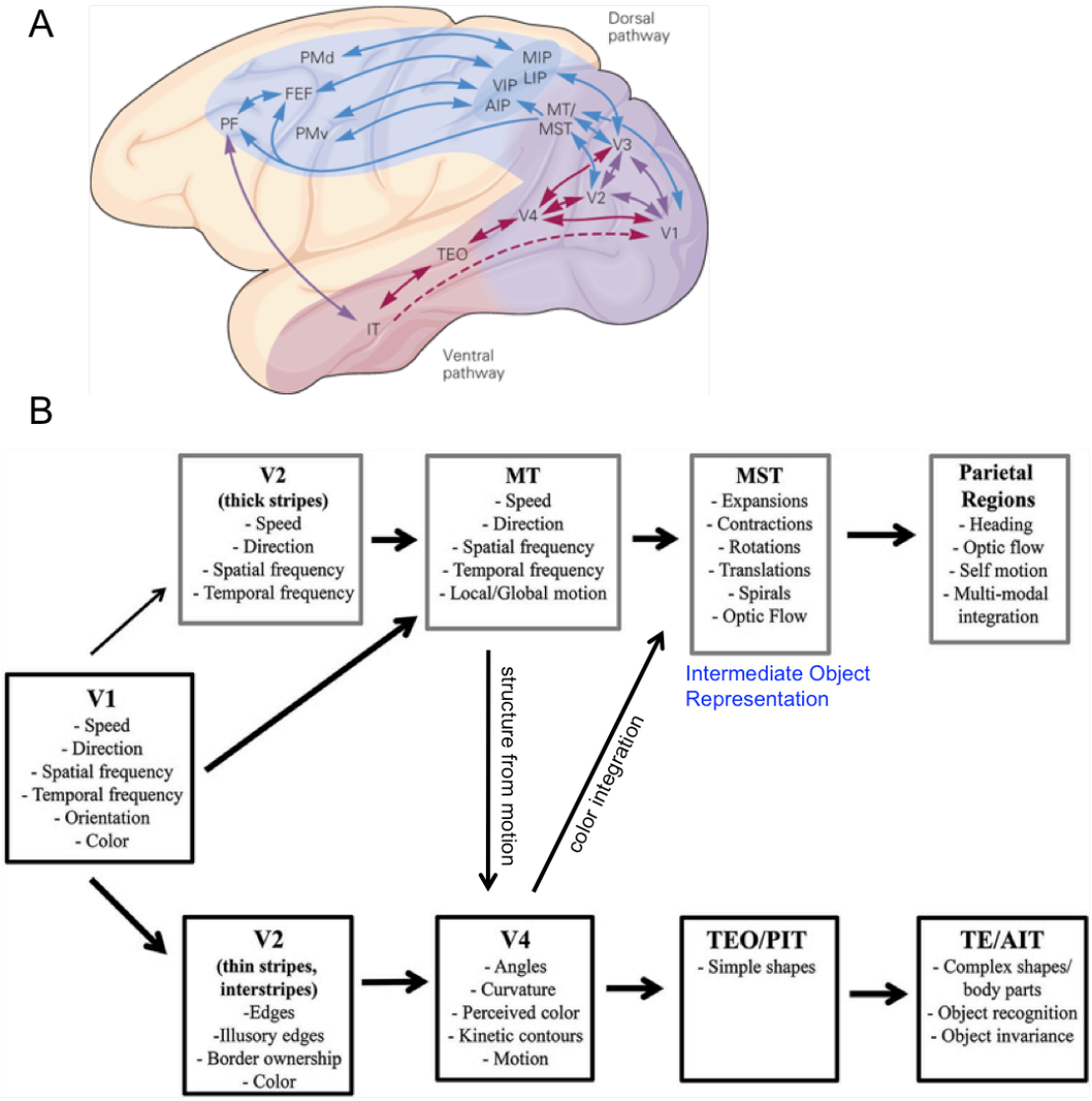

Figure 1.3 Dorsal and ventral pathways and the hierarchy of visual processing

A) Anatomical locations of the areas in the two visual pathways. AIP, anterior intraparietal cortex; FEF, frontal eye field; IT, inferior temporal cortex; LIP, lateral intraparietal cortex; MIP, medial intraparietal cortex; MST, medial superior temporal cortex; MT, middle temporal cortex; PF, prefrontal cortex; PMd, dorsal premotor cortex; PMv, ventral premtor cortex; TEO, posterior inferior temporal cortex, VIP, ventral intraparietal cortex; V1, V1, V3, V4, primary, secondary, third, and fourth visual areas (adapted from Kandel et al., 2013). B) Visual features processed in the visual hierarchy. Gray boxes (top) depict select visual features processed along the dorsal pathway and black boxes (bottom) depict the ones along the ventral pathway. A hypothetical "intermediate object representation" stage is proposed in area MST of the dorsal pathway. TEO/PIT, posterior inferior temporal cortex; TE/AIT, anterior inferior temporal cortex (adapted from Perry and Fallah, 2014).

The functional differences of the dorsal and ventral pathways (visually guided behavior vs. object recognition) can be explained by the different visual features processed in the two pathways (Norman, 2003). The ventral stream is mainly focusing on processing colors and structure details of images (Komatsu and Ideura, 1993), while the major task for the dorsal stream is to detect motion (Maunsell and

Van Essen, 1983). However, there are cross-talks between the two systems, suggested by the object representation (selectivities for orientation, shape and size) in the parietal regions of the dorsal pathway (Murata et al., 2000; Fattori et al., 2005; 2012; Romero et al., 2014), as well as anatomical evidence (Borra et al., 2008). Fig. 1.3 B summarizes the visual features processed in major areas of the two streams with a hypothetical "intermediate object representation" stage integrating information from the ventral stream to the dorsal stream (Perry and Fallah, 2014).

At the end of the dorsal stream, in the parietal and frontal cortices, three putative specialized visuomotor functions are identified. First, lateral intraparietal area (LIP) and frontal eye field (FEF) for saccadic eye movements. Second, parietal reach region (Batista et al., 1999) and dorsal premotor area (PMd) for reach movements. Third, anterior intraparietal area (AIP) and ventral premotor area (PMv) F5 for grasping movements (Fig. 1.3 A) (Luppino and Rizzolatti, 2000; Rizzolatti and Luppino, 2001). Anatomical connections were mapped using high-resolution [^{14}C]-deoxyglucose radiography when monkeys were performing reach-to-grasp tasks (Evangeliou et al., 2009). Area V6A and AIP are identified as hubs in the parietal cortex. The connections are summarized in Fig. 1.4 (Davare et al., 2011). AIP receives inputs from the dorsal stream (purple), including PF, PFG, and PG of the inferior parietal lobule (IPL) and LIP in the intraparietal sulcus (IPS), as well as from the ventral stream (green), including secondary somatosensory cortex (SII), inferior temporal areas TE and TEO. In the center of this anatomical map, the reciprocally connected areas AIP and F5 (Luppino et al., 1999) form the dorsolateral grasping circuit (red) together with M1.

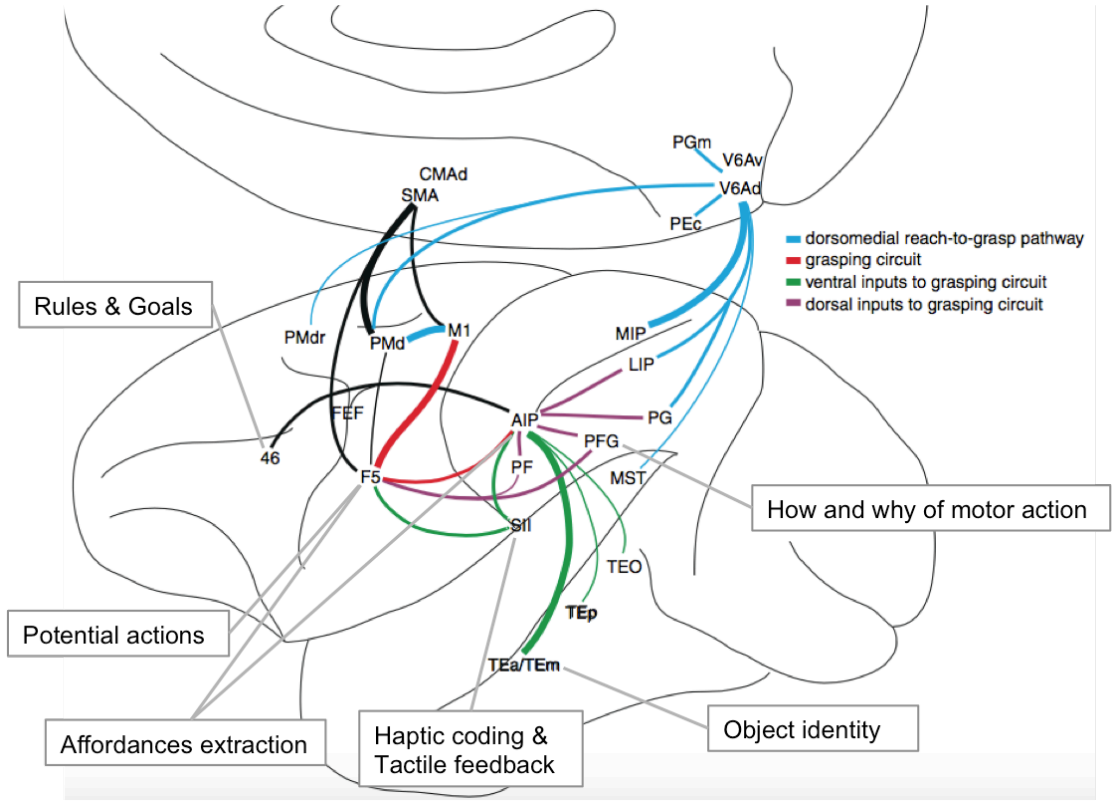

Figure 1.4 Anatomical connections of the cortical grasping network and possible contribution of each node to the generation of hand action

Anatomical connections of areas V6A and AIP based on tract tracing in non-human primates. Area V6A is the hub of the dorsomedial reach-to-grasp pathway (blue). AIP is the area in the dorsolateral grasping circuit (red), receiving inputs from both ventral stream (green) and dorsal stream (purple). Possible contributions indicated in the text boxes are adapted from the "lateral grasping network" (Borra et al., 2017). AIP, anterior intraparietal cortex; LIP, lateral intraparietal cortex; MIP, medial intraparietal cortex; MST, medial superior temporal cortex; PEc and PGm, mesial parietal areas; PF, PFG, PG, inferior parietal areas; PMd, PMdr, dorsal premotor cortex; SII, secondary somatosensory cortex; TEa/TEm, TEp, TEO inferior temporal areas (original from Grafton, 2010 and color labeled from Davare et al., 2011).

Area AIP was originally defined by Sakata and colleagues (Taira et al., 1990). Hand-related AIP neurons were classified into "motor-dominant neurons", "visual and motor neurons" and "visual-dominant neurons", based on their discharge in light and darkness (Taira et al., 1990; Sakata et al., 1995; Murata et al., 1996; 2000). According to visual response, AIP neurons can be classified into object- and non-object type (Murata et al., 2000). Object type neurons activate as soon as an object becomes visible, and this response is earlier than in area F5 (Schaffelhofer and Scherberger, 2016). These neurons show selectivity for common geometric features shared by similar objects, suggesting involvement in coding physical properties of the objects (Sakata et al., 1995; Murata et al., 2000; Schaffelhofer and Scherberger,

2016), including 3D information defined by binocular disparity (Srivastava et al., 2009; Romero et al., 2013; Theys et al., 2013). As a target of the dorsal visual stream, AIP is dedicated to the analysis of the object's intrinsic properties (size, shape, orientation) and finalized to the extraction of object affordances, ultimately mediated by the AIP-F5 circuit (Janssen and Scherberger, 2015).

Area F5 in the rostral part of the PMv consists of multiple sectors (Belmalih et al., 2009; Gerbella et al., 2011): F5a and F5p located at different antero-posterior levels of the posterior bank of the inferior arcuate sulcus, and F5c on the convexity. F5p neurons are mostly hand related (Fluet et al., 2010; Maranesi et al., 2012; Theys et al., 2012; 2013) and ICMS effectively evoke hand movements at relatively low current thresholds (Maranesi et al., 2012). Among the three sectors, only F5p have connections to the M1 hand area and to the cervical spinal cord (Borra et al., 2010; Gerbella et al., 2011). In contrast, F5a is strongly connected to prefrontal areas and AIP (Gerbella et al., 2011). 3-D-shape-selectivity and visual-dominance (more active in the light) are unique features of the sector (Theys et al., 2012). F5c neurons represent mouth or hand and mouth motor acts (Maranesi et al., 2012) and are known for mirror-neuron activity (Umilta et al., 2001). Based on the motor representation and the connectivity with the M1 hand area, F5p could be the most involved sector of putting hand movement into action (Borra et al., 2017). Similar to AIP, hand related neurons were also classified into "motor-neurons" (active during motor execution) and "visual and motor neurons" (active during both object presentation and movement), based on electrophysiological studies (Murata et al., 1997; Raos et al., 2006). Furthermore, many hand-grasping neurons are tuned for specific hand configurations (Rizzolatti et al., 1988; Fluet et al., 2010; Schaffelhofer and Scherberger, 2016) and it is suggested that F5 stores the "vocabulary" of motor prototypes (Rizzolatti and Luppino, 2001).

Summarizing the electrophysiological studies in area AIP and F5, both areas are active during visual fixation and manipulation of objects (Murata et al., 1997; 2000), and the neurons maintain active during the delay period between object presentation and movement onset, independent of the lighting condition during the grasped (Murata et al., 1996; Baumann et al., 2009; Fluet et al., 2010). The hand failed to preshape during grasping, when the two areas are reversibly inactivated

with muscimol (Gallese et al., 1994; Fogassi et al., 2001). These similarities suggest a graded representation and transformation of neuronal information across the areas, where area AIP is more visual-related and area F5 is more movement-related.

As mentioned in section 1.3, M1 plays a fundamental role in controlling dexterous hand actions. However, M1 might have a role in motor control more complex than the emission of signals driving muscle activity. There is evidence that M1 neurons are not necessarily coactivated with limb muscles, for example, during BMI control (Schieber, 2011). M1 activity can also be associated with the direction of movements (Kakei et al., 1999) or reflecting the goal of a motor act (Umilta et al., 2008; Bonini et al., 2011).

Together with PFG area of the IPL convexity encoding information about "how" and "why" of the motor action (Bonini et al., 2012), ventral area 46 in the prefrontal cortex is involved in applying behavioral rules for context-dependent action selection (Hoshi et al., 1998; Murray et al., 2000; Wallis et al., 2001), and secondary somatosensory cortex (SII) is encoding tactile and proprioceptive information for grasping (Fitzgerald et al., 2004),

Borra and colleges proposed an extended model "lateral grasping network" centered on the parieto-frontal grasping circuit (Fig. 1.4 Borra et al., 2017). The sensorimotor transformation for grasping is a complex process and involves large numbers of brain areas. Network models based on anatomy and electrophysiology, as well as computational models (Fagg and Arbib, 1998) shed light on the cortical mechanisms of object oriented hand actions and push forward future research to delineate the roles of each area involved.

1.5 Beyond the neuron doctrine

After viewing how the brain areas, particularly the fronto-parietal grasping circuit, control hand and finger movements, I would like to discuss how the neurons encode information. Does one neuron contain unique information, for example, corresponding to a specific stimulus or activation of a muscle? Do the neurons code information only at a population level, and looking at discharge patterns of single neurons could be sometimes misleading?

To answer this question, it is worthy to review the history of neuroscience. Following Virchow's cell theory (Wilson, 1947), Cajal and Sherrington enunciated the neuron doctrine. Based on Golgi's staining technique, a clearer picture of individual neuronal bodies, axons and dendrites was revealed. Cajal then proposed the individual neurons as the unit structure of the nervous system (Kandel et al., 2013). Sherrington, who originally described the skin receptive field eliciting a scratch reflex (Sherrington, 1906), hypothesized the functional roles of the individual neurons. The neuron doctrine has been dominating the field of neuroscience until today.

Using microelectrodes to record from single cells actually reinforced the study of individual neuron properties. The most representative microelectrode is the tungsten microelectrode developed by Hubel and this enabled the recording from behaving animals (Hubel, 1957). Together with Wiesel, they mapped the excitatory patterns in the primary visual cortex (V1), which led to the discovery of visual receptive fields (Hubel and Wiesel, 1962). In addition, they found that neuronal responses systematically varied with the orientation of the presented stimulus, which later defined the tuning of neurons. According to these properties of single neurons, the firing rate of each neuron is described as a function of correlation with various parameters. Tuning is defined as a systematic modulation of a neuron in relation to the systematic variation of a perceptual, cognitive or behavioral parameter. The concept of receptive field and neuronal tuning became the cornerstone of the "representational framework" (Buzsáki, 2010). These successes crystallized the idea that in addition to anatomical and functional units, single neurons could be also perceptual units (Barlow, 1972). If this is true, at the top of the

visual hierarchy, there should be single neurons responsible for the perception of individual persons. Indeed, recent studies found individual neurons in the temporal cortex responding to pictures of faces (Freiwald et al., 2009). In addition to the visual system, the representational framework can also describe neuronal activity related to movements. Neurons in M1, PMd and PRR were tuned for the reach directions while monkeys performed a center out reaching task (Fig. 1.4 A) (Georgopoulos et al., 1982; Buneo et al., 2002; Rajalingham and Musallam, 2017).

However, the neuron doctrine and the representational framework do have limitations. For example, the concept of receptive fields could oversimplify what is encoded in a neuron. Responding to a particular stimulus might not be the only function of that neuron (Yuste, 2015). The timing of the response and the ensemble of neurons responding simultaneously can be also important. Indeed, neurons in mouse visual cortex have been found not responding to identical stimuli in the same manner (Ko et al., 2011). On the other hand, regarding face neurons as one of the strongest example supporting neurons as perceptual units, there is a criticism, which is difficult to defend against: If there was only one particular neuron coding for a particular person, how would it be possible that the investigators found this neuron out of an area containing hundreds of thousands of neurons.

In the motor system, modern approaches using multiple parameters (including position, velocity, acceleration etc.) to model the firing patterns of individual neurons only coarsely matched the observed response (Todorov, 2000). Vice versa, it was not possible to classify firing patterns of individual neurons during finger movements into functional groups corresponding to the experimentally designed kinematic parameters (i.e. flexion and extension of the finger, Fig. 1.4 B) (Poliakov and Schieber, 1999), one of the most relevant examples to the topic of this thesis. A common problem of the representational framework is that tuning analysis of single neurons only explain a fraction of recorded neuron (often described in percentages as in cited studies), and leaves a large proportion of neuronal variance unexplained. Thus, the concept of the neuron doctrine and the representational frame work focusing on single neurons should be reconsidered, and more attention should be moved to groups of neurons working as a circuit (Buzsáki, 2010).

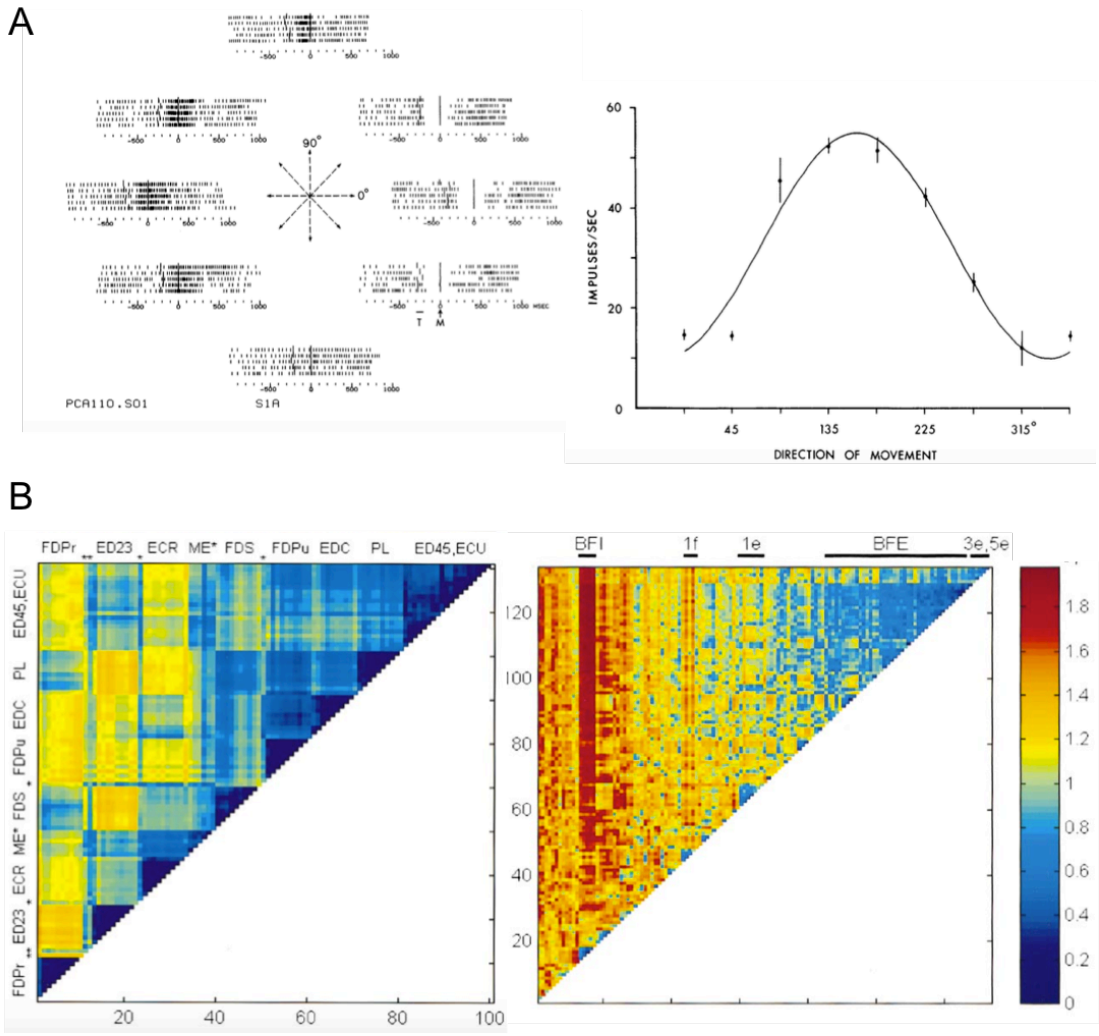

Figure 1.5 Examples from the motor system describing neuron function under the "representational framework"

A) Firing rate variation of a motor cortical cell with the direction of movement. Left: Raster plots are aligned at the movement onset (M). Center diagram indicates the eight movement directions. Right: Directional tuning curve of the same cell based on the entire trial period, similar to the tuning curve in the visual system (adapted from Georgopoulos et al., 1982). B) Functional grouping of EMG and neuronal signals during individuated finger movements. Left: Similarity matrix of clustering EMG activity and neural activity from microelectrode recordings (ME). The abbreviations for the muscles are the same as in Fig. 1.1. The clustering process reordered the recordings based on similarity of activity patterns, and the similarity is measured by distance between recording pairs (presented using the color scale at the right). Right: Similarity matrix of clustering the neuronal population. Horizontal black bars on the top indicate groups identified (see section 1.3 for details) (adapted from Poliakov and Schieber, 1999).

The idea of neural circuits is not new. Cajal's follower Lorente de No already thought about the idea of recurrent connectivity in the nervous system and observed that

neuronal activity could be prolonged after stimulus offset (functional reverberations). Based on this, Hebb coined the idea of “cell assembly”, describing neurons working as a network and the sequence of activations plays a crucial role for the functional aspect of the assembly (Hebb, 1949). Unlike other organs in the body, such as kidney or lung, that the function of a single cell can well represent the function of the organ, the function of the brain is based on interactions between the neurons. To understand the function of a cortical area, one may need to at least record from a population of neurons and look at properties of this circuit (Yuste, 2015).

How the neural circuits generate emergent function is fascinating, but without the technique to record multiple neurons in parallel, this can not be proven experimentally. The optical recording by calcium imaging (Grynkiewicz et al., 1985) with two-photon microscopy (Denk et al., 1990) and the electrical recording by multi-electrode arrays (Nicolelis et al., 2003; Buzsáki, 2004) are major technical developments for multineuronal recordings. The most widely used implantable multi-electrode array is the 100-channel Utah array (Nordhausen et al., 1996; Rousche and Normann, 1998). The later developed floating arrays avoided the relative movements between the electrodes and the brain, thus increased the longevity of chronic implants (Musallam et al., 2007).

1.6 Population analysis and dimensionality reduction

Multi-electrode arrays enable the collection of neuronal data covering the neural networks, however, the nned to analyze this large amount of data creates new challenges (Sejnowski et al., 2014). The goal is to condense these massive datasets into simplifying principles about population activity. Dimensionality reduction fulfills this goal by compressing high-dimensional signals into a set of principle variables, while preserving or highlighting features subjectively decided by the user.

Dimensionality reduction can be applied when one suspects that there is redundancy in the data, and the measured variables are not fully "independent". Dimensionality reduction helps to find the "informative variables" in the data, and these variables are also called "latent variables" because they are not observed in the first place. In the case of neuronal population, the number of recorded neurons is often considered as the number of measured variables. Since the neurons work as an ensemble and are often reciprocally connected, there is likely redundancy in their discharge patterns, and a number of latent variables, which is fewer than the number of neurons could summarize the activity of the circuit.

Consider a case with three neurons (r_1, r_2 and r_3). Traditionally, one plots the change of firing rates over time and the three neurons are represented in separate plots. In order to illustrate the neuronal population activity, one can plot the firing rates of the three neurons against each other on three axes, instead of plotting the change over time (Fig. 1.6 A). In this frame work, each time point t consist of three firing rate values from the three neurons [$r_1(t)$, $r_2(t)$, $r_3(t)$], and is represented as a single point in the three-dimensional space. Change of firing rates over time of the three neurons can be seen as a trajectory traveling through the space. Dimensionality reduction searches for a space with lower dimensions that could still explain the data to a desired extent. In this example, the population activity lies in a plane and two latent variables (s_1 and s_2) can already well describe the activity of the three neurons. The activity that is outside of the plane and not captured by the two latent variables is often considered as noise, and the dimensionality reduction is used as a denoising procedure.

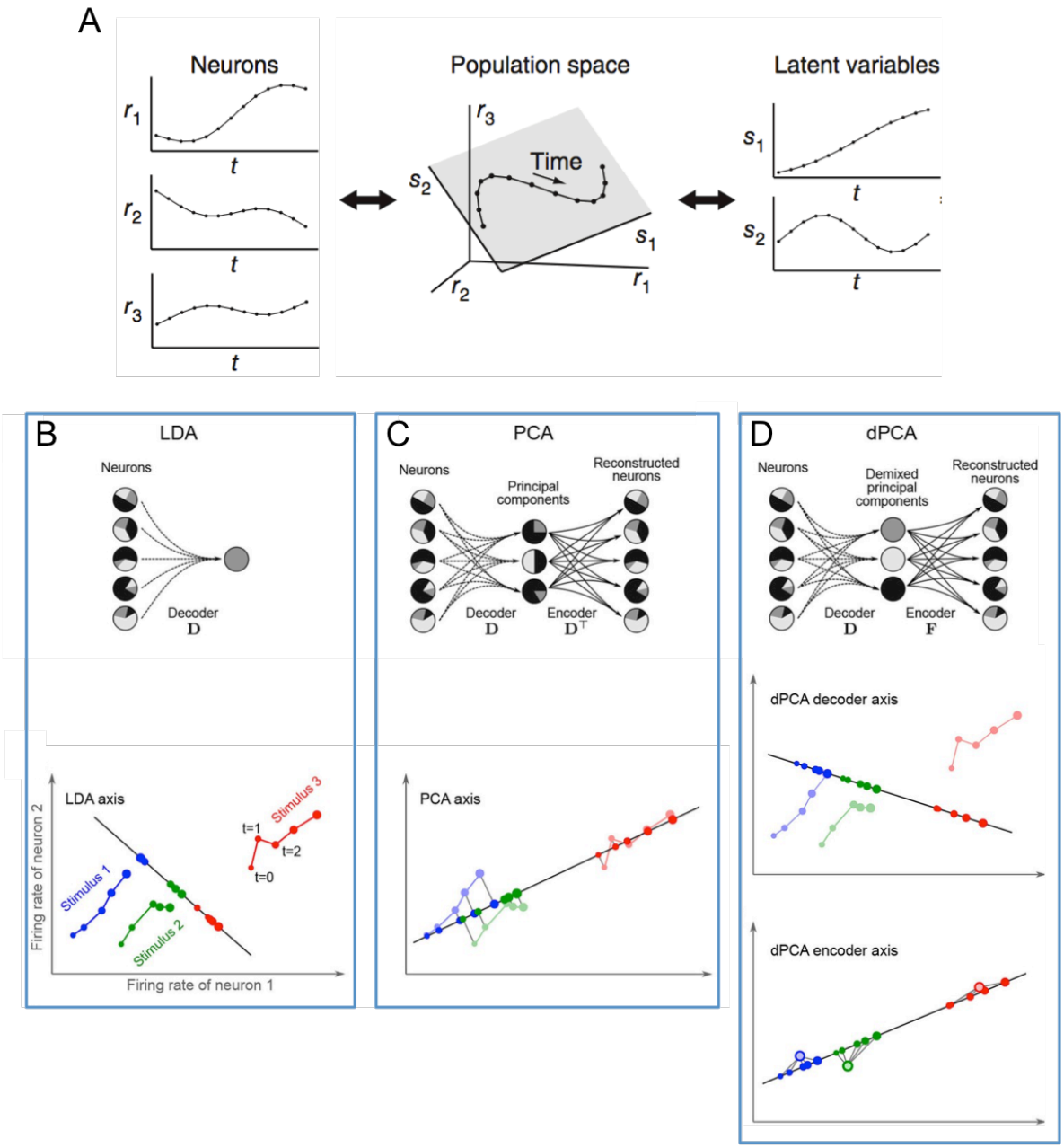

Figure 1.6 Dimensionality reduction and comparison of linear discriminant analysis (LDA), principal component analysis (PCA) and demixed principal component analysis (dPCA) (opposite page)

A) Traditionally, the change of firing rates is plotted against time. Here is an example of three neurons (r_1, r_2 and r_3) plotted separately (left). To visualize the population activity of three neurons, one can plot the firing rates of the neurons against each other. The black points represent population activity of the three neurons and each point in the [r_1, r_2, r_3] defined coordinates is one time point. However, the [s_1, s_2] coordinates (shaded gray plane) with less dimensions is already sufficient to describe the trajectory traced out by the black points (middle). The population activity projected on the two low-dimensional axes are the two latent variables [s_1, s_2] (right) (adapted from Cunningham and Yu, 2014). B-D) The three linear dimensionality reduction techniques: LDA, PCA and dPCA (in three boxes). In the upper part of each box, neurons are illustrated to have mixed selectivity for experimentally designed task parameters (different colors in each circle). In the lower part of each box, similar to A but with two neurons as example, firing rate of neuron 1 is plotted against firing rate of neuron 2 (same data for the three boxes). There are three stimuli (different colors) and five time points (indicated by

increasing size of the dots) (adapted from Kobak et al., 2016). B) The LDA works as a decoder that projecting data on the decoder axis achieves maximum demixing of the different task parameters. C) PCA searches axes that projecting data onto these axes preserves the maximum variance. These axes are ranked by the proportion of variance they captured. By preserving the proportion of variance as large as possible, these axes can also reconstruct the original data very well. In other words, they work both as decoder and encoder. However, the principal components yielded by the projections onto the PCA axes all have mixed selectivity, as in the neurons. In this example, only the first PCA axis is shown. D) dPCA tries to combined the objectives from LDA and PCA, demixing the different task parameter while preserving the data variance. This is achieved by having two axes, a decoder axis similar to LDA (middle part) and an encoder axis similar to PCA (lower part). The encoder is aiming to reconstruct the means of different stimulus classes (large colored circles).

Dimensionality reduction methods are designed for various purposes and differ in their statistical structures (Cunningham and Yu, 2014). Take the example with three neurons, these methods differs in how to find the two-dimensional plane. The objective could be capturing the greatest variance in the data (basic covariance methods), preserving the variance of the firing rate variability but discarding the variance of spike variability (methods with explicit noise model), characterizing the temporal dynamics of the population activity (time series methods), or preserving the dependent variables during dimensionality reduction (supervised methods). Some objectives can be potentially combined, and between some others, there is a trade off.

Principal component analysis (PCA) and factor analysis (FA) are the two well-known methods based on capturing the maximum variance in the data (basic covariance methods). PCA searches orthogonal axes that projecting data onto these axes preserves the maximum variance (Fig. 1.6 C). With these techniques, researchers were able to identify population response structures. The urgent need of analyses beyond the single neuronal level is well stated by (Cunningham and Yu, 2014)

“Population analyses are necessary in settings in which there may be neural mechanisms that involve coordination of responses across neurons. These mechanisms exist only at the level of the population and not at the level of single neurons, such that single-neuron responses can appear hopelessly confusing or, worse, can mislead the search for the true biological mechanism.”

In detail, one fails to find a clear relationship between the single neuron discharge patterns and the stimuli in a sensory task, or the movement kinematics in a motor

task. Looking at examples in the motor system, the activity of individual neurons in M1 and PMd during reaching movement in monkeys was indeed complex, multiphasic and heterogeneous (Churchland and Shenoy, 2007). In addition, the directional tuning of the whole population during the preparatory and movement periods was surprisingly only weakly correlated (Churchland et al., 2010b). However, preparatory tuning could be captured by a preferred direction in a PCA reduced space, and this description was better than any traditional tuning model. These findings suggested that preparatory activity could be an initial state of a dynamical system whose future evolution will produce movement.

One of the main drawbacks of PCA is that this method does not distinguish the different sources of variance. Spiking variability, for example, is not desirable in most cases. The conventional way to avoid spiking variability is to average neural activity across trials before PCA transformation. Sometimes this can be combined with temporal smoothing, e.g. Gaussian kernels. For analyzing raw spike counts (e.g. during real-time application), FA can better distinguish the variance of task-related firing rate changes from the spiking variability. This is achieved by preserving variance shared across neurons and assigning variance independent of each neuron as spiking variability (Churchland et al., 2010a). An outstanding example applying FA was a BMI experiment that identified the intrinsic manifold in M1 (Sadtler et al., 2014). In the first step of this study, monkeys learned to control a two-dimensional cursor using brain signal and a low-dimensional subspace (the “intrinsic manifold”) capturing covariance of all neurons was found by FA. In the second step, different perturbations showed that monkeys could proficiently learn the task by using activity patterns within the manifold, but not patterns outside. These results implies that learning in the brain is some how limited by the current existing network structures.

The covariance methods do not consider temporal dynamics of the data. Dynamics models take advantages of the sequential nature of the spike train, and use this feature to provide denoising to the data (e.g. chose the degree of smoothness and the kernel width for the smoothing). Most of the time series dimensionality reduction methods also have an explicit noise model (akin to FA), and are suitable

for single-trial analysis. Single-trial statistical power is particularly important under the circumstances that change of neural activity is not traceable with any experimentally measurable parameters. The increasing number of neurons recorded simultaneously enables the single-trial based statistics (Cunningham and Yu, 2014). Gaussian process factor analysis (GPFA) (Yu et al., 2009) is one of the commonly used time series dimensionality reduction method. Using this technique, researchers were able to extract single-trial smooth trajectories reflecting monkeys' internal decision process (Kaufman et al., 2015). In another study of the motor system, GPFA revealed that the closer the single trial trajectory was to the "ideal" initial subspace, the faster a movement was initiated (Afshar et al., 2011).

However, as a cautionary note in the review from Cunningham and Yu (2014), a particular low-dimensional trajectory obtained from dynamics models might run into the risk of being biased and the true features of the data are obscured. Therefore, it is recommended to use PCA or GPFA as a simple first step and then chose a specific model based on this step (Cunningham and Yu, 2014). An alternative way to avoid the structural constrains on dynamics models is to orthogonally project the data into a low-dimensional space identified by these models. jPCA is a method of this category, designed to capture the rotational structure existing in both rhythmic movements (e.g. swimming and walking) and non-periodic movements (e.g. reaching) (Churchland et al., 2012).

The last objective mentioned is to preserve the dependent variables, which may be related to experimental parameters, the subject's behavior or a time index. These supervised dimensionality reduction methods preserve the differences of the dependent variables while compressing the data. Linear discriminant analysis (LDA) functions as a decoder that projecting data on the decoder axes achieves maximum demixing of the different dependent variables (Fig. 1.6 B). However, this works when only one dependent variable is assigned to a data point. When having multiple dependent variables for each data point, one might want to separate the different dependent variables into independent components. The so called demixed dimensionality reduction can be achieved by linear regression after PCA transformation (Mante et al., 2013) or a difference of covariance approach (Machens

et al., 2010). With a probabilistic extension, the difference of covariance approach later developed into the demixed principal component analysis (dPCA) (Kobak et al., 2016). This method seeks to balance the two goals, aiming to find a decomposition of the data that are easily interpretable with respect to the task parameters (objective of supervised methods), while preserving the original data as much as possible (objective of basic covariance methods). This is achieved by using different decoder and encoder, where the decoder "demixes" and compresses the different task parameters while the encoder reconstructs the individual neurons from the compressed data. In the recent motor system research, dPCA has been applied to investigate the population coding of grasp and laterality-related information (Michaels and Scherberger, 2018), as well as to delineate the role of PMd and PMv for reaching and grasping (Takahashi et al., 2017).

Like other fields of science, systems neuroscience pursues to describe complex phenomena in simple terms. Recently, researchers have started to face the heterogeneity of single neurons, instead of considering the non-explainable firing rate variance as noise. Dimensionality reduction methods serve as a starting point for searching the simplicity at the population level. The importance of these methods increases with developments of large-scale recording techniques. On the other hand, the claim of significant population structure not existing at single-neuron level should be statistically tested. A surrogate-based test has been developed to test the significance of these structures (Elsayed and Cunningham, 2017).

1.7 Towards individuated finger movements in hand prosthesis

Using our hands is essential in our every day life. This becomes most apparent when we lose the ability to control our arm and hand. According to a survey asking quadriplegic patients to rank functions in order of importance to their quality of life, regaining hand and arm function was number one on the list (Anderson, 2004). Fortunately, with technological advancement, the hope of regaining hand and arm function is going to be realized through the development of BMI. These devices record and process activities from the neuromuscular system of a waking subject, and the computational output is then used to accomplish a task and/or drive a physical machine (Donoghue et al., 2007; Nicolelis and Lebedev, 2009; Schieber, 2011).

Reviewing the history of BMI, there are several trends worthy of mention. Firstly, using finger movements as an example, the development started with offline decoding (Georgopoulos et al., 1999; Ben Hamed et al., 2007) and later demonstrated the possibility in real-time (Baker et al., 2009). Secondly, the experiments were conducted first in animals, especially in non-human primates, and later in human patients. The main challenge of using invasive methods to record brain signals in humans is still the limited lifetime of the implanted sensors (Scherberger, 2009). Thirdly, the BMI control started with a small number of DOFs (e.g. control of a 2-D cursor on the screen), and until today, the number of DOF possible to be controlled online is still limited (Collinger et al., 2013), and still far from the known DOFs of the five-fingered hand (Feix et al., 2016).

There is an obvious time lag between researches for reaching and for grasping, as well as for individuated finger movements. Already in the early 2000s, real-time prediction of 3-D hand trajectory by ensembles of cortical neurons in monkeys was achieved (Wessberg et al., 2000), and this signal could be used to control a 3-D cursor with visual feedback, forming a “closed-loop” (Taylor et al., 2002). Some years later, the real-time interaction with the physical environment (embodiment) was realized, and monkeys were able to control a robotic arm with 5 DOFs to feed themselves (Velliste et al., 2008). The translation into human clinical studies took

less than a decade. With microelectrode array recording from M1, the tetraplegic participants suffered from brainstem stroke or spinocerebellar degeneration were able to control a 7-DOF-robotic arm to perform three-dimensional reach and grasp movements (Hochberg et al., 2012; Collinger et al., 2013).

These achievements are astonishing and this is surely a good news for paralyzed patients who hope to regain their arm and hand function. However, regarding the ability to control dexterous finger movements, there is still a long way to go. Although the number of DOF being controlled increased, there is only one DOF for the hand, the basic closing and opening. In the study of Velliste et al., the hand consisted of a motorized gripper with two "fingers", which was able to fulfill the self-feeding task. A more state-of-the-art anthropomorphic prosthetic limb was used in the study from Collinger and colleagues (2013). However, the more than 20 DOFs available from the prosthesis were combined into 1 DOF to be controlled from the brain signal. This means the number of DOF achieved in the state-of-the-art BMI control is much smaller than the number of DOF available from state-of-the-art hand prostheses. A possible explanation is that the 1-DOF grasping combined with 6-DOF reaching is able to complete a majority of tasks one needs in his daily life (mainly reaching and grasping). Nevertheless, understanding how skillful hand movements are stored and retrieved in the brain and being able to decode these movements effectively for prosthetic control are both future goals for basic science research and clinical application.

Looking one step back at decoding studies without online applications, up to 27 DOFs recorded from the arm and hand were able to be decoded when the monkeys grasped different objects (Vargas-Irwin et al., 2010; Menz et al., 2015). Albeit the different objects being grasped, the motions of individual fingers during grasping are highly correlated (Mason et al., 2001). This implies that for building a hand prosthesis that can move fingers independently, for example, to press a button or to type, the knowledge we gained from decoding studies of grasping might not be sufficient. An alternative strategy to gain insight into the neural coding of individuated finger movements is to train monkeys to move fingers as independently as possible with abstract cues (Schieber, 1991; Schieber and Hibbard, 1993).

Decoding “which finger was moved” with a classifier was first achieved (Ben Hamed et al., 2007; Aggarwal et al., 2008; Egan et al., 2012), and later continuous kinematics was also decoded (Aggarwal et al., 2009).

In addition to cortical signals, EMG signals (Farina et al., 2010) and neural activity from the peripheral nerves (Rossini et al., 2010; Hong et al., 2018) can also be inputs for BMI. In the 1990s, EMG activity was recorded when a monkey performed individuated finger movements (Schieber, 1995), and signals can be functionally grouped, according to the movements (Poliakov and Schieber, 1999). In a similar task involving only three fingers (thumb, index and middle finger), EMG activity was recorded with a wireless device and finger movements were decoded with a LDA classifier (Baker et al., 2010). Indeed, an EMG based method has been proven to work in humans. Using surface electromyographic signals, flexion and extension of all five fingers (10 conditions in total) were decoded (Tenore et al., 2009). However, EMG methods are only available for amputees, not for paralyzed patients. Even so, a recent development indicates a novel way for the paralyzed patients to use their paralyzed muscles. Through a neuromuscular electrical stimulator with 130 electrodes embedded in a flexible sleeve wrapped around the arm, the tetraplegic participant was able to continuously control six different wrist and hand movements (flexion and extension of the wrist and the thumb, opening the hand, and flexion of the middle finger) using cortical signals from M1 (Shaikhouni et al., 2016).

Development of hand prostheses capable of moving fingers individually is a tough challenge. Nevertheless, animal experiments and translation into human patients show evidence of progress in this direction.

1.8 Motivation and overview

Compared to reaching and grasping, there are a very fewer studies on individuated finger movements. Although individual finger movements in humans can be decoded with electroencephalography (EEG) signals (Liao et al., 2014) and electrocorticography (ECoG) signals (Kubánek et al., 2009), this is only possible when the subjects extend and flex their fingers repeatedly for 1.5 to 3 seconds. In order to have a more detailed knowledge of how the brain controls individuated finger movements, single-neuron level recording with higher temporal and spatial resolution is necessary. Macaque monkey is a primate model organism suitable for this purpose and many electrophysiological studies of reaching and grasping have been done in this species (Georgopoulos et al., 1982; Batista et al., 1999; Vargas-Irwin et al., 2010; Townsend et al., 2011; Schaffelhofer and Scherberger, 2016). However, observations from natural and trained movements suggest that monkeys have less ability than humans to move fingers independently (Kimura and Vanderwolf, 1970). This is likely the reason that there are fewer studies of individuated finger movements in monkeys than in humans, because it is challenging to train the animals to perform this kind of tasks.

Schieber is the talent scientist who managed to train the monkeys to perform flexion and extension movements of each digit and of the wrist. He first quantified the independence of the digits (Schieber, 1991) and later recorded EMG (Schieber, 1995) and neural signal from M1 (Schieber and Hibbard, 1993; Poliakov and Schieber, 1999). The following decoding studies of individuated finger movements were quite successful (Ben Hamed et al., 2007; Aggarwal et al., 2008; 2009; Baker et al., 2009; Egan et al., 2012), however, it was not easy to describe how individual finger movements are coded in M1. Compare to EMG, there's no clear functional groups of neurons corresponding to movements of the digits and wrist. Instead, the neurons were "broadly tuned", changing their firing rates during movements of several different digits (Poliakov and Schieber, 1999). As Schieber stated in his review: "Future work may delineate how a network of functionally diverse M1 neurons can control generation of specific hand and finger movements. A network of intermingled and overlapping representations may be able to control the

biomechanically coupled peripheral apparatus of the hand more efficiently than a network of discrete, spatially segregated notes." From a population perspective, the M1 neurons are not necessarily "functionally diverse", but having "mixed selectivity". With the recent development of population analysis techniques, we may able to see beyond the heterogeneity of single neurons and understand the control of individuated finger movements at the population level.

In addition to M1, we also aim to record more cortical areas involved in reaching and grasping, since fingers are the most distal parts of the upper limb system. Together with M1, F5 and AIP form the fronto-parietal grasping circuits, where the sensory information, mainly visual information, is transformed into a motor action. Previous studies of area AIP and F5 recorded neural activity while the monkeys grasped different objects (Murata et al., 2000; Raos et al., 2006; Schaffelhofer and Scherberger, 2016) or performed different grip types (Baumann et al., 2009; Fluet et al., 2010; Townsend et al., 2011; Lehmann and Scherberger, 2013; Schaffelhofer and Scherberger, 2016; Michaels and Scherberger, 2018). Compared to hand prehesion for grasping and grip types trained in previous studies, individuated finger movements are unique, and it is novel to delineate how AIP and F5 encode these movements.

In order to understand how individuated finger movements are coded in area AIP, F5 and M1, two monkeys were trained to perform a delayed finger flexion task, in which the thumb, index or middle finger was flexed individually or in combination with a neighboring finger. In this thesis, neural data were collected only from one monkey, because training of the second monkey is not accomplished yet. While the monkey performed the task, neural activity in area AIP, F5 and M1 was recorded simultaneously with floating microelectrode arrays. The real-time decoding was performed in parallel with the recording in cooperation with Dr. Andres Agudelo-Toro.

2. Methods

2.1 Basic procedures

Two male rhesus macaques (*Macaca mulatta*, Monkey M, 10.5 kg and Monkey N, 11.5 kg) were used in this study. Neural data were only collected from Monkey M in this thesis, because training of Monkey N is not accomplished yet. Monkey M was used in another study and was already implanted with a head holder on the skull and microelectrode arrays in cortical areas AIP, F5, and M1 at the beginning of the training. He was habituated to sit in a primate chair with the head fixed. Both arms of the animal were placed in tubes. The left arm was restrained in a long tube to prevent interacting with the setup. The right arm went through a short tube with a manipulandum attached at the end, where he performed the finger task with his hand. The right arm tube and the manipulandum was placed at a 45 degree angle upwards, in order to project the visual cues on the surface of the manipulandum. Cues were projected from a projector (Aiptek Q20, Taiwan, R.O.C) onto the white surface of the manipulandum, in front of each finger to indicate the desired movement (circles of ca. 1 cm in diameter). Eye movements were tracked with an infrared optical eye tracker (ISCAN, Woburn, MA, USA) and tracking was calibrated at the start of each session. All task relevant behavioral parameters (eye positions, stimulus presentation, switch activation) were controlled by custom-written behavioral control software implemented in LabView (National Instruments).

All animal care and experiments with the animals were performed in accordance with German and European law and in agreement with the *Guidelines for the Care and Use of Mammals in Neuroscience and Behavioral Research* (National Research Council (US), 2003), as well as with the *NC3Rs Guidelines* (**R**eplacement, **R**eduction and **R**efinement).

2.2 Microswitch manipulandum

Training a macaque monkey to do individuated finger movements is a very difficult task. The biggest challenge is to isolate the desired finger movements from the whole arm movement and the movements of the wrist and the palm. Secondly, both human and monkeys can't fully move one finger independently without moving other fingers simultaneously. To what degree should the experimenter allow the movements of the non-instructed fingers and how to monitor these movements are both challenges. Schieber (1991) successfully trained monkeys to perform flexion and extension movements of all five digits and of the wrist by using a manipulandum with slots separating and preventing adduction/abduction movements of the fingers (Fig. 2.1 A). The flexion and extension movements of the finger were detected by microswitches mounted ventral and dorsal to the distal phalanx of each digit. The position of the microswitch lever arm and the force applied to it could be precisely measured, however, the relationship of these measurements to the kinematics of each finger was not fully clear.

We decided to have an alternative strategy with less physical constraint for the finger task, since physical constraint of the setup could only prevent the unwanted movement, but not the muscle contractions. A data glove capable of tracking 27 degrees of freedom of the hand and arm was developed in our lab (Schaffelhofer and Scherberger, 2012). The idea was to train the monkey to perform finger flexion in a less constrain way by monitoring the kinematics with the data glove. However, it was easier for the monkey to learn to move individual fingers by pressing different buttons at the fingertip positions, and to introduce the data glove afterwards.

A manipulandum with microswitches (Marquardt 1050, Rietheim-Weilheim, BW, Germany) was used to train finger flexion movements (Fig. 2.1 C) and the data presented in this thesis was collected using this experimental setup. The manipulandum has five microswitches, arranged according to the fingertip positions of the monkey's right hand. Small plates between the thumb and the index, as well as between the index and the middle finger prevented the fingers from pressing a wrong microswitch. Thin metal layers were mounted on the index and middle finger microswitches, so when the monkey places his two fingers on these two

microswitches, an electrical circuit was formed and this signal could be used as a control of proper starting position of the hand.

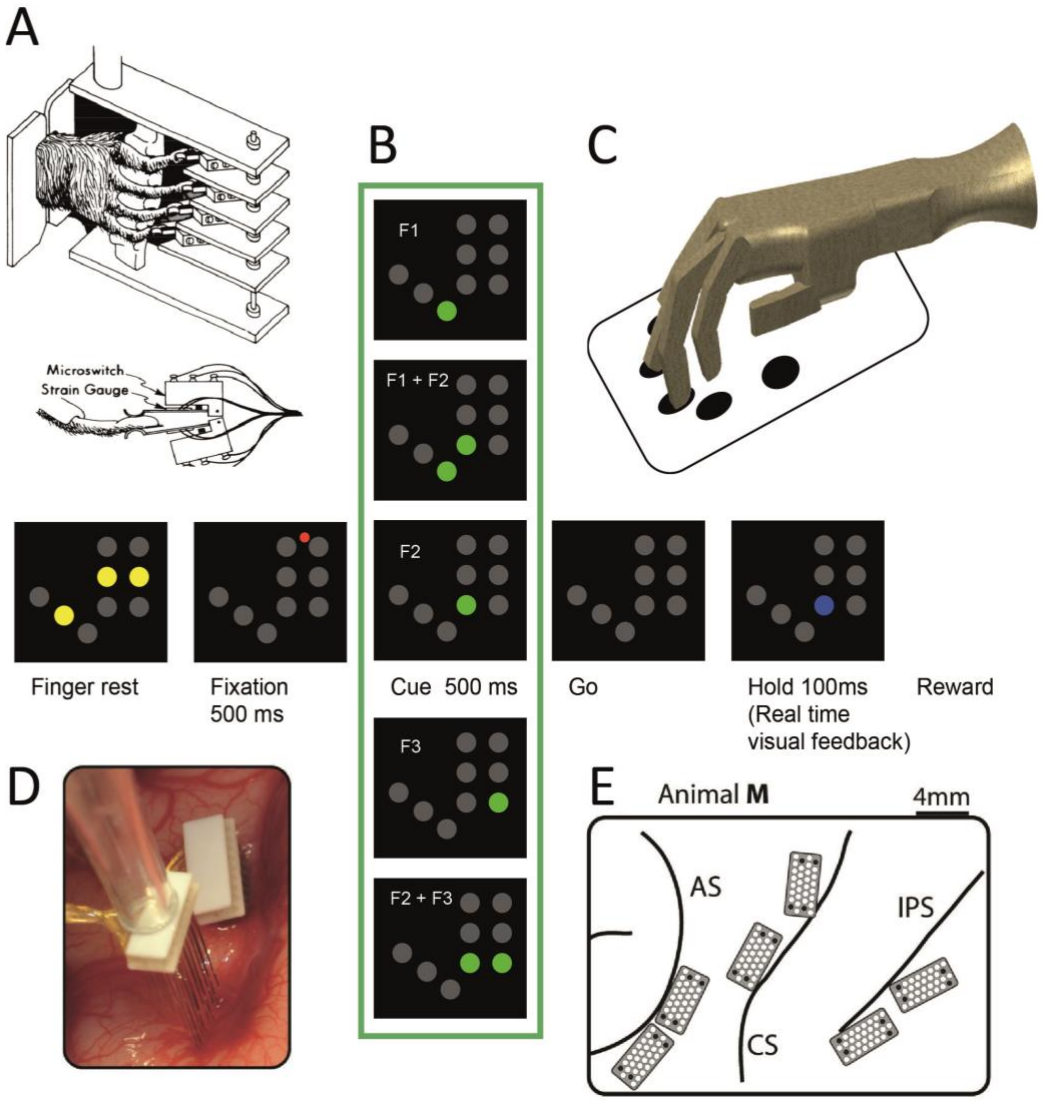

Figure 2.1 Experimental setups, task paradigm and array implantation

A) Schieber's (1991) manipulandum with slots and double microswitches on the dorsal and the ventral sides of each digit. B) Task paradigm. The gray dots mark the potential positions for cues and were not shown to the monkey. The positions of the dots mimic the thumb, index and middle finger of the right hand. There are three layers for each finger, where the second layer showed the finger rest positions (yellow) and the third layer showed the movement cue (green) and real-time feed back of press (blue). The first layer is not used in this study. The five cues are shown in the middle column (surrounded by the green rectangle). C) The microswitch manipulandum for detecting flexion movements of the right hand used in this study. D, E) Neural activity from area AIP, F5 and M1 was recorded simultaneously with six floating microelectrode arrays (left hemisphere of monkey M). Each array consisted of a 4x9 matrix with two ground and two reference electrodes (black), and 32 recording channels (white). Electrode length increased towards the sulcus from 1.5 mm to 7.1 mm. AIP arrays were implanted toward the lateral end of the intraparietal sulcus (IPS); F5 arrays were on the posterior bank of the arcuate sulcus (AS); M1 arrays were implanted in the hand region, which was on the anterior bank of the central sulcus (CS) (Schaffelhofer and Scherberger, 2016).

2.3 Task paradigm

The monkey was trained to perform an individual and combined finger flexion task with five different conditions, including individual thumb (F1), index (F2) and middle finger (F3), and the double movement of F1+F2 and F2+F3 (Fig. 2.1 B). A trial was initiated when the monkey placed his index and middle finger on the microswitches (described in the previous section). When the electrical circuit formed, the three yellow dots disappeared. A fixation dot appeared between the index and middle finger cues and the monkey was required to fixate during the entire trial. After fixating for 500 ms (fixation epoch), the cue appeared as green dots in front of the instructed finger(s) for 500 ms (cue epoch). Double movements were indicated with two dots. Cues were presented in a pseudorandom order, where successful trials were removed and the unsuccessful trial stayed in the pool. The monkey was allowed to press after the cue disappeared (go epoch, maximum 1000 ms). After pressing the correct microswitche(s) for 100 ms (hold epoch), a drop of juice was delivered as a reward. When the microswitches were pressed, blue dots appeared at the same positions of the cues as a visual feedback. This helped the monkey identify both a correct press and an incorrect press. Incorrect trials were aborted immediately.

2.4 Surgical procedures and imaging

Prior to surgery, a 3D anatomical MRI scan of the animal's skull and brain was performed to locate anatomical landmarks (Townsend et al., 2011). For this, the animal was sedated (e.g. 10 mg/kg ketamine and 0.5 mg/kg xylazine, i.m.), placed in the scanner (Siemens TrioTim; 1.5 Tesla) in a prone position, and T1-weighted images were acquired (iso-voxel size: 0.7 mm^3). We measured the stereotaxic location of the arcuate, central and intra-parietal sulci to guide placement of the electrode arrays.

The surgery is planed in two procedures: First, a head post (titanium cylinder; diameter 18 mm) was implanted on top of the skull (approximate stereotaxic position: midline, 40mm anterior, 20° forward tilted) and secured with bone cement

(Refobacin Plus, BioMed, Berlin) and orthopedic bone screws (Synthes, Switzerland). After recovery from this procedure and subsequent training with head fixation, the animal was implanted in a second procedure with six floating microelectrode arrays (FMAs; MicroProbes for Life Science, Gaithersburg, MD, USA). Specifically, two FMAs were inserted in each area AIP, F5, and M1 (Fig. 2.1 D, E). FMAs consisted of 32 non-moveable monopolar platinum-iridium electrodes (impedance: 300-600 kΩ at 1 kHz) as well as two ground and two reference electrodes per array (impedance < 10 kΩ). Electrode lengths ranged between 1.5 and 7.1 mm and monotonically increased to target grey matter along the sulcus.

Electrode array implantation locations are depicted in Fig. 2.1 E. The lateral array in AIP was located at the end of the intraparietal sulcus at level of PF, whereas the medial array was placed more posteriorly and medially at the level of PFG (Borra et al., 2008). In area F5, the lateral array was positioned approximately in area F5a (Belmalih et al., 2009, Borra et al., 2010), whereas the medial array was located at the border of F5a and F5p. Finally, both arrays in M1 were positioned in the hand area of M1 (anterior bank of the central sulcus at the level of the spur of the arcuate sulcus and medial to it) (Rathelot and Strick 2009).

All surgical procedures were performed under aseptic conditions and general anaesthesia (e.g. induction with 10 mg/kg ketamine, i.m., and 0.05 mg/kg atropine, s.c., followed by intubation, 1-2% isofluorane, and analgesia with 0.01 mg/kg buprenorphene, s.c.). Heart and respiration rate, electrocardiogram, oxygen saturation, and body temperature were monitored continuously. Systemic antibiotics and analgesics were administered for several days after each surgery. To prevent brain swelling while the dura was open, the animal was mildly hyperventilated (end-tidal CO_2 < 30 mmHg) and mannitol kept at hand. Animals were allowed to recover for about two weeks before behavioral training or recording experiments recommenced.

2.5 Neural recordings and spike sorting

Neural signals recorded simultaneously from the total of 192 channels of the six arrays (in areas AIP, F5 and M1) were amplified and digitally stored using a 256 channel TDT RZ2 (sampling rate 24.414 kS/s; 0.6-10000Hz band-pass hardware filter, Tucker-Davis Technologies, Alachua, FL, USA). Preprocessing before spike detection includes filtering and denoising: raw neural signals were first low-pass filtered with a median filter (window length 3ms). The filtered signal was then subtracted from the original data, and this corresponds to a nonlinear high-pass filter. A non-causal Butterworth low-pass filter (5000 Hz; 4^{th} order) was then applied to the subtracted signal. Principal component analysis (PCA) was applied for all electrodes of each array to eliminate common noise sources, as described previously (Musial et al., 2002). To ensure that no individual electrodes were discarded, PCs with a normalized coefficient larger than a conservatively chosen 0.36 threshold were retained.

Spike waveforms were detected and semi-automatically sorted using a modified version of the offline spike sorter Wave_clus (Quiroga et al., 2004; Michaels et al., 2015; Dann et al., 2016). The spike sorting steps are as follows: (1) spike detection, (2) feature extraction, (3) clustering, (4) template matching, and (5) redetection.

Spike detection was performed by amplitude thresholding after the preprocessing as described above. The threshold was set to $4\sigma_n$, where σ_n is an estimate of the standard deviation of the background noise, using the median of the bandpass-filtered signal. Compare to taking the standard deviation of the signal, taking the median avoids the interference of the high firing rates and large amplitudes of the spikes.

Feature extraction of spike shapes was conducted by testing outcome from PCA, wavelet transform (WT) and original waveforms with the Lilliefors test separately. The PCA finds the dimensions capturing the maximum variance and the data projected on the first three PCs were used. The WT is a time-frequency representation of the signal, providing an optimal resolution in both time and the frequency domains without the requirement of signal stationarity. Wavelet coefficients characterize the spike shapes at different scales and times. Such

coefficients should have a multimodal distribution if there is more than one spike class. The Lilliefors test compares the cumulative distribution function of the data with that of a Gaussian distribution with the same mean and variance.

Clustering of the spikes by the selected features was done by superparamagnetic clustering. This idea is based on simulated interactions between each data point and its K-nearest neighbors. The strength of interaction between one point and its nearest neighbors spikes falls off exponentially with increasing Euclidean distance, which corresponds to the similarity of the selected features. An initial random state is assigned to each point, and the probability that the nearest neighbors of this point will also change state together is dependent on the interaction strength and the "temperature", which has a physical analogy with a spin glass. At the so-called high temperature "paramagnetic phase", all the spins switch randomly, independent of their interactions. At the low temperature "ferromagnetic phase", the entire spin glass changes its state simultaneously. In the medium range "superparamagnetic phase", only spins that interact with each other will change their state simultaneously. Regarding the clustering problem, at low temperatures, all spins tend to switch their state simultaneously and will thus be classified into a single cluster; at high temperatures, many spins change their state independently, as a result, partitioning the data into several clusters. In Wave_clus, the temperature is plotted against the cluster sizes and a graphical user interface (GUI) is implemented in Matlab to manually select the clusters at different temperatures. The user moves the cursor between the space of the cluster frontiers, starting from low temperatures and moving towards the high temperatures to point the desired clusters. Unassigned waveforms are *matched to the templates* of the desired clusters by linear discriminant analysis (LDA) classifier.

After waveforms being semi-automatically sorted, the different averaged templates were redetected to discover the overlaid waveforms (Gozani and Miller, 1994). The *redetection* was achieved by convolution of the filtered signals with the waveform templates, starting from the one with largest magnitude. As a second step, the redetected waveforms were classified by a LDA classifier, and this was performed independently for each template. After each redetection, the current template was

subtracted from the filtered signal to reduce artifacts during the next redetection. With this paradigm, spikes with a temporal overlap up to 0.2 ms could be redetected. We set 30% as a threshold to check the stationarity of all units. If there had been more than 30% firing rate change between the first 10 min and the last 10 min of the recording session, the unit would be excluded from further analyses.

After spike sorting, we classified units into single- or non-single unit according to five criteria (Dann et al., 2016): (1) the absence of short (1-2 ms) intervals in the inter-spike interval histogram for single units; (2) the homogeneity and spike density of the detected waveforms; (3) the separation of waveform clusters in the projection of the first 17 features (a combination for optimal discriminability of PCs, single values of the wavelet decomposition, and samples of spike waveforms) detected by Wave_clus; (4) the presence of well-known waveform shapes characteristics for single units; and (5) the shape of the inter-spike interval distribution.

2.6 Behavioral data analysis

The performance of each session was recorded and the behavioral success rate of each condition was calculated. Since the monkey was placing his fingertips already on the microswitches, it was not possible to distinguish the reaction time (time from go cue onset to movement onset) from the movement time (time from movement onset to goal reached). Therefore, reaction time + movement time (RM time) was used as the criterion to select trials for further analysis. The RM time of the double movements (F1+F2 and F2 + F3) was much longer than the RM time of single movements (F1, F2 and F3). As a compromise, histograms of RM time were plotted for each condition and different thresholds were chosen for the single movements (0.2 s) and the double movements (0.42 s) in order to have enough trials for each condition. In addition to RM time, the time between the two presses of the double movements was also controlled, so it could not be longer than the hold time of a single movement (100 ms). According to this criterion, the kinematics of a double movement was different from the kinematics of two sequential single movements.

2.7 Peristimulus time histograms (PSTHs)

After sorting, spikes were binned into non-overlapping 1-ms windows and smoothed with a Gaussian kernel (σ = 60 ms). Data were aligned to cue onset and hold onset. Since there was no memory epoch and the offset of cue was used as the go signal, the monkey was anticipating the go signal during the cue epoch and there was a clear change of firing rate during this epoch. We chose the cut-off time after the cue epoch and before the hold epoch, so that there were small overlaps and smooth transitions, though this cut away the go signal. PSTHs were then calculated by averaging over all trials per condition and unit.

2.8 Cluster-based permutation test

In order to deal with the multiple comparison problem of multiple time points in the neural data, the cluster-based permutation test (Maris and Oostenveld, 2007) was used in this study. The nonparametric test is performed by randomly permuting the experimental conditions of the trials (1000 times in this study) and calculate the test statistic on these random partitions. The permutation p-value is the proportion of random partitions that resulted in a larger test statistic than the observed one (non-permuted original data). The critical alpha-level for the p-value was set at 0.01 or 0.05. When dealing with the multiple comparison problem, clustering the adjacent time-samples is less conservative than the Bonferroni correction. For every time point, the conditions were tested with a t-test and all the time points whose t-value was larger than some threshold (this threshold only affect the sensitivity of the test, not the false alarm rate) were selected and clustered on the basis of temporal adjacency. The cluster-level statistics was calculated by the sum of the t-values within a cluster and only the largest cluster was taken for test statistic described above.

2.9 Tuning analysis

The tuning of a unit is defined as the differential response among the five conditions and was tested by the cluster-based permutation test. All units in of one cortical area were aligned by their tuning onset to obtain an overview of the population response. In addition, the percentage of tuned units of each time point was calculated for each area to compare the tuning onset across areas. While the cluster-based permutation test tests for difference among the conditions, Tukey-Kramer test (Matlab functions: anova1, multcompare) tests for significant differences between all possible condition pairs (five conditions resulting in ten condition pairs).

2.10 Partial correlation between error trials and their corresponding correct trials

Besides comparing the tuning onset of the three areas, another way to investigate the different roles of the three areas involved in the visuomotor transformation is to calculate the partial correlation coefficient (pcc, matlab function: partialcorr, Cramér, 1946). Firstly, we searched for the error trials, which have exactly the same movement pattern as a correct trial (a trial instructed with condition A, but pressed a non-A microswitch for more than 100 ms, where non-A belongs to one of the other four conditions). For the six sessions analyzed, trial number of the selected error trials were calculated and only the categories (instructed A, pressed B) with more than 5 trials were used for further analysis. There were two type of partial correlation coefficient: The “cue error pcc” was calculated between one type of error trial and the correct trial with the same cue, where the influence of the correct trial with the same movement was controlled. The “movement error pcc” was calculated between one type of error trial and the correct trial with the same movement, where the influence of the correct trial with the same cue was controlled. The “cue error pcc” is described by

$$\rho_{AB,AA \times AB,BB} = \frac{r_{AB,AA} - r_{AB,BB} r_{BB,AA}}{\sqrt{1 - r_{AB,BB}^2}\sqrt{1 - r_{BB,AA}^2}}$$

where ρ is the pcc between an instructed-A pressed-B error trial (denoted as AB) and an instructed-A pressed-A correct trial (denoted as AA), controlling for the effect of the movement (instructed-B pressed-B correct trial, denoted as BB). The "movement error pcc" is then described by

$$\rho_{AB,BB \times AB,AA} = \frac{r_{AB,BB} - r_{AB,AA} r_{BB,AA}}{\sqrt{1 - r_{AB,AA}^2}\sqrt{1 - r_{BB,AA}^2}}$$

$r_{AA,BB}$ is the standard Pearson's correlation between vectors AA and BB. The pcc was calculated separately for each time point. To be exact, it is the pcc between the firing rates of all neurons from the error trial and the firing rates of all neurons from the corresponding correct trial. The trial alignment and smoothing process were the same as in section 2.7. Firing rates were log 10 transformed before calculation of pcc.

2.11 Dimensionality reduction

The growth in scale and resolution of recording techniques creates new challenges for the analysis of neural data. Recent neuroscience experiments have simultaneously recorded units of multiple trials and multiple experimentally designed conditions. As the number of neurons, trials and conditions increases, it becomes challenging to extract meaningful structure from these large amount of data. In spite of this complexity, it is actually an exciting moment to be able to study populations of neurons. According to Cunningham and Yu (2014), population data could gain single-trial statistical power, be used to study population response structure and for exploratory data analysis. The data collected in this study is suitable for the last two purposes.

PCA is one of the most basic and well-used covariance based dimensionality reduction methods. PCA was applied to trial-averaged, temporally smoothed PSTHs (matlab function: princomp, svd). The PSTHs were packed into a matrix n x ∑ c(t), where n is the number of recorded neurons, and c(t) denotes the selected conditions over time. The PCA identifies an ordered set of orthogonal directions that captures the greatest variance in the data. The original data were then projected onto these axes, forming a low dimensional data set k x ∑ c(t), where k represents the dimensions across which the most variance was explained.

In contrast to discovering the population activity in an unsupervised fashion, a possible objective of dimensionality reduction is to project the data such that differences in the experimentally designed dependent variables are preserved. If there are multiple dependent variables for each data point (movement condition and time in our study), one might seek to "demix" the effects, so that each projection axis captures the variance of a single dependent variable. The PCA based demixed principal component analysis (dPCA) was used in this study (Kobak et al., 2016). Brief introduction to this method is presented in the following section.
Both PCA and dPCA were applied for visualization and as preprocessing for further analysis.

2.12 Demixed principal component analysis (dPCA)

Neurons in higher cortical areas are often tuned to multiple sensory and motor variables, displaying a mixed selectivity. There are two sources contributing to the firing rate variance of the neural population in a behavioral task: The first part is the condition-dependent part, reflecting the designed task parameters, such as stimuli, movements and reward. The common goal of neuroscience studies is to draw conclusions from the relationship between the firing pattern and the task parameters. However, there's a second part, the condition-independent part, which is common among all conditions. For example, firing rates usually increase during movement. When this second source is relatively large, compared to the first one, the difference among conditions could be buried. Separating these two parts of variance is the most important in our study.

dPCA is a dimension reduction technique, which decomposes population activity into few components based on the designed task parameters, including the condition-dependent and the time-dependent (condition-independent) components. The purpose of this technique is to "demix" the task parameter while maintaining the maximum variance explained in the dimension reduced data.

The "demix" is achieved by a marginalization procedure. Taken two task parameter "stimulus (s out of S)" and "decision (d out of Q)" as example, this data set can be

thought of as KSQ time-dependent neural trajectories (K trials for each of the SQ condition), collected in a matrix X of size N x KSQT (N denotes number of neurons). For one neuron, its spike train x_{tsdk} can be decomposed intro a set of averages (called marginalization) over combination of parameters. The angular brackets <> denotes the average over a set of parameters $\{a, b, \ldots\}$:

$\bar{x} = \langle x_{tsdk} \rangle_{tsdk}$

$\bar{x}_t = \langle x_{tsdk} - \bar{x} \rangle_{sdk}$

$\bar{x}_s = \langle x_{tsdk} - \bar{x} \rangle_{tdk}$

$\bar{x}_d = \langle x_{tsdk} - \bar{x} \rangle_{tsk}$

$\bar{x}_{ts} = \langle x_{tsdk} - \bar{x} - \bar{x}_t - \bar{x}_s - \bar{x}_d \rangle_{dk}$

...

$\varepsilon_{tsdk} = x_{tsdk} - \langle x_{tsdk} \rangle_k$

The original neural activities are given by the sum of all the marginalizations:

$$x_{tsdk} = \bar{x} + \bar{x}_t + \bar{x}_s + \bar{x}_d + \bar{x}_{ts} + \bar{x}_{td} + \bar{x}_{ds} + \bar{x}_{tds} + \varepsilon_{tsdk}$$

We are not interested in demixing a time-dependent pure stimulus term $\bar{x}_s$ from a time-stimulus interaction term $\bar{x}_{ts}$, since all components changing with time is expected. These two terms are thus grouped and noted as $\bar{x}_{ts}$. Same rule applies for the decision terms. Applying this marginalization procedure to every neuron and splitting the whole data matrix X, we can write the decomposition in matrix form:

$$X = X_t + X_{ts} + X_{td} + X_{tds} + X_{noise} = \sum_\phi X_\phi + X_{noise}$$

The second step of dPCA is dimension reduction. Classical PCA compresses the data with a decoder matrix D and the resulting principal components can be linearly de-compressed with an encoder matrix D^T to reconstruct the original data. We can search for the optimal D matrix by minimizing the squared error lost function between the original data X and the reconstructed data $D^T DX$

$$L_{PCA} = \| X - D^T DX \|^2.$$

The dPCA makes two changes to this classical formulation. First, reconstruct each marginalization X_ϕ mentioned instead of the whole data matrix X. Second, gain additional flexibility by compressing and decompressing with different linear mappings, matrix D and matrix F, respectively. These two matrices are chosen to minimize the lost function

$$L_{dPCA}=\sum_\phi \| X_\phi - F_\phi D_\phi X \|^2.$$

Reduced-rank regression and *singular value decomposition* can minimize and solve each term in the sum. Each row of each D_ϕ is one demixed principal component. The components are ordered by the amount of explained variance, similar to PCA. The decoder/encoder axes corresponding to two different task parameter ϕ_1 and ϕ_2 are found independently and are allowed to be non-orthogonal (in PCA the principal axes are required to be orthogonal).

dPCA is prone to overfitting like other decoding method. A standard way to avoid this is to add a quadratic penalty term to the lost function L_ϕ:

$$L_\phi =\| X_\phi - FDX \|^2+ \mu \| FD \|^2,$$

where

$$\mu = (\lambda \| X \|)^2.$$

Optimal λ of each dataset is selected by leave-one-out cross-validation. One random trial of each neuron in each condition is held out to be the testing set and the remaining trials are averaged to form a training set. dPCA is performed on the training set for λ values between 10^{-7} and 10^{-3} and the normalized reconstruction error $L_{CV}(\lambda)$ is computed on the test set. This procedure is repeated ten times for different train-test splittings. The averaged resulting functions $L_{CV}(\lambda)$ has a clear minimum that is selected as the optimal λ.

The decoding axis of each dPC in the condition-dependent marginalization is used as a linear classifier to decode the condition respectively. 100 iterations of stratified Monte Carlo leave-group-out-validation are used, where the training set and the testing set were formed as in searching the optimal λ process. After running dPCA on

the training set, the decoding axes of the first three condition-dependent dPCs are used as classifiers. For example, the mean value of the first dPC for each condition is computed separately for each time point. Each test trial is projected on the decoding axis and is classified time point by time point based on the closest class mean. This results in a time-dependent classification accuracy, which is then averaged over 100 repetitions. 100 shuffles are then used to compute the distribution of classification accuracies expected by chance. In the results figures, we defined the significant classification according to two criteria: (1) the actual classification accuracy exceeds the accuracies from all 100 shuffles; (2) this period is longer than at least ten consecutive time bins.

2.13 Distance Analysis

To estimate the minimum neural distance between condition pairs (distance between neural trajectories of two conditions, resulting ten condition pairs from five conditions, e.g. F1-F2 is the label for distance between condition F1 and F2), the Euclidean distance between two conditions was calculated for each time point separately (matlab function: pdist). The calculation was performed in three different spaces (Ames et al., 2014): the full neuronal space (each unit seen as one dimension and square root of firing rate was used), k PCs (where the explained variance of k PCs exceed 90%), and the first five condition-dependent dPCs (each PC or dPC as one dimension). The distance calculation in the full space was single-trial based. If there were m trials for condition A and n trials for condition B, there will be m x n cross condition single trial pairs. The Euclidean distances between all the pairs were calculated and averaged. The reason for using single trial instead of trial averaged firing rate is because of the large difference of trial number among the five conditions. The Euclidean distance between a condition pair decreases when the number of trials being averaged increases. This is likely that averaging over trials smoothes the trajectories and results in smaller distance between conditions. Among the ten condition pairs, selected groups were plotted. We focused on comparing the double movements with its corresponding single movements, e.g. F12-F1, F12-F2 and F1-F2 (F1+F2 is simplified as F12), and among the three single movements F1-F2, F1-F3 and F2-F3. To compare among the three areas, the Euclidean distances were normalized by the square root of the number of units within each area.

2.14 Multiple linear regression

To determine whether the neural trajectories of double movements (F1+F2 and F2+F3) are linear combinations of the trajectories of its two corresponding single movements, a multiple linear regression was performed (matlab function: regress):

$$X_{12} = X_1\beta_1 + X_2\beta_2 + \beta_0 + \epsilon$$

where X_{12} denotes the trajectory of the double movement (response variable), X_1 and X_2 denote trajectories of the two corresponding single movements (predictor variables). β_1, β_2 and β_0 are regression coefficients and β_0 is the constant term. ϵ is the error term capturing all the other factors not contributed by the predictor variables. In detail, the original data (including predictor and response variables) are projected onto the first five PCA/dPCA (condition-dependent) axes. Theses rotation axes are found by using the averaged firing rate of all trials in each condition:

$$X_1 = \sum_{k=1}^{5} X_{1,k}\,;\; X_2 = \sum_{k=1}^{5} X_{2,k}\,;\; X_{12} = \sum_{k=1}^{5} X_{12,k}$$

where $X_{1,k}$, $X_{2,k}$, and $X_{12,k}$ are the predictor/response variable projected onto the k^{th} PCA/dPCA axis, respectively. The response variable projected onto the k^{th} PCA/dPCA axis is then predicted by the two predictor variables projected onto the same axis:

$$X_{12,k} = \sum_{k=1}^{5} X_{1,k}\beta_{1,k} + \sum_{k=1}^{5} X_{2,k}\beta_{2,k} + \beta_{0,k} + \epsilon_k$$

where $\beta_{1,k}$, $\beta_{2,k}$, $\beta_{0,k}$ and ϵ_k are the corresponding regression coefficients and the error term of predicting the data projected onto the k^{th} PCA/dPCA axis.

The multiple linear regression is 2-fold cross-validated by splitting half of the trials of the double movements into training set and the other half into testing set. Both the training and the testing set used the same rotation axes. The trials of the double movements were split k times, where k equals to the number of all possible combination from n choose (n/2) (matlab function: nchoosek), where n is the total trial number. When k was larger than 100000, a random set of combinations instead of all the combinations was applied. In this case, the trials were split randomly into

two sets of training and testing data for 5000 times. The trials in each set were averaged to obtain one trajectory, the training ($X_{12\ train}$) and the testing ($X_{12\ test}$) trajectory, respectively. Five dPCs (condition-dependent components) or PCs were regressed separately as described above. β values were computed with the training set:

$$X_1\beta_{1\ train} + X_2\beta_{2\ train} + \beta_{0\ train} + \epsilon = X_{12\ train}$$

The reconstructed double movement latent variables ($X_{12\ re}$) were obtained using a linear combination of single digit movement trajectories with estimated beta values as weighting factors:

$$X_{12\ re} = X_1\beta_{1\ train} + X_2\beta_{2\ train} + \beta_{0\ train}$$

This procedure was repeated k times with different training sets. In every iteration, one correlation coefficient was computed from the reconstructed trajectory ($X_{12\ re}$) and the testing trajectory ($X_{12\ test}$), where the latent variables were concatenated into one trajectory. This resulted in a distribution of r values and we used the mean as the goodness of fit.

The third single movement (the single movement unrelated to the double movement) was regressed as a reference for the r value (e.g. r value of regressing F12 with F1 and F2 should be compared with r value of regressing F3 with F1 and F2). The number of trials for the third single movement to be averaged in the cross-validation sets is n/2, where n is the number of trials of the double movement to be compared. Therefore, the level of variation in the multiple linear regression for the response variable and the predict variables were controlled.

2.15 Decoding

The neuronal signals captured during movement of individual and combined fingers were decoded with a Naïve Bayes classifier online and offline. The online classification was performed to demonstrate the possibility of using the obtained signals in a brain computer interface. The offline analysis was later performed with the real-time sorted spikes for validation and with manually sorted spikes (Wave_clus toolbox). The latter was intended to assess the quality of the real-time sorting and for further analyses.

Neuronal data was obtained with a RZ2 BioAmp Processor (Tucker Davis Technologies TDT, Florida USA). The output of the six arrays (192 channels total) was pre-processed online with a band pass filter (300 to 7000Hz) and given to the online spike sorter. Spikes were detected with automatic thresholding (4 times standard deviation from a 5 second window) and sorted manually either in the PCA feature space or with the waveform view. Single and multi-unit counts were binned into 40 ms bins and sent synchronized with the epoch and behavior information via UDP to a decoding computer. The processing pipeline on the RZ2 was custom build using the RPvdsEx design tool provided by TDT.

The Naïve Bayesian decoder was implanted in LabVIEW as in previous studies (Schaffelhofer et al., 2015; Townsend et al., 2011). Assuming statistical independence between the firing rates $\mathrm{f_i}$ of different units ($i=1,\ldots,n$), the likelihood function $\mathrm{L(c)}$ was computed as $\mathrm{L(c)} = \prod_{i=1}^{n} \mathrm{p(c|f}_i)$, where $\mathrm{p(c|f}_i)$ represents the probability of observing condition c for a given firing rate f_i of unit i. Bayes' theorem states that

$$\mathrm{p(c|f}_i) = \frac{\mathrm{p(f}_i|\mathrm{c}) \cdot \mathrm{p(c)}}{\mathrm{p(f_i)}}$$

where $\mathrm{p(f}_i|\mathrm{c})$ is the probability of observing the firing rate $\mathrm{f_i}$ under condition c, i.e. the set of distributions for a given unit under different conditions, which can be readily obtained assuming a training set. For any given condition the terms $\mathrm{p(c)}$ and $\mathrm{p(f_i)}$ can be extracted from the product in $\mathrm{L(c)}$ as

$$\mathrm{L(c)} = \frac{\mathrm{p(c)}^n}{\prod_{i=1}^{n} \mathrm{p(f}_i)} \prod\nolimits_{i=1}^{n} \mathrm{p(f}_i|\mathrm{c})$$

For an observed set of firing rates to decode the condition for which $\mathrm{L(c)}$ produces the maximum likelihood is selected as the decoded condition (i.e. the finger or finger combination that was most likely used). The term $\frac{\mathrm{p(c)}^n}{\prod_{i=1}^{n} \mathrm{p(f}_i)}$ is constant across conditions so $\mathrm{L(c)}$ can be approximated as

$$\mathrm{L(c)} \approx \prod_{i=1}^{n} \mathrm{p(f}_i|\mathrm{c})$$

Furthermore the right hand term can be also computed as a sum if a logarithm is applied, preserving the maximum. The logarithm allows computing the term as a sum instead of a product with larger numerical stability (floating point operations of large number of variables with values less than 1 and/or close to zero).

To train the decoder, the probability distributions $\mathrm{p(f}_i|\mathrm{c})$ were estimated from the mean firing rates observed in the training data under the assumption of a Poisson distribution.

Over eight days, 17 runs of the real-time decoder were performed. In each run, the decoder was trained online with approximately 10 correct trials per condition (approx. 50 trials in total) before real-time decoding. The average of the binned unit activity during fixation, cue, go, and hold epochs were used for training and decoding the finger movements. Offline decoding from five selected sessions was performed with online sorted spikes (the same as for real-time decoding), as well as with the manually sorted spikes, using an 8-fold cross-validation procedure with the same decoder used in real-time.

3. Results

3.1 Reaction and movement time

In motor system research, reaction time and movement time are important parameters to monitor behavior. However, with the microswitch manipulandum used in this study, it was not possible to distinguish these two parameters and we used the combined reaction and movement time (RM time) instead (section 2.6). Fig. 3.1 shows the RM time histograms of the five conditions, where the single movements have an exponential-like distribution and the double movements have a peak near 0.2 sec. This shows that it was easier for the monkey to perform single movements than double movements. In order to have clear PSTHs, trials with long RM time should be discarded and we set different thresholds for the single (0.2 sec) and the double movements (0.42 sec) to have enough trials. The two thresholds were selected based on the RM histogram (red dotted line). After thresholding, the averaged RM time for the five conditions were 81±51 ms (F1), 97±58 ms (F2), 221±83 ms (F1+F2), 83±51 ms (F3) and 203±80 ms (F2+F3).

Figure 3.1 Reaction time + movement time (opposite page)

RM time histograms of the five conditions pooled from six sessions, binned into 0.025 sec bins starting from 0 to 1 sec. The red dotted line shows the threshold of each condition (0.2 for single movements and 0.42 for double movements). The averaged RM time and the standard deviation were calculated from the trials with shorter RM time than the thresholds.

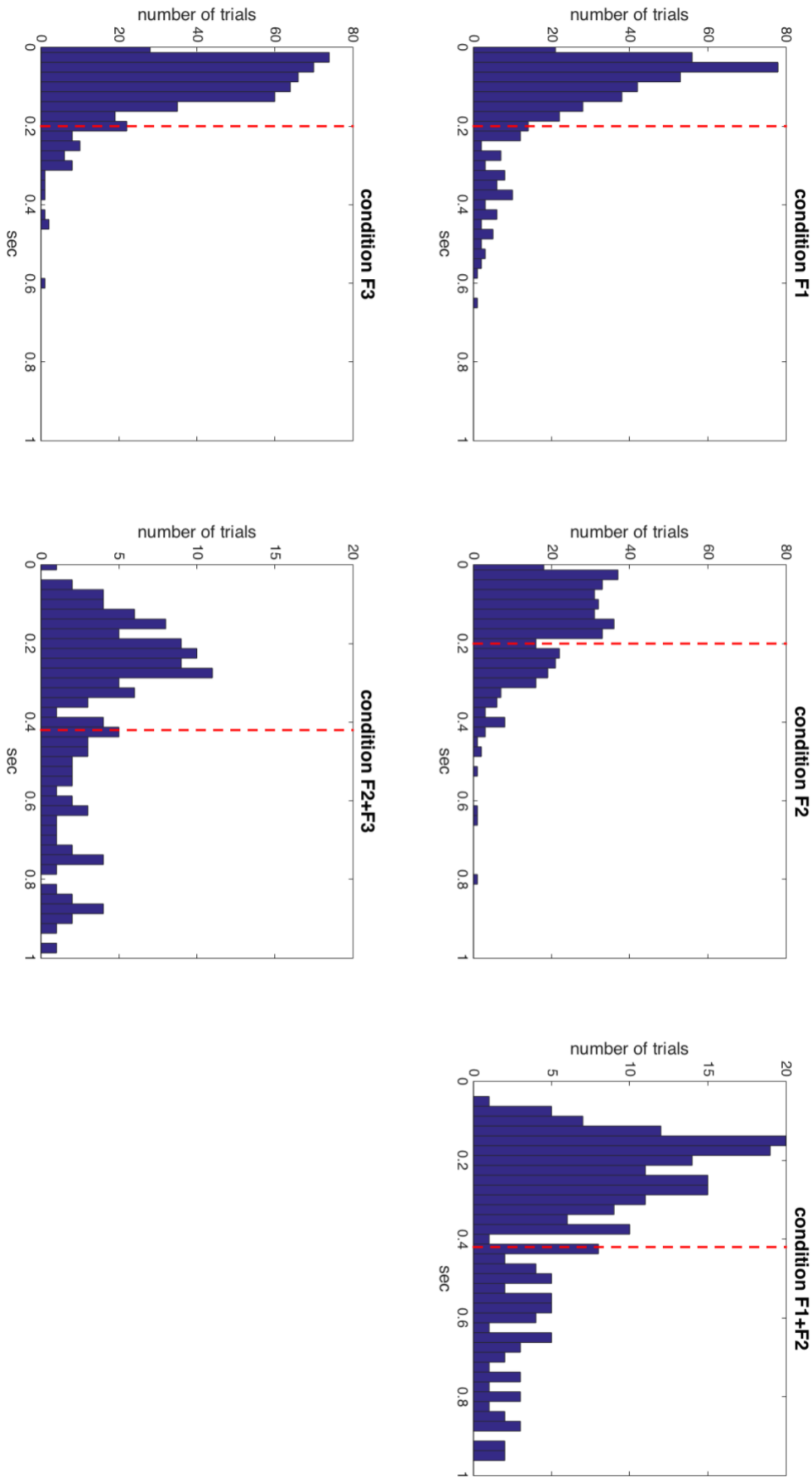
number of trials
sec
condition F1
number of trials
sec
condition F3
number of trials
sec
condition F2
number of trials
sec
condition F2+F3
number of trials
sec
condition F1+F2

3.2 Task Performance

The six recording sessions analyzed in this study were first planned for real-time decoding, when the performance of Monkey M was not fully optimized (Fig. 3.2). Unfortunately, the arrays of this animal had to be explanted just after the six sessions were recorded for reasons not related to this experiment. The percentages of the original correct trials (red + blue in Fig. 3.2) for the five conditions over the six sessions were 49%(F1), 35% (F2), 31%(F1+F2), 57%(F3) and 63%(F2+F3). After additional thresholding, the percentages of thresholded correct trials (blue) were 41%(F1), 24%(F2), 14%(F1+F2), 52%(F3) and 12%(F2+F3). The large percentage drop of the double movements after thresholding was mainly due to thresholding the time between the two presses, not the limitation of RM time (section 2.6). There were on average 212 correct trials per session with a successful rate of 28% across conditions after thresholding.

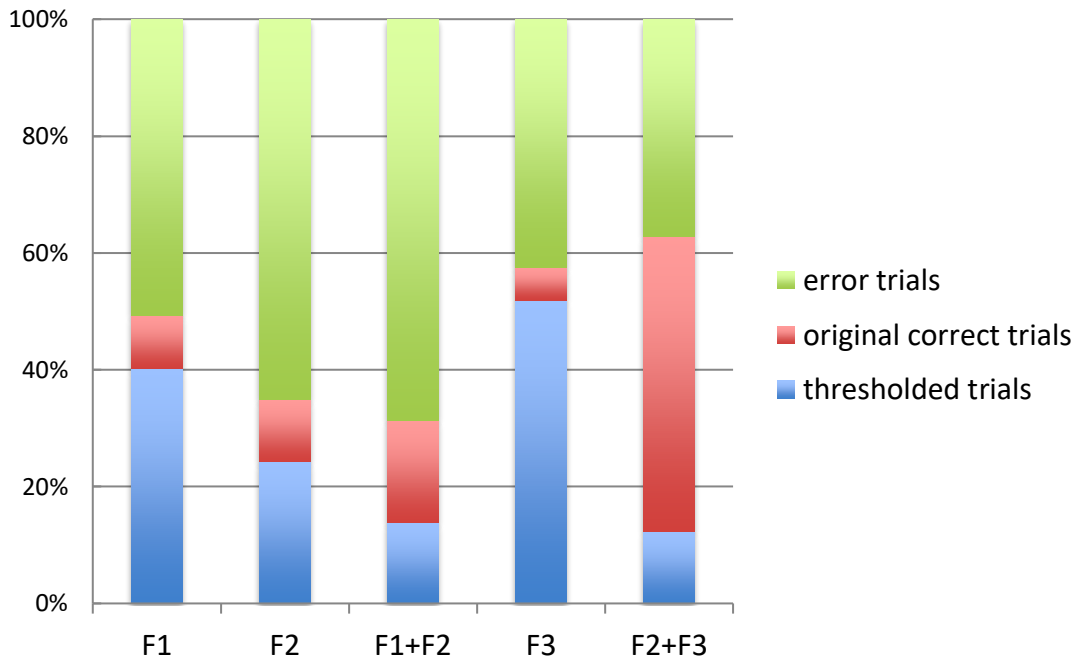

Figure 3.2 Task performance

Performance of the five conditions are shown in percentage. The difference between the original correct trials and the later thresholded trials is marked in red, while the thresholded trials and the error trials are in blue and green. The criteria for thresholding is described previously (see section 2.6).

3.3 Neuronal data and example units

On average, there were 228 single- and multi-units simultaneously recorded from area F5, M1 and AIP per session (Table 3.1).

Table 3.1 Number of units in area F5, M1, AIP recorded in the six sessions

	F5	M1	AIP
Rec4	79	100	64
Rec5	79	104	70
Rec6	71	79	52
Rec7	74	96	60
Rec8	68	81	64
Rec9	64	93	68
mean ± std	72.5 ± 6	92.2 ± 10.1	63 ± 6.4

Fig. 3.3 shows example units from area AIP, F5 and M1, where the five conditions were plotted in different colors. In accordance with previous studies, units in area AIP were modulated during cue presentation, as well as during the movement (Baumann et al., 2009, Lehmann and Scherberger 2013, Murata et al., 2000, Townsend et al., 2011). The AIP unit showed a differential firing pattern after cue onset (cluster-based permutation test, $p<0.05$) and reached its maximal firing rates at the beginning of the hold epoch. F5 units were also modulated from the cue onset to the end of the movement, similar to previous studies (Fluet et al., 2010, Lehmann and Scherberger 2013, Murata et al., 1997, Raos et al., 2006, Rizzolatti et al., 1988, Umilta et al., 2007) with higher firing rates during the hold. Because the task paradigm in this study did not have a memory epoch and the length of the cue epoch was fixed (500 ms), the animal was able to anticipate the go cue during the cue epoch, resulting in the increase of firing rates in the cue epoch. This could be clearly seen in the M1 example unit, similar to a previous study (Poliakov and Schieber, 1999). The firing rates gradually increased from the late cue epoch and reached

maxima at the beginning of the hold epoch, as in object-grasping tasks (Umilta et al., 2007, Schaffelhofer and Scherberger, 2016).

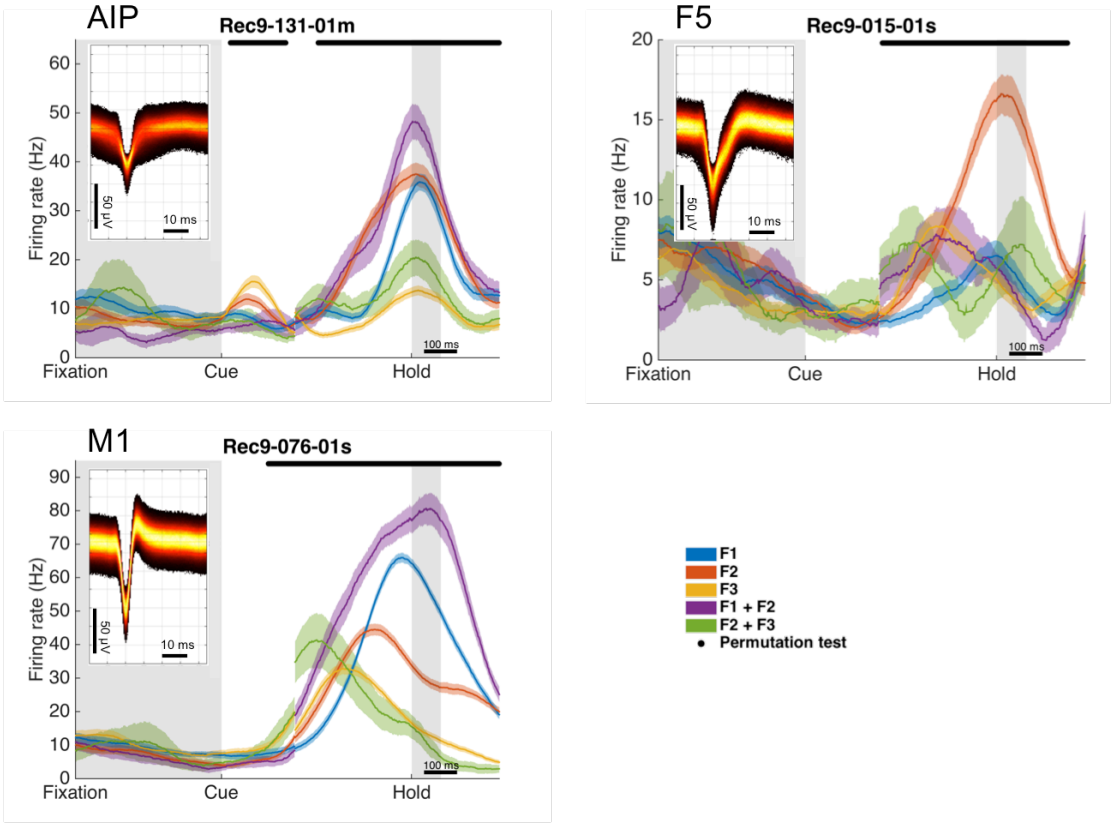

Figure 3.3 Example units from area AIP, F5 and M1

PSTHs showing the five conditions in different colors. Onset of fixation, cue and hold epochs were marked (fixation and hold epoch in gray), while the go signal (cue offset) was not shown due to alignment. Trials were aligned to cue onset (shown up 250 ms after) and hold onset (shown from 400 ms before). Shadows behind curves show standard error. Bars at the top show significant intervals derived from a cluster-based permutation test based on a 1-way-ANOVA ($p < 0.05$). Insets depict spike density plots showing the waveforms. The AIP example is a multiunit. The F5, M1 examples are single units.

3.4 Tuning characteristics

In order to obtain a better overview of the tuning dynamics in the neuronal population, the significant bars (Fig. 3.3) of all units from one area were aligned according to their tuning onset (Fig. 3.4 A). The majority of the units in area AIP and F5 started to be tuned between the onset of the cue and the hold. In the first half of the cue epoch (250 ms), percentage of tuned AIP units (12.3 % in average) was significantly higher than the percentage of tuned F5 (8.1%) and M1 (7.5%) units. Area AIP responded faster and stronger than area F5 and M1 to the presentation of abstract cues indicating movements, similar to when grasping 3D objects (Schaffelhofer and Scherberger, 2016). Likely due to the anticipation of the go signal during the cue epoch and thus the activation of area M1, the percentages of tuned F5 and M1 units in the early cue epoch were at a similar level. The percentage of tuned M1 units exceeded the percentage of tuned AIP and F5 units significantly in the later cue epoch and reached its maximum (69.4 %) shortly before the hold epoch. Area F5 and AIP showed similar patterns with maxima of 62% and 59.9% tuned units, respectively.

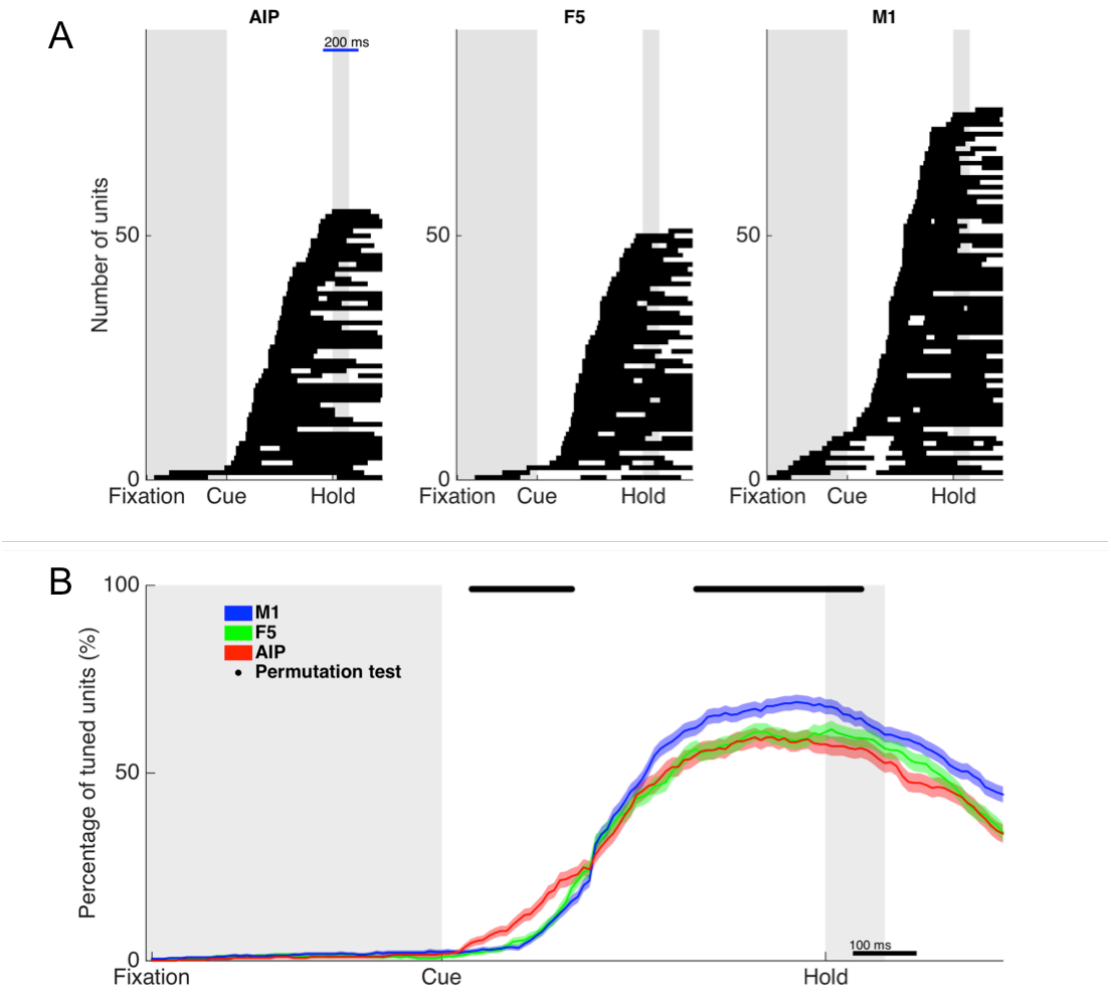

Figure 3.4 Tuning characteristics of units in area AIP, F5 and M1 based on the cluster-based permutation test

A) Tuning onset of one example recording session (Rec9). Individual units in each area were aligned by their time of tuning onset. Onset of fixation, cue and hold epochs were marked as in Fig. 3.3. B) Percentages of tuned units in area AIP, F5 and M1, averaged across six recording sessions, shadows showing standard error. The bar at the top shows significant intervals derived from a cluster-based permutation test based on a 1-way-ANOVA ($p < 0.05$).

3.5 Multiple comparison among conditions

As seen in Fig. 3.3, the M1 example unit increased its firing rate during the cue epoch of the trial for all conditions with different amplitudes. In other words, there are very few units with increased activity for one or two finger movements (Poliakov and Schieber, 1999). Most of the units in M1 are "broadly tuned". Similar firing patterns were observed in area F5 and AIP. Instead of classifying the units according to their increased activity from fixation, we tested whether the firing rates between two conditions are significantly different from each other (ANOVA and post-hoc Tukey-Kramer criterion, $p<0.05$ Bonferroni corrected for the four epochs) separately in the fixation, cue, go and hold epochs. This procedure was done for all possible condition pairs, resulting in ten pairs from five conditions (Fig. 3.5).

These ten condition pairs can be subdivided into four categories: (1) comparisons between single movements (1-2, 1-3 and 2-3, abbreviation: S-S). (2) comparisons between a double movement and one of its related single movement (1-12, 2-12, 2-23 and 3-23, abbreviation: D-rS). (3) comparisons between a double movement and a non-related single movement (1-23 and 3-12, abbreviation: D-nrS). (4) comparison between two double movements (12-23, abbreviation: D-D). Our hypothesis is that the number of neurons firing differently for the S-S condition pairs will be the highest and the number of neurons firing differently for the D-rS will be the lowest, since individuated movements of the thumb, index and middle fingers (S-S category) are more important in daily life than distinguishing movements from D-rS category.

Already in the cue epoch, the firing patterns of the S-S condition pairs showed differences, and the percentage of units tuned for 1-3 condition pair was the highest in all three areas (AIP: 4.3%, F5: 3.8%, M1: 2.3%). In the go and the hold epoch, percentages of tuned units for all condition pairs increased, confirming the results from Fig. 3.4, with the trend of M1 being the highest, followed by F5 and AIP.

To further test the hypothesis of the S-S category being the most important, we first looked at the set of movements involving the thumb and the index finger. It is true for area F5 and M1, the percentages of units tuned for S-S condition pairs were higher than the percentages in the D-rS (1-12, 2-12) and D-nrS (1-23) categories.

However, for the set of movements involving the index and middle finger, there is no such clear pattern. The three condition pairs 2-3 (S-S), 2-23 (D-rS) and 1-23 (D-nrS) are from three different groups but had similar percentages of units tuned. In area AIP, only two D-rS condition pairs (2-12 and 3-23) showed low percentages of tuned units (3.5% and 1.6% respectively) and the other condition pairs had similar level of tuned units. The 3-23 condition pair also showed the lowest percentage of tuned units in area F5 (4.3%) and M1 (7.7%). This is an indication that the index finger often moved with the middle finger during individuated middle finger movement, but not vice versa. The number of units tuned for 2-23 condition pair was higher (F5: 10%, M1: 20.4%), suggesting the importance to have individuated index finger movement.

Figure 3.5 Multiple comparison among conditions (opposite page)

The differences between all possible condition pairs were tested with Tukey-Kramer test separately ($p<0.05$, Bonferroni corrected) for each area and epoch. The labeling for the five conditions were simplified as 1, 12, 2, 3, 23 and the conditions pairs were written as combination of two conditions, e.g. 1-12 for the condition pair between F1 and F1+2. For each condition pair, the percentage of units with significant firing rate difference between the conditions was plotted with standard deviation from different recording sessions. There are in total ten condition pairs resulting from five conditions. The cue epoch shown here was the first 250 ms of the cue epoch, in order to have less influence from the anticipation of the go signal. The go epoch was chosen to be 100 ms before the hold, according to the reaction + movement time histogram (Fig. 3.1). Only units with average firing rates > 5 Hz were included.

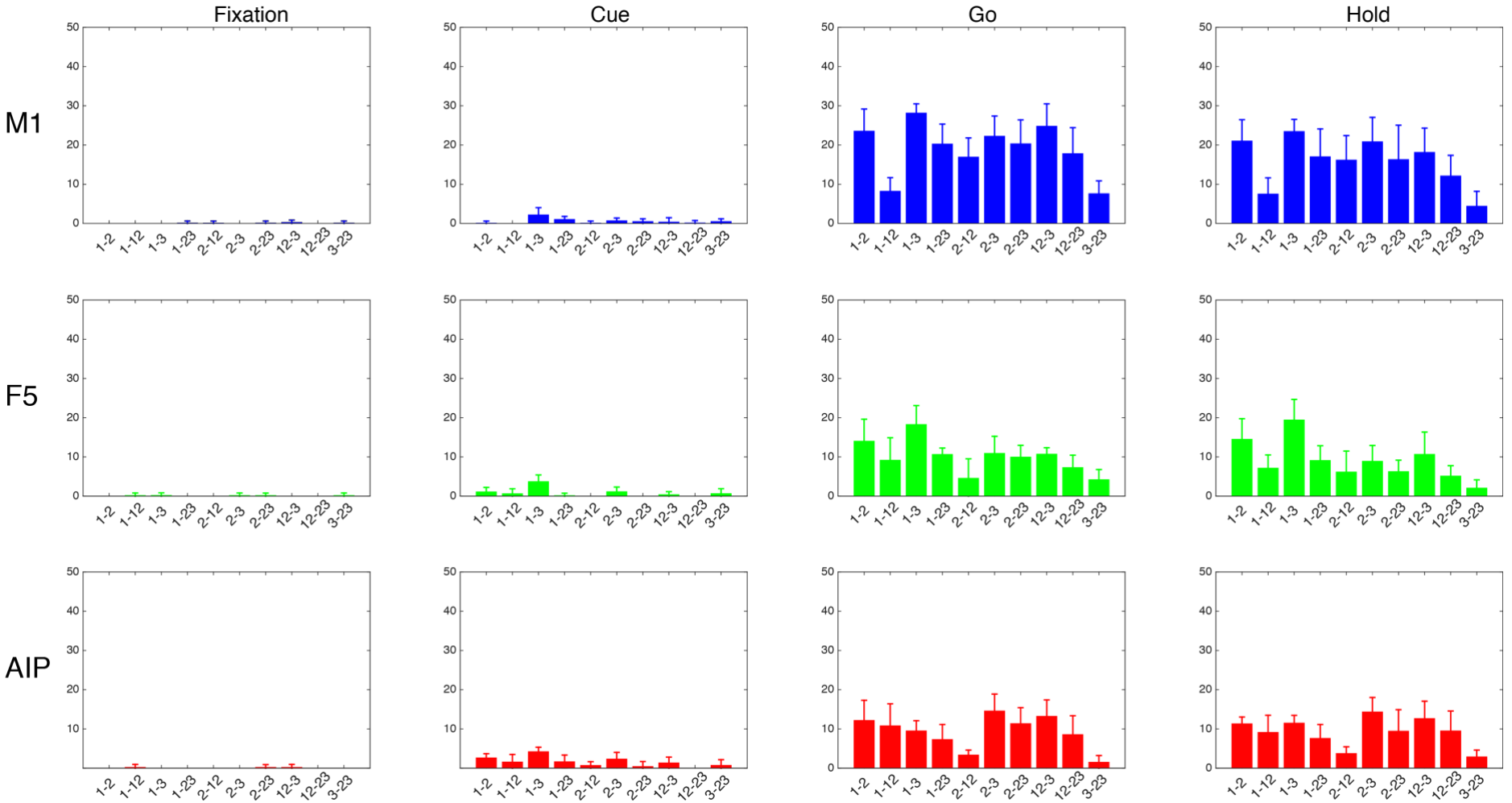
Fixation
Cue
Go
Hold
M1
F5
AIP
0
10
20
30
40
50
1-2
1-12
1-3
1-23
2-12
2-3
2-23
12-3
12-23
3-23

3.6 Partial correlation between error trials and their corresponding correct trials

The different trends of the percentages of tuned units in the three areas (Fig. 3.4 B), as well as the multiple comparison of the condition pairs in different epochs (Fig. 3.5), revealed the different roles of area AIP, F5 and M1 in the visuomotor transformation process. The partial correlation coefficients (pcc) between the error trials and their corresponding correct trials ("cue error pcc" and "movement error pcc", section 2.10) could further disentangle the visual information from the movement information.

Table 3.2 Error trial categories in the six sessions used for partial correlation analysis

The "cue" column shows the original cue (instructed movement which was not correctly performed) of each error trial category, and the "wrong press" column shows the movement performed, which was one of the other four movements in the task. The labeling of the five conditions was simplified as in Fig. 3.5. Each row represents one error trial category, and only categories with more than five trials were used for analysis. The number of error trial categories in each session is shown in the last raw.

cue	wrong press	*Rec4*	*Rec5*	*Rec6*	*Rec7*	*Rec8*	*Rec9*
2	1	x	x	x	x		
2	12	x	x	x	x		
2	3		x				
2	23		x	x	x	x	x
12	2	x					
12	3		x	x			
12	23	x	x			x	x
3	2		x	x		x	x
3	23	x	x				
Total number		5	8	5	3	3	3

Table 3.2 shows the error trial categories selected for the pcc analysis. Out of 20 possible error trial categories, only nine had more than 5 trials. Among these nine

categories, there are only three different cues (2, 12 and 3), suggesting that these movements were more difficult for the monkey (true for 2 and 12, Fig. 3.2) or when instructed for one of these movements, it was likely to perform another movement. For example, when instructed for individuated index or middle movement, both fingers could move together (cue 2, wrong press 23 or cue 3, wrong press 23). For cue 2, all the possible four wrong presses appeared, while for cue 12 and cue 3, only three and two possible wrong presses were performed. Although only three different cues appeared, all five movements were performed as wrong presses.

Fig. 3.6 shows the "cue error pcc" and the "movement error pcc" of three error trial categories from one example session during the course the trial. The "cue error pcc" in the first category "Cue2 Press23" (first row in Fig. 3.6) was higher than the "movement error pcc" during the entire trial in area AIP. In area F5 and M1, it was higher before the monkey initiated the movement (ca. 100 ms before hold) and the "movement error pcc" exceeded it before the hold epoch. The "movement error pcc" value during the hold epoch was larger in area M1 than in area F5. In the other two categories (Cue12 Press23 and Cue3 Press2), the "cue error pcc" and the "movement error pcc" fluctuated at a similar level till early cue epoch, and showed similar patterns as in the first category. The unexpected high "cue error pcc" values during fixation epoch in the first category could be due to the pseudorandom order of the cue presentation. When one of the cues was poorly performed and often left in the pool, the monkey could potentially anticipate the coming cue. However, when comparing with other categories of other sessions, the values in the first category were still in the fluctuation range (data not shown).

Figure 3.6 Partial correlation coefficients between error and correct trials (opposite page)

Partial correlation coefficients (R^2) of all error trial categories and the average from one example session (Rec9, Table 3.2). "Cue error pcc (red)" and "movement error pcc (blue)" plotted separately for each error trial category and for each area. Onset of fixation, cue and hold epochs were marked (hold epoch in gray). Trials were aligned to cue onset (250 ms after) and hold onset (350 ms before).

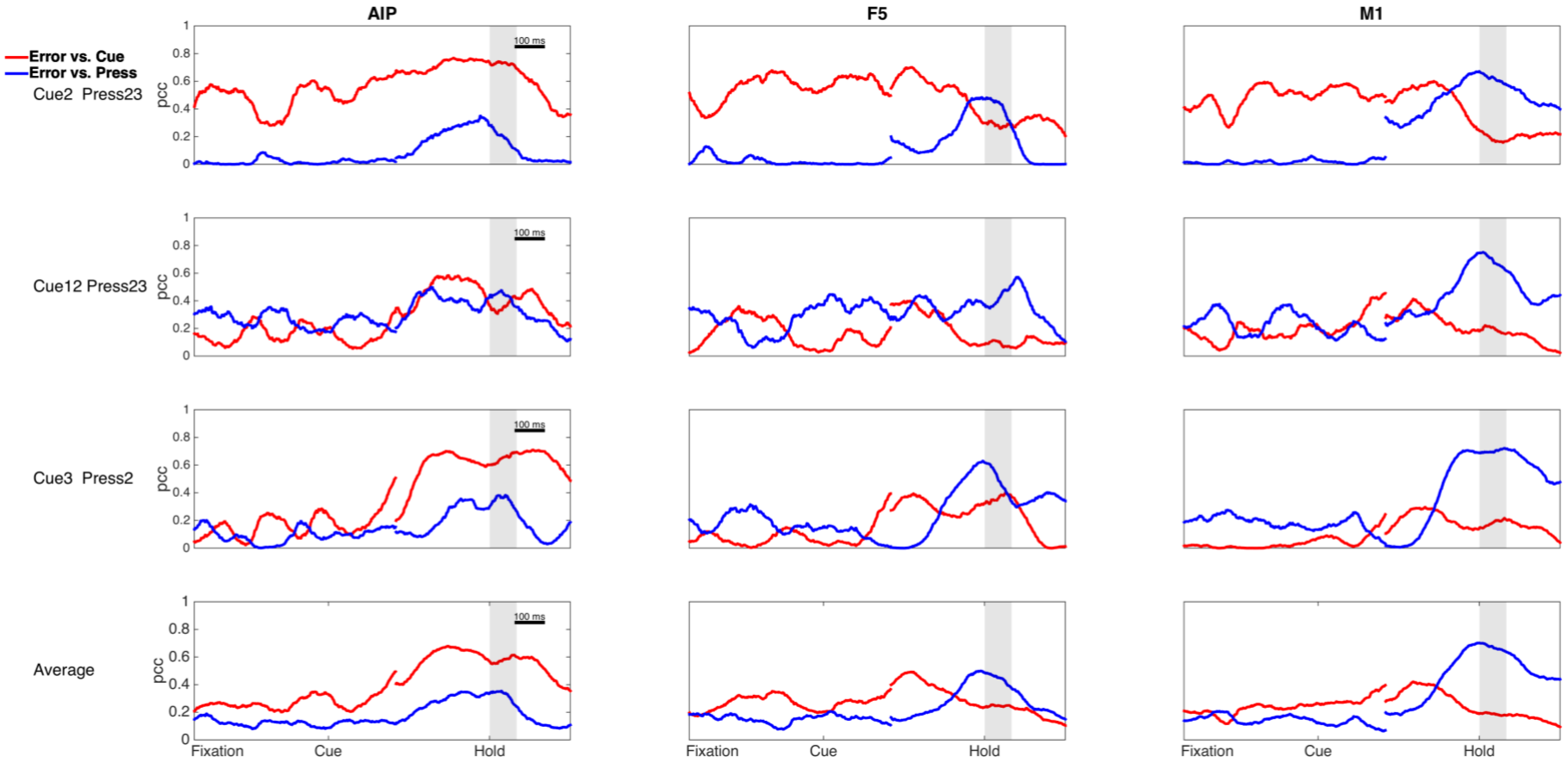
AIP
F5
M1
Error vs. Cue
Error vs. Press
Cue2 Press23
Cue12 Press23
Cue3 Press2
Average
pcc
100 ms
Fixation
Cue
Hold

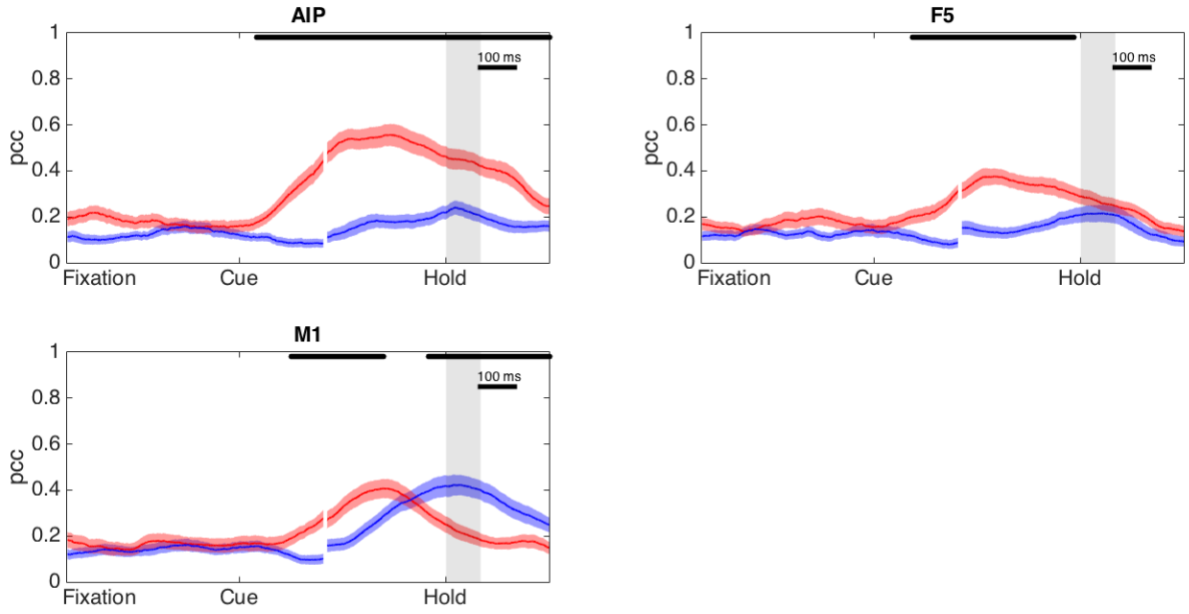

Figure 3.7 Averaged partial correlation coefficients between error and correct trials

Averaged partial correlation coefficients (R^2) over the 27 error trial categories from six sessions (Table 3.2). "Cue error pcc (red)" and "movement error pcc (blue)" plotted separately for each area, shadows showing standard error. Trial alignment and labels are the same as in Fig. 3.6. Bars at the top show significant intervals derived from a cluster-based permutation test based on a 1-way-ANOVA ($p < 0.05$).

The average of the three categories from the example session describes the different roles of the three areas, and the average over all 27 categories from six sessions (Fig. 3.7) further confirmed this trend: The more visually associated area AIP showed gradually increased "cue error pcc" after cue onset and reached its maximum ca. 200 ms before the hold epoch. The "cue error pcc" maintained at a relatively high level during the movement and dropped after the hold epoch. The "movement error pcc" in area AIP also showed a similar pattern with smaller amplitude. Area F5 is where the visual information and the motor preparation intercross. There are two peaks of pcc values, the first peak from the "cue error pcc" around 300 ms before the hold epoch and the second peak from the "movement error pcc" at the onset of the hold epoch. Although when averaging over all the error trial categories in six sessions, the second peak is less obvious than the average from the example session (Fig. 3.6). Because the "cue error pcc" dropped to a level similar to the weakly increased "movement error pcc" during the hold epoch (Fig. 3.7), there was no significant

difference between the two. The “cue error pcc” and the “movement error pcc” in area M1 also have a double-peak structure (cluster-based permutation test, $p<0.05$). The “cue error pcc” peak was a bit later compared to the peak in area F5, suggesting the upstream-downstream relationship of these two areas. The “movement error pcc ” in both areas had a peak at the onset of the hold epoch, reflecting the precise timing of movement control.

3.7 Neural trajectories in the PCA space

Similar to the temporal complexity and heterogeneity at the single-neuron level discovered in motor and premotor cortex (Churchland and Shenoy, 2007), units recorded in area AIP, F5 and M1 in this study also showed diverse differential firing patterns (Fig. 3.8).

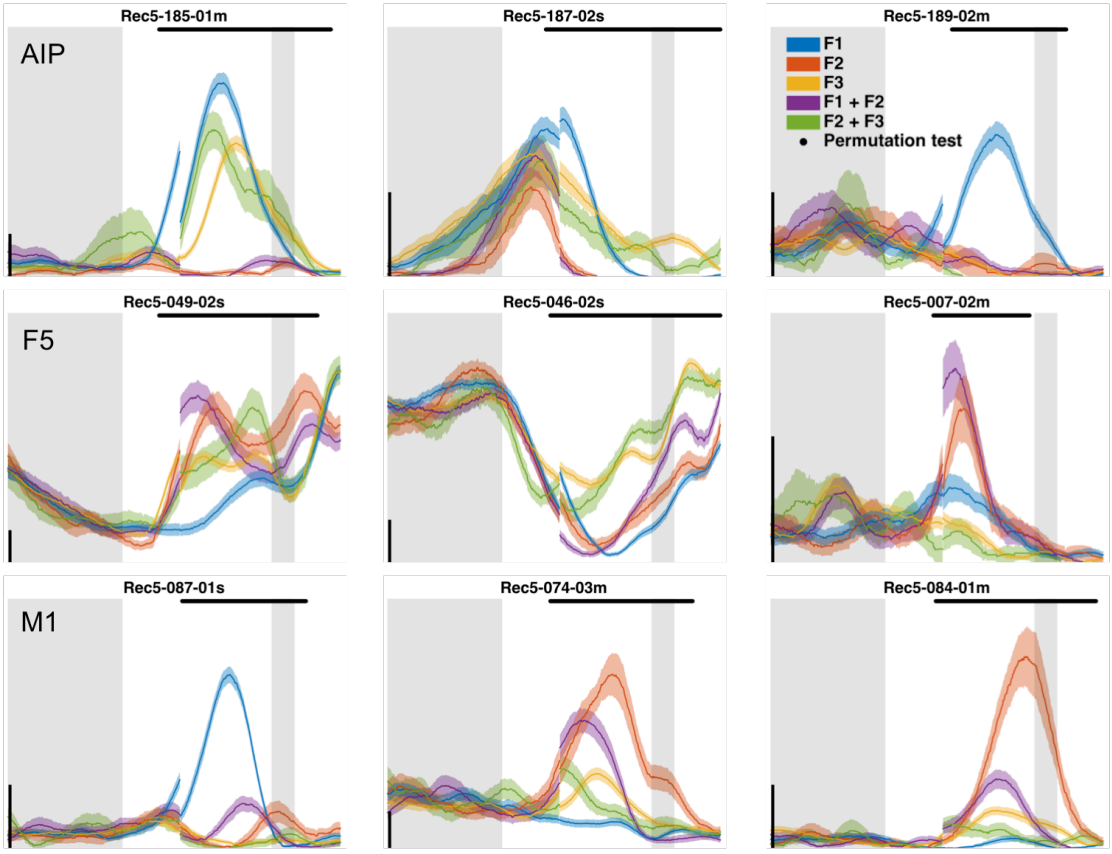

Figure 3.8 Diverse firing patterns of single neurons

PSTHs of nine example units from area AIP, F5 and M1 (top, middle and bottom rows) showing diverse firing patterns. Trial alignment, labels and significant bars at the top are the same as in Fig. 3.3. Vertical calibration bars show firing rate of 5 Hz.

For example, in area AIP, unit Rec5-189-02m was tuned for F1 from late cue epoch till the end of hold epoch, while unit Rec5-185-01m responded earlier in the cue epoch for F1, F2 + F3 and F3 movements. Rec5-046-02s in area F5 decreased firing rates during cue presentation and movement initiation. In area M1, Rec5-074-03m and Rec5-084-01m both had maximum amplitude for F2 movement, followed by F1 + F2 movement, but with distinct patterns for all five conditions. Alignments of tuning onset (Fig. 3.4 A) from the three areas show gradual changes of the temporal

coding patterns and it would be arbitrary to classify units according to their firing rate profiles in a given period of the trial.

In order to see all the units as a whole, each recorded unit could be considered as one dimension in a state-space, and the population firing rates evolving over time form a neural trajectory through this space (Shenoy et al., 2013). We performed principal component analysis (PCA) on the PSTHs of all units from each area (section 2.11). Plotting the first three principal components (PCs) yields a low-dimensional trajectory that can be visualized and still represents >75% of the total variance of the original neural data.

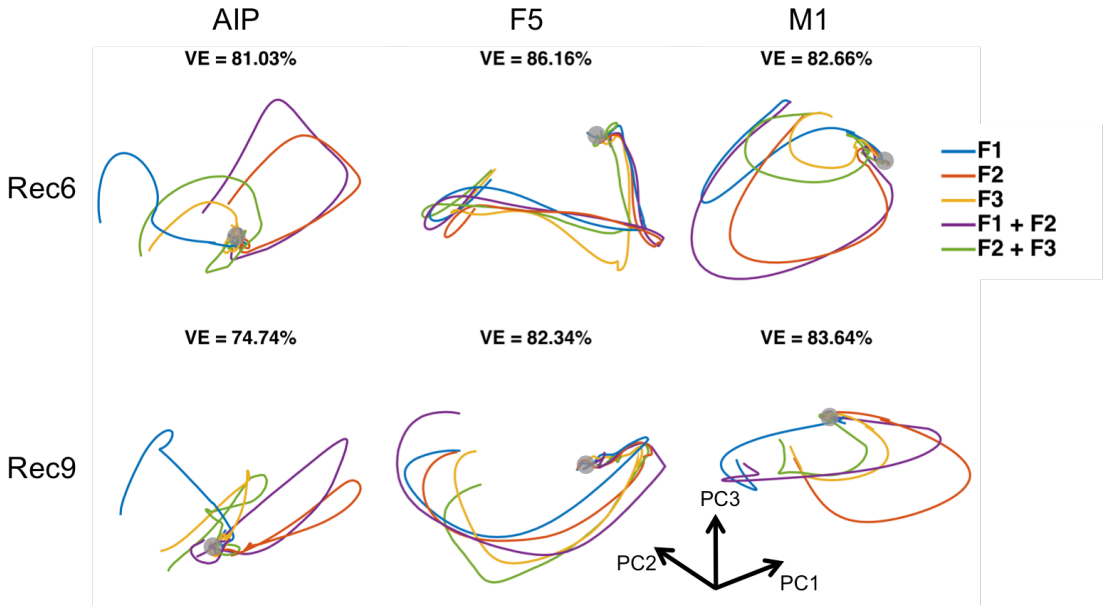

Figure 3.9 Neural trajectories in the PCA space

Neural trajectories of the five conditions (labeled in different colors) in area AIP, F5 and M1 from two example recording sessions (Rec6 and Rec9). PSTHs of all units from each area were PCA transformed and the population firing rates can be visualized as neural trajectories by plotting the first three PCs. The alignment of the trials was slightly different from Fig. 3.3 to obtain smoother trajectories (250 ms after cue onset and 350 ms before hold onset). Gray circles show start of the trials. The cumulative variance explained (VE) from the first three PCs was listed on top of each subplot.

Fig. 3.9 shows the neural trajectories of the five conditions in area AIP, F5 and M1. Note that a neural trajectory doesn't travel necessarily the same distance between each time interval, but extends larger distance when the population firing rates change dramatically. Take a classical delayed reaching task as example, the distance

between the baseline and the prepare-and-hold state (go cue onset) is relatively short, comparing to the distance traveled during the reaching movement (Ames et al., 2014). In this study, it is difficult to observe how the trajectory evolved between the prepare-and-hold state and the movement onset, because there was no memory epoch and no detection of movement onset (section 2.6). The baseline (fixation epoch) and the cue onset appeared within a very small area in the PCA space. In Fig. 3.9, they are mostly covered by the gray circle and indicated as "start". The most part of a trajectory plotted in the PCA space represents how the population firing rates evolve during the movement.

In area AIP, the trajectories of the five conditions showed the most divergence (Fig. 3.9 Left). The relative positions of the trajectories did not follow the cue design, which was based on the anatomy of the right hand (F1-F2-F3, Fig. 2.1 B). The ordering of the trajectories in the AIP PCA space was F1-F3-F2 (blue, yellow and red trajectories). This showed that when using abstract cues to indicate different movements, area AIP seems to code information related to movement preparation and does not necessarily reflect the physical properties of the cues (e.g. position of the cues). However, when the movement is to grasp visible objects, these objects are represented based on their shapes in the AIP neuronal population space (Schaffelhofer and Scherberger, 2016).

The neural trajectories in area F5 were surprisingly the least diverse. The five trajectories traveled in the same direction and ended within a small area, compared to the end points in area AIP. However, the percentage of F5 units tuned in the cue epoch was similar to area M1 and the percentage of units tuned during the movement was similar to area AIP (Fig. 3.4 B). This can be seen from the distance between the five conditions. They were close to each other but separable, comparing to trajectories in the other two areas.

M1 trajectories were similar to the ones in AIP. F1 and F2 trajectories were far apart from each other and F3 trajectory was in between, with a shorter route traveled. In both areas, F1 + F2 (purple trajectory) was closer to F2 (red trajectory) and F2 + F3 (green trajectory) was closer to F3 (yellow trajectory). This shows that the population firing rates of the double movements resemble one of the two single

movements more than the other. The trajectory endpoints in M1 seemed to be more converged than the endpoints in AIP, showing that the population firing rates for flexion of different fingers probably represent a pattern following the dynamics of the muscles. In contrast, the trajectory endpoints in AIP seemed to be more diverged, which could be serving as working memory (Schaffelhofer and Scherberger, 2016).

3.8 Demixed principal component analysis

PCA is an unsupervised dimensionality reduction technique, which captures the maximum variance in the data. However, it could be sometimes difficult to observe the different patterns the experiment was aiming for, because the proportion of variance contributed by the experimentally designed dependent variables might not be large enough to be captured by the first few PCs. The neural trajectory in the F5 PCA space is an example of this scenario (Fig. 3.9). The first three PCs explained more than 80% of the total variance, but the trajectories of the different conditions traveled in a same manner within the first-three-PC space. Thus visualization of the inter-conditional differences in area F5 by plotting the first three PCs is suboptimal. Demixed principal component analysis (dPCA) conquers this problem by decomposing population activity into components based on the designed task parameters (section 2.12). In this study, the two parameters are the condition-dependent and the time-dependent (condition-independent) components (Fig. 3.10). The purpose of this technique is to "demixed" the two parameters while maintaining the maximum variance explained in the dimension reduced data. The cumulative variance explained by the demixed principal components (dPCs, red) is similar to the cumulative variance explained by the principal components (PCs, black) in all three areas, confirming the validity of dPCA (Fig. 3.10 A, D and G).

Among the three areas, area AIP had the largest proportion of variance explained by the condition-dependent components (57%, pie chart in Fig. 3.10 B). This can be seen in detail at the first three dPCs (ranked by variance explained, VE), which included two condition-dependent components (#1, 29.5% VE and #3, 11.2% VE) and only one condition-independent component (#2, 29.3%). This is congruent with the neural trajectories obtained from the PCA space, where the neural trajectory pattern in area AIP was the most diverse (Fig. 3.9). When projecting the neural data onto the decoder axes of the condition-dependent dPCs, the five conditions were well separated (Fig. 3.10 C, top row). Similar to the trajectories in PCA space, F1 + F2 (purple) was closer to F2 (red) and F2 + F3 (green) resembled more F3 (yellow).

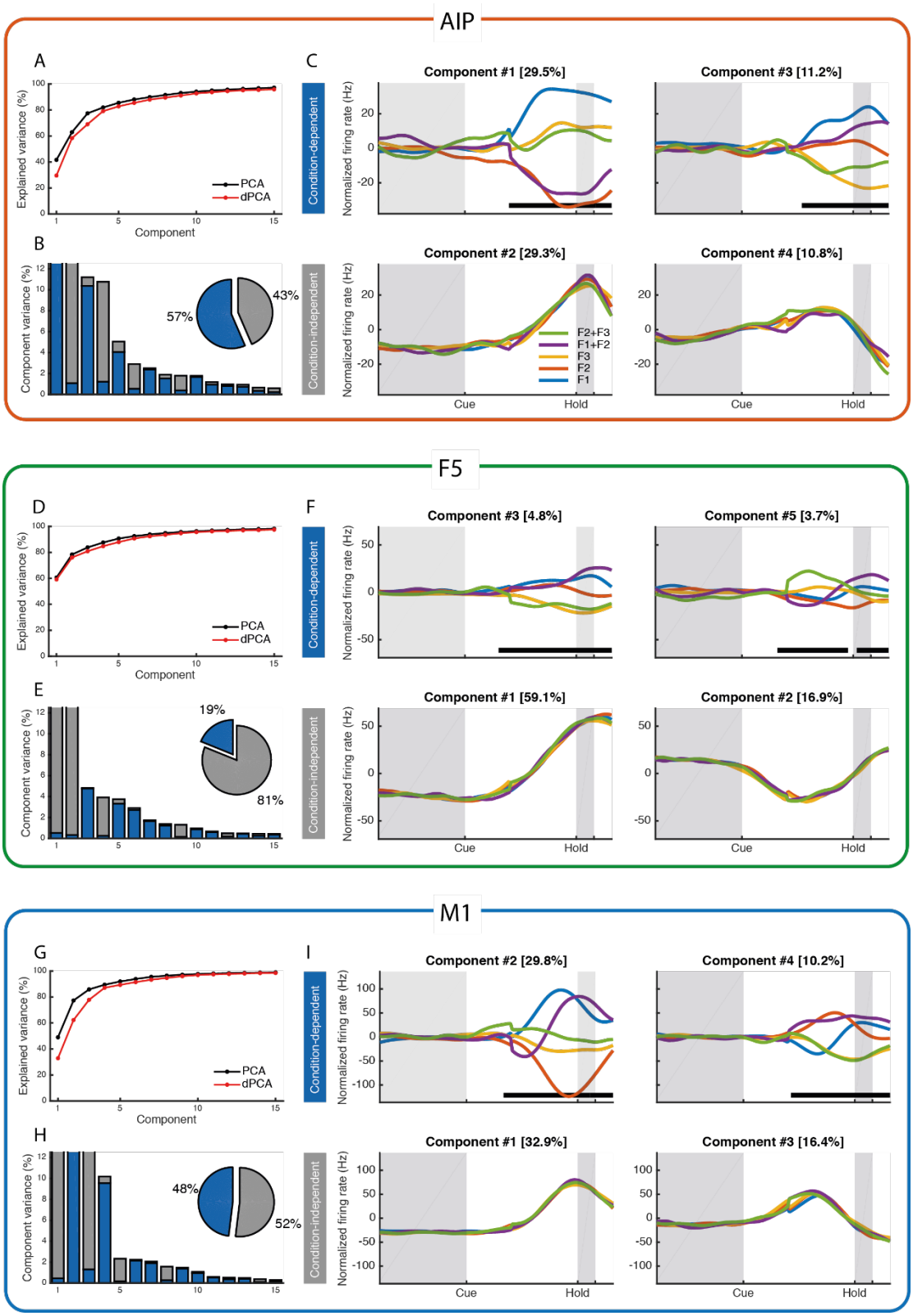
AIP
A
Explained variance (%)
Component
PCA
dPCA
B
Component variance (%)
57%
43%
C
Condition-dependent
Condition-independent
Component #1 [29.5%]
Component #3 [11.2%]
Component #2 [29.3%]
Component #4 [10.8%]
Normalized firing rate (Hz)
F2+F3
F1+F2
F3
F2
F1
Cue
Hold
F5
D
E
19%
81%
F
Component #3 [4.8%]
Component #5 [3.7%]
Component #1 [59.1%]
Component #2 [16.9%]
M1
G
H
48%
52%
I
Component #2 [29.8%]
Component #4 [10.2%]
Component #1 [32.9%]
Component #3 [16.4%]

Figure 3.10 Demixed principal component analysis of AIP, F5 and M1 population activity (opposite page)

Demixed component analysis of one recording session (Rec9). Area AIP, F5 and M1 were analyzed separately (top, middle and bottom boxes). A) Cumulative variance explained by the first 15 principal components (PCs, black) and demixed principal components (dPCs, red). B) Variance of the individual dPCs. Each bar shows the proportion of total variance, and is composed out of two stacked bars: blue for condition-dependent variance and gray for condition-independent variance. Each bar appears to be single-colored, which signifies nearly perfect demixing. Pie chart shows how the total signal variance is split between condition-dependent and condition-independent. C) First two condition-dependent components (top row) and first two condition-independent components (bottom row). In each subplot, the full data are projected onto the respective dPCA decoder axis, so that there are five lines corresponding to five conditions (legend in the bottom left subplot). Trial alignment for dPCA was 250 ms after cue onset and 380 ms before hold onset. Onset of the cue and the hold epoch are marked (fixation and hold epoch in gray). Length of the hold epoch indicates 100 ms. Black lines at the bottom show time intervals during which the conditions can be reliably decoded from single-trial activity (section 2.12). Note that the vertical scale differs across areas. Ordinal number and variance explained in percentage of each component is shown on top of each subplot. D-F) same as A-C for area F5. G-I) same as A-C for area M1.

This was observed in the first two condition-dependent components. The first condition-independent component (Component #2) was modulated by movement and time, while the second one (Component #4) also showed mild visuomotor transition in the early cue epoch (Fig. 3.10 C, bottom row).

The variance explained by the condition-dependent components in area F5 (19%) was similar to two other studies of delayed grasping with precision and power grips (in ‘t Veld, 2016; Michaels and Scherberger, 2018), while this percentage in area AIP (57%) and area M1 (48%) were much higher than from the grasping studies (Fig. 3.10 B, E and H). The first two condition-dependent components in area F5 were Component #3 and Component #5 with 4.8% and 3.7% VE, respectively. However, conditions can be decoded from these two dPCs from the late cue epoch to the end of the trial (Fig. 3.10 F, top row). The first condition-independent component was the largest component (59.1%), modulated strongly by the movement.

Area M1 had similar proportion of variance explained by the condition-dependent and the condition-independent components (Fig. 3.10 H). In the first condition-dependent component (Component #2), the F1 (blue) and F2 (red) lines reached their maximum absolute value (normalized firing rate) shortly before the hold epoch and decreased during the hold epoch, in contrast to area AIP, where the signal was maintained till the end of the trial (Fig. 3.10 C and I). This can also be observed from

the neural trajectories in PCA space where the AIP endpoints were more spread out than the M1 endpoints (Fig. 3.9).

In summary, both PCA and dPCA can be used to visualize the population firing pattern of simultaneously recorded neurons. The differences among area AIP, F5 and M1 can be observed with PCA, and with the first four dPCs in Fig. 3.10, patterns similar to the trajectories in PCA space appeared, since PCA and dPCA are related methods. The advantage of dPCA is to find variance explained by the experimentally designed parameters. This is often important because the population firing rate differences between conditions could be relatively small, compared to common firing rate changes in the trial, for example, during movements. In this study, this is the case for area F5, where the separation in PCA space is suboptimal, while the condition-dependent components obtained from dPCA can clearly show the condition-dependent changes of the population firing rates over time.

3.9 Euclidean distance between the neural trajectories

In order to quantify the differences between conditions, we calculated the Euclidean distance between two trajectories in the neuronal state-space. However, there are two problems one has to consider. First, distance is a measurement between two points. When there are multiple experimentally designed conditions, it creates a multiple comparison problem. The number of condition pairs is larger than the number of conditions. In section 3.5, we classified the ten condition pairs resulting from five conditions into four categories. We can thus first search for the difference among the categories and then compare in detail specific condition pairs. Second, the neural trajectories are functions of time. The selection of time points or intervals within a trial to calculate distance is critical to obtain meaningful results. Previous studies either calculated the minimum distance near the epoch onsets (Ames et al., 2014), or use the average firing rate within one epoch (Schaffelhofer and Scherberger, 2016). We used the average firing rate method to have an overview of the four categories, and for specific condition pairs, we calculated the Euclidean distance between the neural trajectories for each time point separately.

Fig. 3.11 A shows the normalized Euclidean distances of all ten condition pairs over time from one example recording session. Here, the condition pairs were colored according to the four categories (the D-rS was separated further into the F12 and F23 groups). In all three areas, the lines in the S-S category (red) had the maximum magnitude, and the D-nrS lines (purple) were above the D-D line (pink).

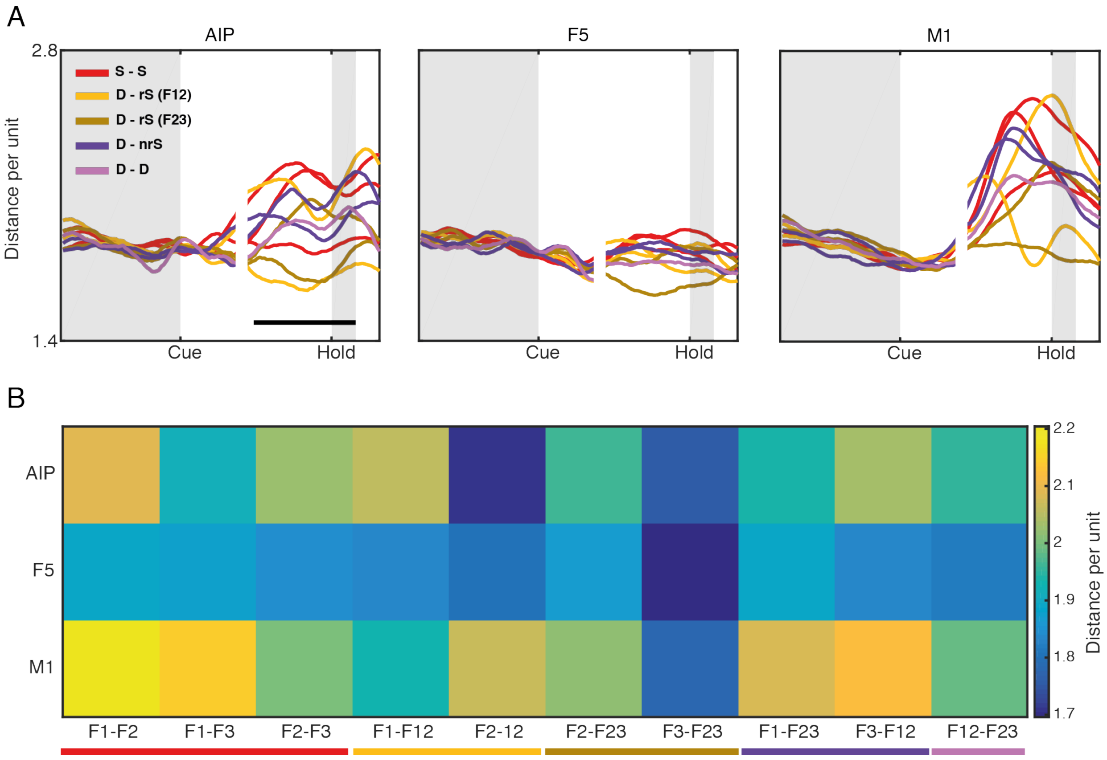

Figure 3.11 Distance analysis of condition pairs

A) Distance analysis of all ten condition pairs from one example recording session (Rec7). Normalized Euclidean distances plotted as functions of time separately for area AIP, F5 and M1. Distances were normalized by the square root of the number of units within each area (distance per unit). The ten condition pairs were plotted with five different colors (legend in the left subplot), representing comparison between two single movement (S-S, red), double movements with its related single movements (D-rS, yellow for F12 group and brown for F23 group), double movements with unrelated single movements (D-nrS, purple) and two double movements (D-D, pink). Trial alignment was the same as for dPCA (250 ms after cue onset and 380 ms before hold onset). Onset of the cue and the hold epoch are marked (fixation and hold epoch in gray). Length of the hold epoch indicates 100 ms. The black line at the bottom of the left subplot shows the time interval used to calculate the colormap in B. B) Summary plot of distance analysis. Colormap shows the average distance (from the late cue epoch to the end of the hold epoch) for all ten condition pairs in area AIP, F5 and M1 (averaged across six recording sessions). The ten condition pairs are marked at the bottom with the same colors as in A.

This shows that the distances between single movements (S-S) were the largest, followed by the distances between the double movements and its unrelated single movements (D-nrS, only F1-F23 and F3-F12 when three fingers were instructed). The distance between the two double movements (D-D, F12-F23), having one finger overlapping, was smaller than the D-nrS distances. However, there were lines not following this logic. In area AIP, there was one S-S line (red) not modulated during movement, and in area M1, there was one S-S line clearly beneath the D-nrS line

(purple). Furthermore, it was difficult to find clear patterns for the two groups in the D-rS category (yellow and brown). In area AIP and M1, there were one line in each group having relatively high magnitude and the other having relatively low magnitude.

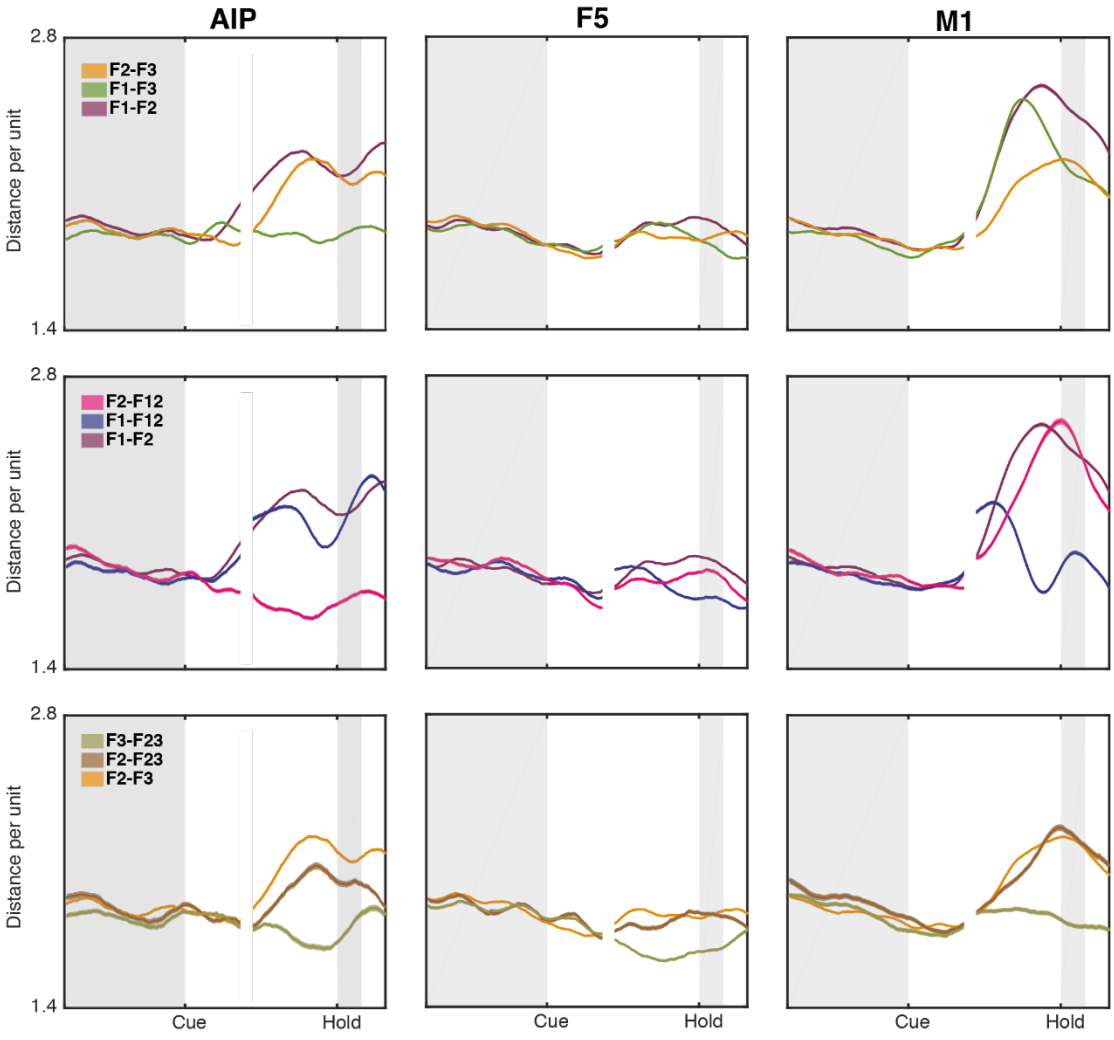

Figure 3.12 Distance analysis of selected condition pairs from one example recording session

Distance analysis of S-S (top row), and D-rS categories (F12 group, middle row, and F23 group, bottom row) in area AIP, F5 and M1 from one example recording session (Rec7). The three S-S condition pairs (F1-F2, F1-F3 and F2-F3) were plotted in different colors (legend in the AIP subplot). For the F12 and F23 groups, one S-S condition pair related to the double movement was included (plotted in the same color as in the top row). Shadows show standard error from single-trial based method (section 2.13). Trial alignment, and mark of epoch onsets are the same as in Fig. 3.11 A.

In order to have a precise view of the S-S category, we plotted the normalized distances of the three condition pairs in different colors (Fig. 3.12 and 3.13, top rows). In all three areas, F1-F2 lines had the largest magnitude from the late cue

epoch till end of the trial. However, the pattern for F2-F3 and F1-F3 in area AIP was different from the pattern in area M1. In area AIP, F1-F3 seemed not to be modulated by movement, while in area M1, F1-F3 had a peak before onset of the hold epoch, similar to F1-F2. This can be observed from the example recording session (Fig. 3.12), as well as from the averaged results of the six recording sessions (Fig. 3.13). Note that the distance analysis was based on a single-trial method (section 2.13), and the standard error was plotted as shadows in Fig. 3.12. However, the standard error was very small, compared to the standard error from PSTH of neurons (Fig. 3.8). In the F23 group (Fig. 3.12 bottom row), the standard error is more visible. In area F5, the F1-F3 line was slightly above the F2-F3 line, but the differences between the normalized distances were not significant (cluster-based permutation test, $p>0.05$, Fig. 3.13 top row). Congruent with the neural trajectories in PCA space having more diverse endpoints in area AIP (Fig. 3.9), the modulation in area AIP started earlier and ended later, compared to area M1 (Fig. 3.13 top row). The distance analysis of condition pairs provided an opportunity to test the differential patterns observed in the PCA space statistically.

In the F12 group, the discrepancy between area AIP and M1 appeared again. In area AIP, like the F1-F3 in the S-S category, F2-F12 seemed not to be modulated by movement, while in area M1, F2-F12 had a magnitude similar to F1-F2 from the S-S category (Fig. 3.12 and 3.13 middle rows). Interestingly, this discrepancy was also discovered at the single-neuron level. In section 3.5, the percentages of units tuned for F1-F12 and F2-F12 (having different firing rates between the two conditions linked by the dash line) in area AIP and M1 were very different during movement. In area AIP, more units tuned for F1-F12 (F1-F12: 10.9%, F2-F12: 3.4%), and in area M1, more units tuned for F2-F12 (F1-F12: 8.3%, F2-F12: 17%, Fig. 3.5). However, the discrepancy between area AIP and M1 didn't appear in the F23 group. The normalized distance of F3-F23 was the smallest in all three areas (Fig. 3.12 and 3.13 bottom rows).

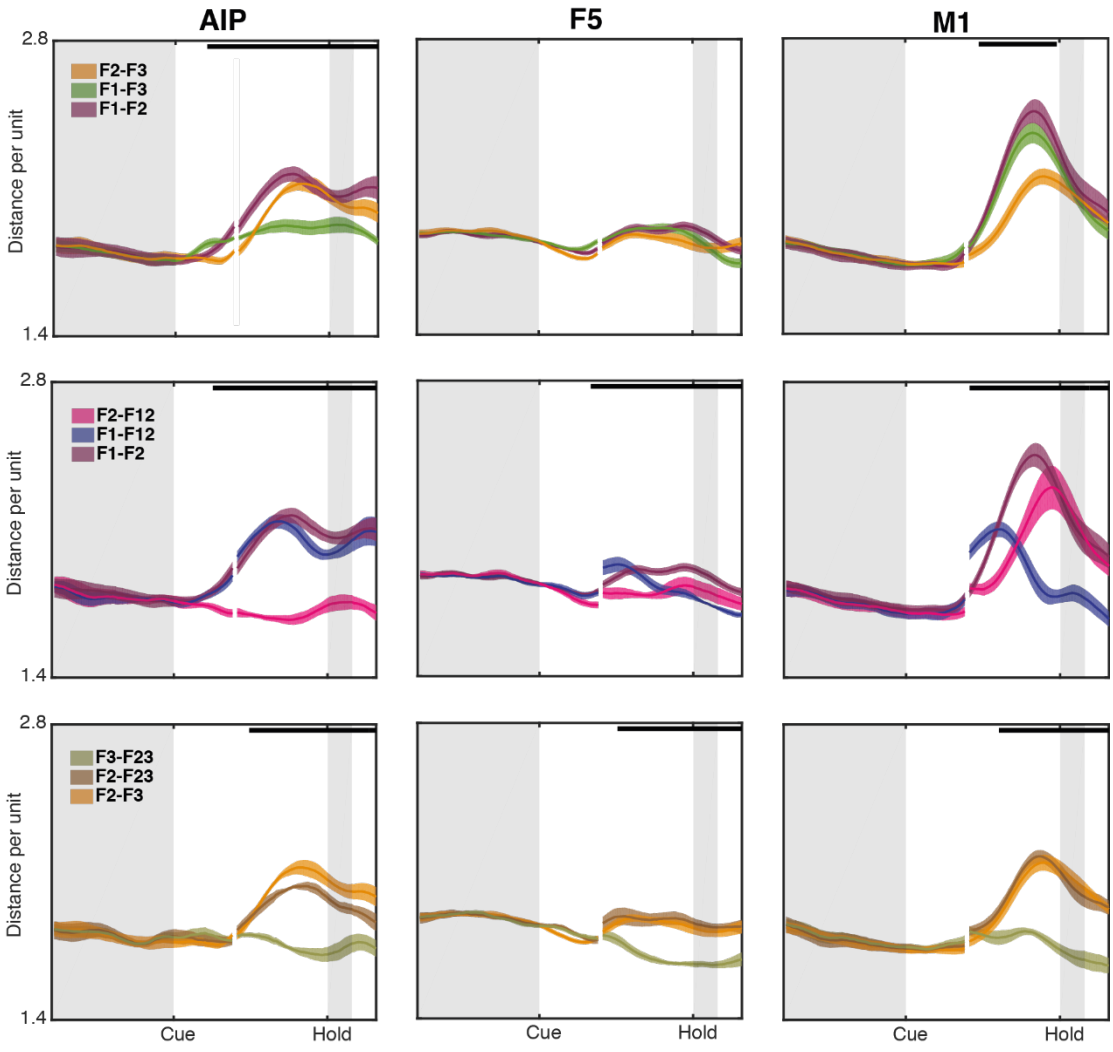

Figure 3.13 Distance analysis of selected condition pairs (average of six recording sessions)

Averaged results of the distance analysis. The S-S category (top row), and the two groups of the D-rS category (middle and bottom row) are the same as in Fig. 3.12. Shadows show standard error from the six recording sessions. Bars at the top show significant intervals derived from a cluster-based permutation test based on a 1-way-ANOVA ($p < 0.05$).

In addition to the full neuronal space, we repeated the distance analysis on the PCA and dPCA transformed data (condition-dependent components, Fig. 3.14). The results from the two dimensionality reduction techniques were very similar to the analysis from the full neuronal space (only the S-S category is shown). However, there were some minor differences. The baseline in Fig. 3.14 was more stable than in Fig. 3.13, probably because the dimensionality reduction was based on trial averaged data. The convergence of firing rates in the fixation epoch can be observed at the single-neuron level (Fig. 3.8), where the differences between conditions declined

with time. This was reflected in the single-trial based distance analysis in the full neuronal space, but not visible from the trial averaged analysis. Furthermore, in Fig. 3.14, the magnitudes of the normalized distances in area M1 were larger than the ones in area AIP, while in Fig. 3.13, the difference between these two areas was smaller. It is likely because the firing rates for the full neuronal space were square-root transformed, and the data for PCA and dPCA transformations were not. Another point to be mentioned is that in area AIP, the F1-F3 line seemed to be modulated by movement stronger in Fig. 3.14 than in Fig. 3.13. A possible explanation is that there were some portions of neurons not tuned for the F1-F3 condition pair, but the variance of these neurons were relatively small and might not be captured by the first few dimensions of the dimensionality reduction technique. Nevertheless, the results from the full neuronal space and the two dimensionality reduction techniques are very similar, and it is appropriate to use either one of them.

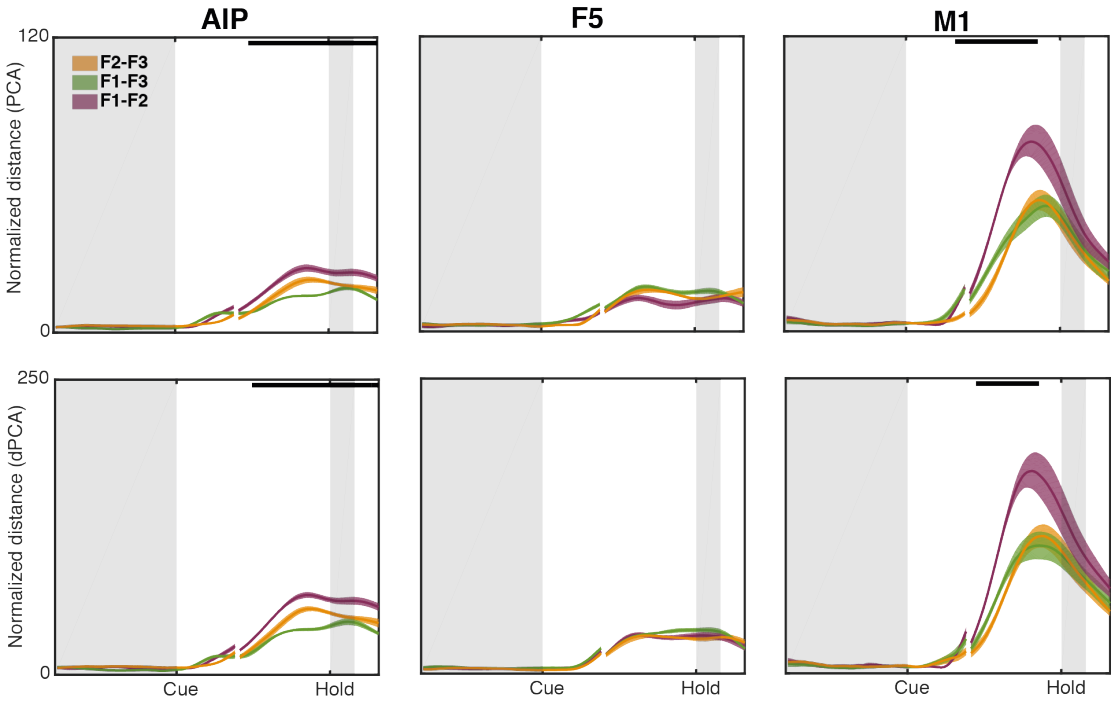

Figure 3.14 Distance analysis of PCA and dPCA transformed data (average of six recording sessions)

Distance analysis of PCA (top row) and dPCA (bottom row) transformed data of the S-S category (F1-F2, F1-F3 and F2-F3, legend in top row AIP subplot) in area AIP, F5 and M1. To perform distance analysis of the PCA transformed data, k PCs were used so that the cumulative variance was just exceeding 90% of the total variance (k is different for each area). Euclidean distance was normalized by the square root of k. Distance analysis of the dPCA transformed data was done by using the first five condition-dependent components (section 3.8). Trial alignment, mark of epoch onsets, shadows showing standard error and significant bars are the same as in Fig. 3.13.

In summary, Euclidean distance between two neural trajectories can be used to measure the similarity of the population firing rates of the experimentally designed conditions. As seen in the neural trajectories plotted in PCA space, the distances between the conditions increase during movement, and are largest in area M1, followed by area AIP. For the S-S category, the differences between the normalized distances were significant from the late cue epoch till the end of the trial in area AIP, while in area M1, only from the late cue epoch till shortly before the hold epoch. We therefore used the average value from the period of the late cue epoch till end of the hold epoch to make a summary plot (Fig. 3.11 B). The columns of this matrix are arranged by the four categories mentioned in section 3.5: S-S, D-rS (F12 and F23 groups),

D-nrS and D-D. Across the three areas, it is obvious that area M1 has the highest distance per unit and area F5 has the lowest. In area M1, the S-S category has the first two highest distances (F1-F2: 2.20, F1-F3: 2.13), followed by the D-nrS category (F1-F23: 2.08, F3-F12: 2.12). In area F5 and AIP, the ranking of D-nrS and D-rS is not that clear. The discrepancy mentioned previously between area AIP and M1 can be easily observed from the colormap. It was between F1-F3 and F2-F3 for the S-S category and between F1-F12 and F2-F12 for the D-nrS category.

3.10 Reconstruction of double movements from corresponding single movements

In addition to assessing the similarity between conditions in the neuronal state-space with the Euclidean distance, we would like to know whether a double movement neural trajectory is a linear combination of its two corresponding single movements. This question is important under two different perspectives. First, knowing the complexity of the multitendoned muscles controlling the individual fingers, it is interesting to see how the brain encodes this control signal. Second, if a combined finger movement is a linear combination of the two corresponding single movements, it will be possible to train a BMI decoder only based on single movements. This is an important "generalization" for decoding applications. Multiple linear regression could be used to test this hypothesis (section 2.14). If a linear combination of the two single movements could reconstruct the combined double movement better than the third single movement (in this study, there were only three single movements), the double movement could be seen as a combination of the two single movements in the neuronal state-space, instead of an independent movement type. In contrast, if the goodness of fit for the reconstructed double movement and the reconstructed third single movement was found to be at a similar level, the double movement was considered as an independent movement type. In this study, there were two double movements, F12 and F23. To test the hypothesis, we used F1 and F2 to predict F12 (F1+F2 -> F12), and F2 and F3 to predict F23 (F2+F3 -> F23). For the F12 and the F23 group, the corresponding controls were F1+F2->F3 and F2+F3->F1. For a general description of predicting a double movement with two single movements, the linear regression could be stated as:

$$X_{12} = X_1\beta_1 + X_2\beta_2 + \beta_0 + \epsilon$$

where X_{12} denotes the double movement, and X_1, X_2 denote the two single movements. β_1 and β_2 are the corresponding regression coefficients. β_0 is the constant and ϵ is the error term.

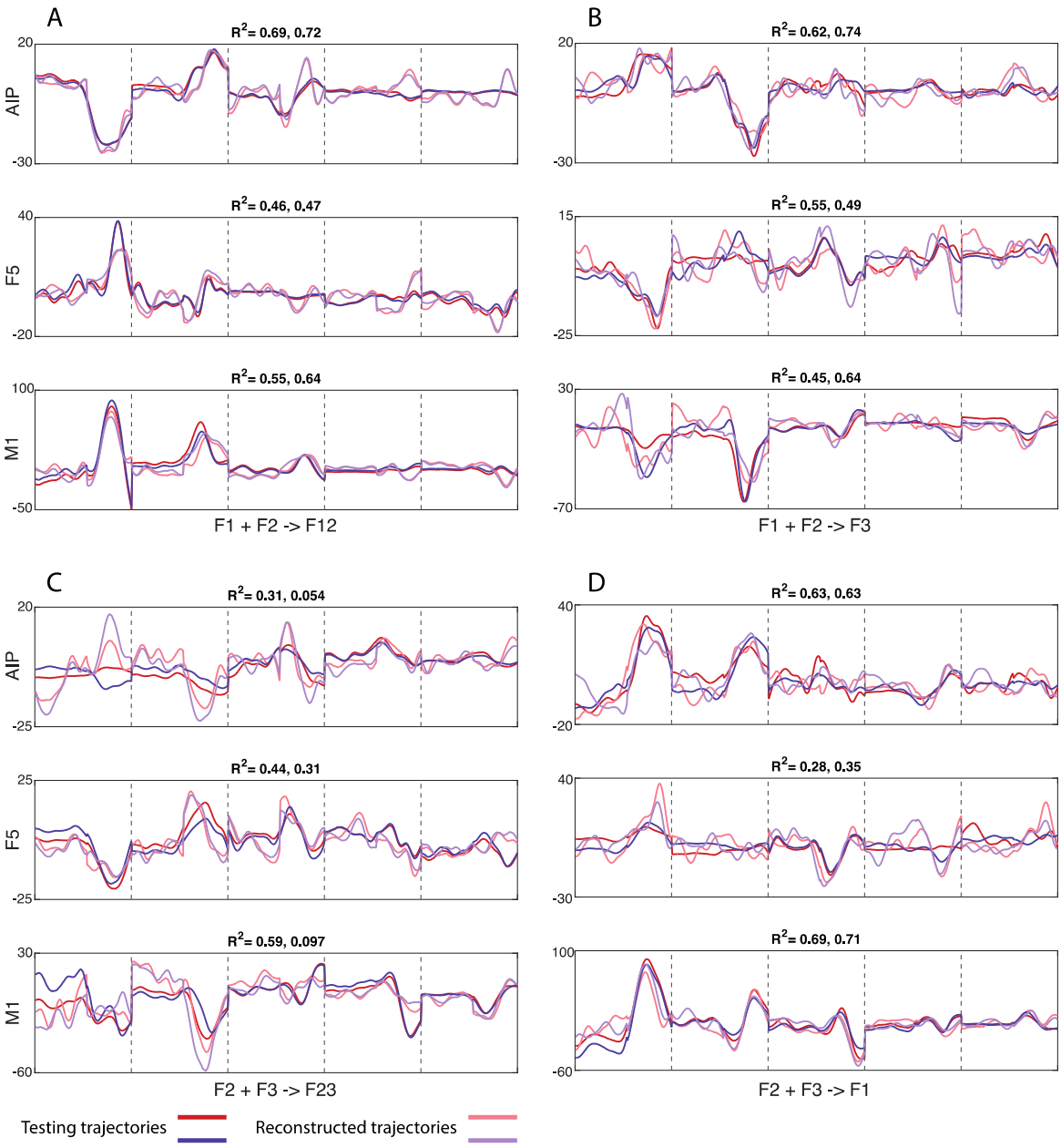

Figure 3.15 Example of two testing and two reconstructed trajectories from the cross validation

Testing and reconstructed trajectories from two iterations of the cross validation procedure (Rec9, dPCA results). The testing trajectories were plotted in darker colors (1st: red, 2nd: purple) and the reconstructed trajectories in lighter colors (1st: pink, 2nd: light purple, legend at the bottom). The reconstruction of the five dPCs (normalized firing rate change over time) were performed separately and then concatenated to calculate the correlation coefficient (the corresponding R^2 value for the 1st and the 2nd iteration on top of each subplot). The borders between the dPCs were marked by the dotted lines. The regressions were performed with the entire trial (trial alignment: shown up to 250 ms after cue onset and shown from 350 ms before hold onset) and separately in area AIP, F5 and M1 (top, middle and bottom subplots). (A) F1+F2->F12. (B) F1+F2->F3. (C) F2+F3->F23. (D) F2+F3->F1.

From the dPCA results (section 3.8), we know that there is a large portion of total variance explained by the condition-independent components. Thus, using the

condition-dependent part of the population firing pattern to perform multiple linear regression can give us a clearer view about the linear relationships between the different movements. We performed the multiple linear regression with both principal components (PCs) and the condition-dependent demixed principal components (dPCs), so we can compare the goodness of fit with and without the common components.

Because of the smoothing of the neural trajectories, leave-one-time-point-out cross validation can not avoid overfitting to a desired level (data not shown). We thus applied a 2-fold cross validation based on splitting the trials of the response variable conditions (X_{12}) into training set and testing set. This procedure was repeated k times, so that every possible combination of training and testing set was used. In each iteration, β values were obtained by regressing the training trajectory (average of all trials in the training set) on the predictor variables (X_1 and X_2) and the correlation coefficient was calculated between the reconstructed trajectory (multiplication of β values with predictor variables) and the testing trajectory (average of all trials in the testing set) to avoid overfitting. Fig. 3.15 shows two example reconstructed trajectories (pink and light purple) and two corresponding testing trajectories (red and purple) from two iterations of the cross validation procedure. One R^2 value was calculated in each iteration, and the whole cross validation process produced a distribution of R^2 values (Fig. 3.16). The near-normal distributions indicates that the 2-fold cross validation based on splitting the trials into half is appropriate. Averaged R^2 values from one recording session were used as a measurement for goodness of fit and test the differences among groups using all six recording sessions (Fig. 3.17).

In addition to the hypothesis mentioned (the two types of response variable, double vs. third single movement), there are two other factors we can test statistically, differences among areas (AIP, F5 and M1) and the two groups of predictor variables (F1 + F2 and F2 + F3). We first performed a 3-way ANOVA to test the influence of these three factors on R^2 values of the dPCA data. All three factors were significant (3-way ANOVA, $p<0.01$). However, for the predictor variable group and the response variable type, p values were between 0.005 and 0.01 (R value). We tested further

the predictor variable group and the response variable type with 2-way ANOVA in area AIP, F5 and M1 separately. Only in area AIP, predicting F23 with F2 + F3 was significantly worse than the other three conditions (2-way ANOVA and post-hoc Tukey-Kramer criterion, $p<0.01$, Fig. 3.17 A first row).

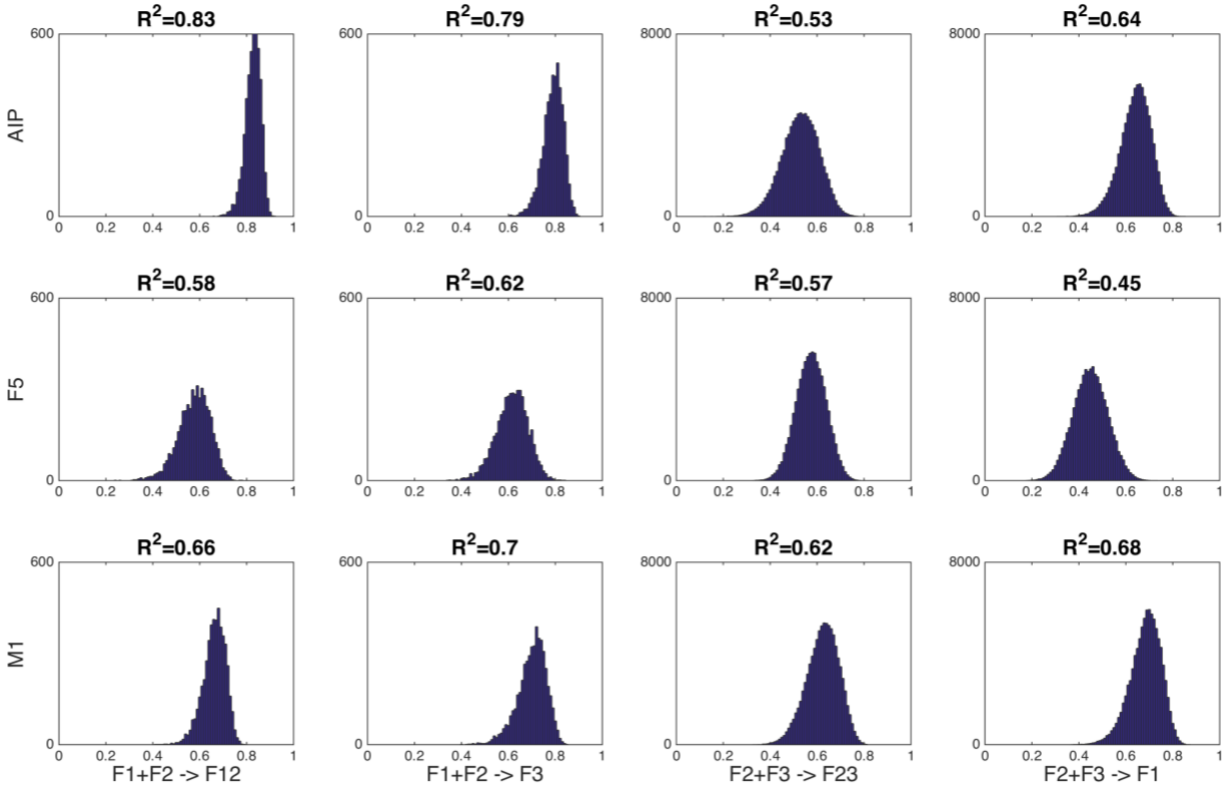

Figure 3.16 R^2 histograms of the cross validation process from one example recording session

Histograms of R^2 show the correlation coefficients between the reconstructed trajectories and the testing trajectories of one example recording session (Rec5, dPCA results). There are two groups of regressions, F1+F2->F12 (first column) and F2+F3->F23 (third column). For each group, there is a control using the two single movements to predict the third unrelated single movement (F1+F2->F3 for F12 group, second column, and F2+F3->F1 for F23 group, fourth column). In each group, the number of iteration for the cross-validation procedure was based on the number of trials of the double movement. The regression was performed separately for area AIP, F5 and M1 (first, second and third row), and resulted in 12 conditions shown as subplots in this figure. The mean of the R^2 values is shown on top of each subplot.

We repeated the analysis with PCs and the differences between response variable types and across areas were significant (3-way ANOVA, $p<0.01$). We tested each area separately with 2-way ANOVA, and only in area F5, predicting F12 with F1 + F2 was significantly better than predicting F3 (2-way ANOVA and post-hoc Tukey-Kramer criterion, $p<0.01$, Fig. 3.17 B). The R^2 values from PCs were significantly higher than

R^2 values from dPCs in area F5 and M1 (1-way-ANOVA, $p<0.01$), but not in area AIP (Fig. 3.17).

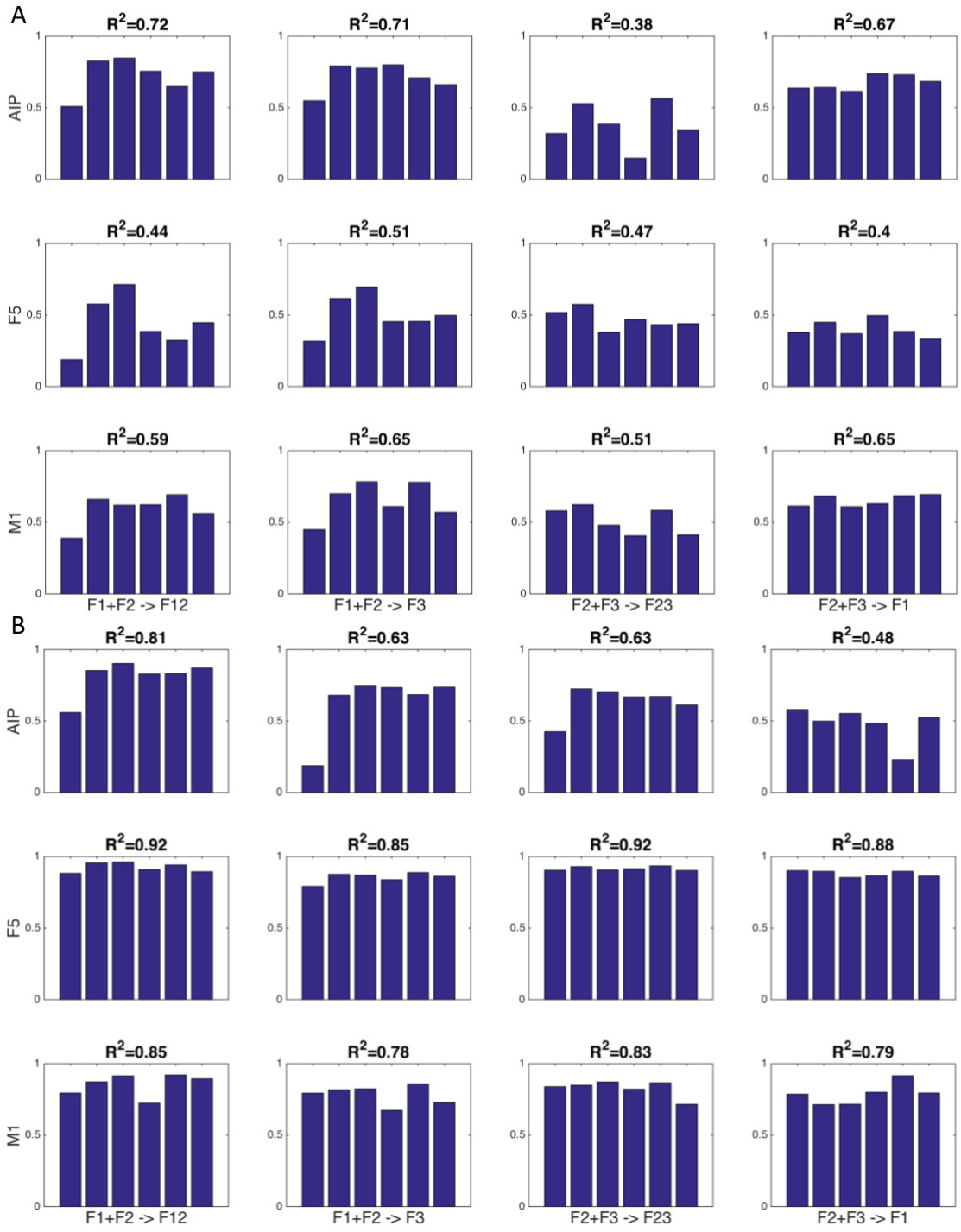

Figure 3.17 R^2 values from six recording sessions

Columns show different regression groups and rows show different areas (same as in Fig. 3.14). In each subplot, bars show R^2 values from six recording sessions and averaged value across sessions are shown on top. A) dPCA results and B) PCA results.

Apart from comparing the correlation coefficients, we can also look at the β values from the regression groups. These values represent the weights of the two predictor variables (single movements). Since the β value can be negative, we use absolute value of β to compare the weights of the two predictor variables (Fig. 3.18). In detail, each predictor or response variable consists of five latent variables (e.g. five PCs or dPCs):

$$X_1 = \sum_{k=1}^{5} X_{1,k}\,;\; X_2 = \sum_{k=1}^{5} X_{2,k}\,;\; X_{12} = \sum_{k=1}^{5} X_{12,k}$$

where $X_{1,k}$, $X_{2,k}$, and $X_{12,k}$ are the k^{th} latent variable of the predictor and the response variables, respectively. The k^{th} latent variable of the response variable is then predicted by the k^{th} latent variables of the two response variables:

$$X_{12,k} = \sum_{k=1}^{5} X_{1,k}\beta_{1,k} + \sum_{k=1}^{5} X_{2,k}\beta_{2,k} + \beta_{0,k} + \epsilon_k$$

where $\beta_{1,k}$, $\beta_{2,k}$, $\beta_{0,k}$ and ϵ_k are the corresponding regression coefficients and the error term of predicting the k^{th} response latent variable.

We used five latent variables, so there are in total 15 β values for one regression. In Fig. 3.18, we plotted X_2 β values ($\beta_{2,k}$) against the X_1 β values ($\beta_{1,k}$) in scatter plots to compare the weights (for Fig. 3.18, we describe one dot as β_k, as abbreviation of $\beta_{2,k}$ plotted against $\beta_{1,k}$). We could then compare the weights of the two predictor variables with the Euclidean distance results. If the Euclidean distance between X_{12} and X_1 was smaller, the weights of X_1 β values were higher. The trend for the F1 + F2 predictor variable group was not clear. In M1, the distance between F1-F12 was smaller than between F2-F12, but only β_1 and β_5 were slightly below the orthogonal line and the other three β values were above, showing higher weights on F2. In AIP, the F12 trajectory was closer to F2, but β_1, β_3 and β_4 had higher weights on F1. For the F2 + F3 predictor variable group, the results matched our prediction. In all three areas, predicting F23 or F1 all had higher weights on F3, which is congruent with the distance analysis having smaller distance between F23-F3 and F1-F3.

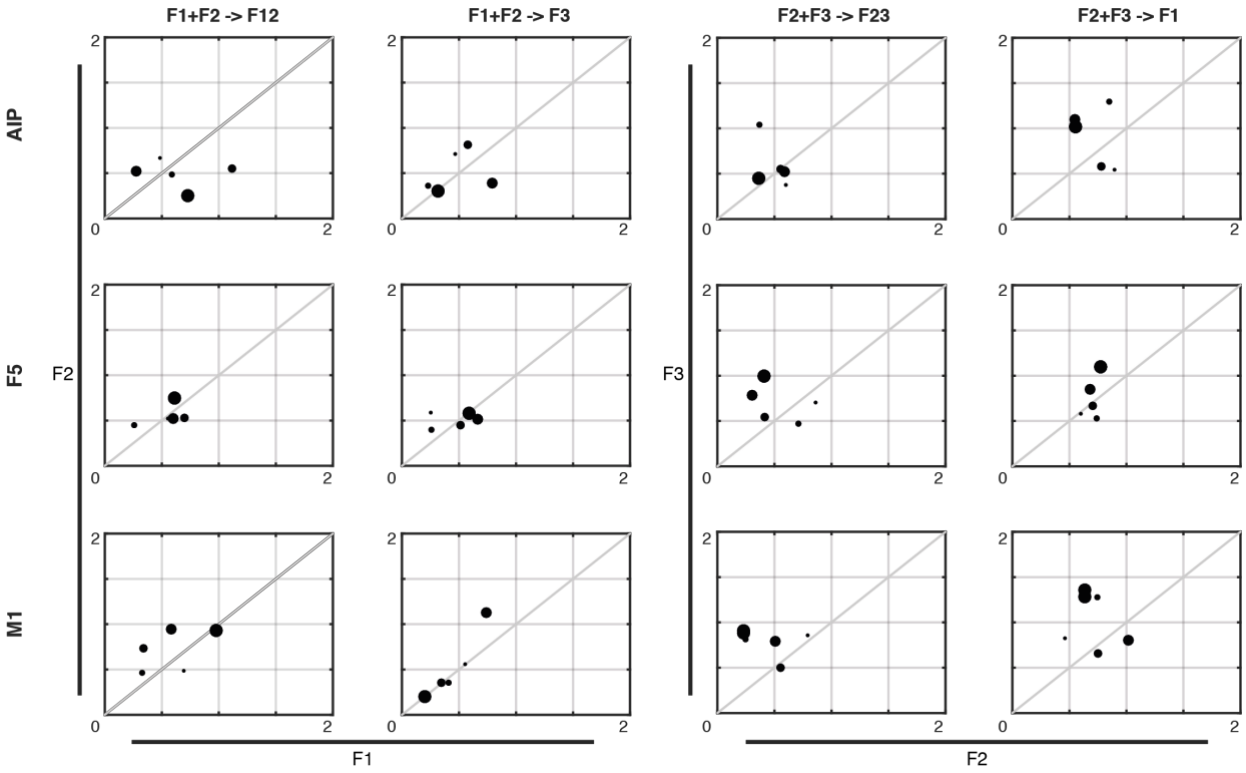

Figure 3.18 Weights of the two predictor variables

β values of predictor variable X_2 (y axis) plotted against β values of predictor variable X_1 (x axis). Subplots show averaged results from six recording sessions. The regression terms are shown on top of each column and subplots in each row show results from area AIP, F5 and M1 (same as in Fig. 3.16). There are two predictor groups, F1 + F2 and F2 + F3, marked by the thick lines at the bottom and the left of the subplots. In each predictor variable group, subplots in the first column show the β values predicting the double movement, and subplots in the second column show the ones predicting the third single movement as control. The five latent variables of the response variable were predicted separately, resulting in five β values for each of the two predictor variables and are shown as five dots in each of the subplot (the descending size represents the order of the latent variable).

In conclusion, both double movements (F12 and F23) should be considered as independent movement types, instead of combinations of the two related single movements, since the two single movements can not predict the double movement better than the third unrelated single movement. Nevertheless, when looking at the correlation coefficients, even the results with dPCs are not low (R^2>0.38 for all regressions in three areas). One could thus say that the trajectories of finger movements are linearly related. In additions, the β values represent the weights of the two predictor variables and for the F2 + F3 predictor variable group, this is congruent with the distance analysis results.

3.11 Online and offline decoding

In order to estimate to what extent can the experimentally designed task parameters be read out from the neural signal, as well as to investigate the potential application for controlling hand prosthesis in real-time, we performed both online and offline decoding with a Naïve Bayes classifier.

Online (real-time) decoding was performed with online (real-time) spike-sorting. The online spike-sorted data was later decoded offline for comparison. Neural data was offline spike-sorted (section 2.5) to better approach the full classification capacity. For online decoding, the performance for fixation epoch was 21%, cue epoch 52%, go epoch 66% and hold epoch 80% (averaged over all decoding runs). Among the five single and combined finger movements, F1 could be best decoded (86%), followed by F3 (85%) and F2 (78%), while decoding of F23 performed least (72%). The two confusion matrices in Fig. 3.19 A show the performance for the five conditions during the go and hold epoch of an example real-time decoding run (real-time spike sorting and online decoding, RTS-RTD). The diagonal elements (real condition = predicted condition) show the decoding performance and the off-diagonal elements (real condition ≠ predicted condition) show to which condition was the real condition wrongly predicted. For example, during the go epoch, in 14% of the trials, F1 was predicted as F3, and F2 was predicted as F12 (37.5%) or F3 (12.5%). During the hold epoch, the pattern changed slightly. Instead of predicted as F12, F2 was predicted as F23 (25%), and decoding of F1 achieved 100%. In short, confusions occurred mostly among double movements with its related single movements or vice versa, except for the thumb.

We then compared the decoding performance from different areas (All, M1, F5 and AIP), different decoding protocols and different epochs (Fig. 3.19 B). For online decoding (RTS-RTD), the all areas combined (abbreviated as “All area”) had the best performance, followed by M1, F5 and AIP was worst in both epochs (the difference between All and M1 was not significant, 1-way ANOVA and post-hoc Tukey-Kramer criterion, $p<0.01$). We reran the decoding offline with an 8-fold cross validation procedure (RTS-OffD). Compared to online decoding, there was an increase in

performance, but mostly not significant (each epoch and each area tested separately with 1-way ANOVA, $p>0.01$). Only in area AIP, during go epoch, RTS-OffD was significantly better than RTS-RTD (1-way ANOVA, $p<0.01$). Comparing among the areas of the RTS-OffD protocol, All and M1 were significantly better than AIP, but F5 was not significantly worse than M1 in both go and hold epoch (1-way ANOVA and post-hoc Tukey-Kramer criterion, $p<0.01$). In order to approach the full classification capacity, we manually sorted the spikes and performed the same offline decoding (OffS-OffD). In both go and hold epoch, the performance increased for all the areas. Especially for AIP, its performance exceeded F5 in both epochs. Comparing with RTS-OffD, only AIP was significantly better during both epochs (1-way ANOVA, $p<0.01$), while comparing with RTS-RTD, differences during go epoch in ALL and M1 were also significant (1-way ANOVA, $p<0.01$). Comparing among the areas of the OffS-OffD protocol, F5 was significantly worse than All and M1 in go epoch, and both F5 and AIP were significantly worse than All in hold epoch (1-way ANOVA and post-hoc Tukey-Kramer criterion, $p<0.01$). To visualize the decoding capacity gained by the manually sorted data for each area, we plotted the RTS-OffD against the OffS-OffD performance (Fig. 3.19 C). The AIP data points are at the upper left of the scatter plot, and the farthest from the diagonal line. This means comparing to other areas, the manually sorted-data from AIP contained more information, which was not revealed by the real-time spike sorting.

Figure 3.19 Online and offline decoding (opposite page)

A) Confusion matrices show classification performance for the five conditions of an example run (decoding from all areas). Left: go epoch, right: hold epoch. B) Averaged performance for different decoding protocols. There were eight online decoding (RTD) and five selected offline decoding (OffD) sessions during go epoch (left) and hold epoch (right). Online decoding was performed with real-time spike-sorting (RTS-RTD, blue) and later compared with eight-fold cross-validated offline decoding results (RTS-OffS, orange). Offline spike-sorting was used for offline decoding (OffS-OffD, yellow) to better approach the full classification capacity of the data. Error bars show standard deviation and dotted lines show chance level (20%). C) Scatter plots of RTS-OffD versus OffS-OffD performance. Five individual sessions (based on offline decoding sessions) were plotted separately by using data from area AIP, F5, M1 and combination of all areas (All).

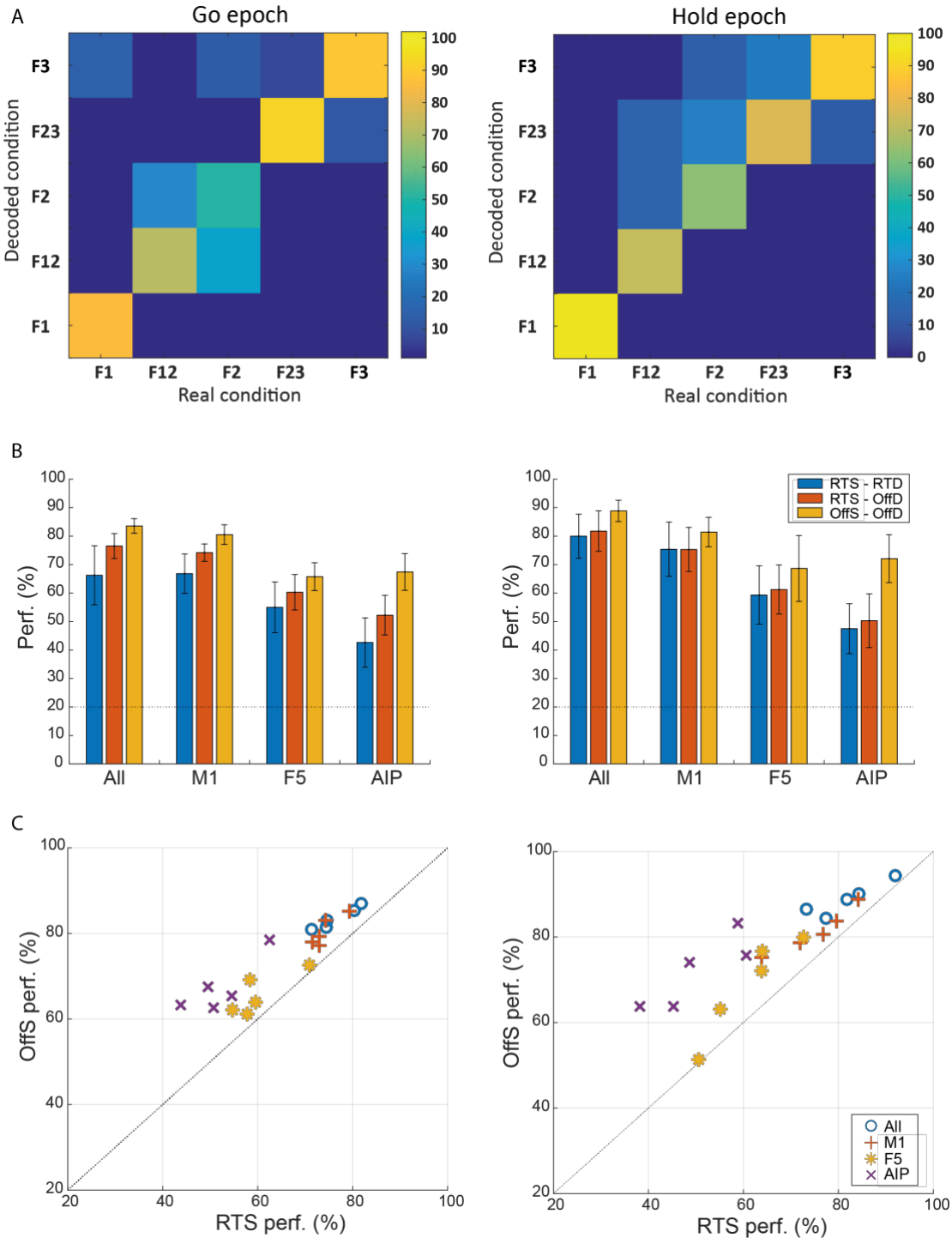

In conclusion, individual and combined finger movements can be decoded with a Naïve Bayes classifier. During the hold epoch, the real-time decoding performance was 80% and with offline manual spike sorting, the performance reached 89%. For the decoding with online spike-sorted data (RTS-RTD and RTS-OffD), in accordance with previous studies, the All area had the best performance, followed by M1, F5

and AIP in decreasing order (Schaffelhofer et al., 2015, Menz et al., 2015). However, manual spike sorting strongly improved the performance of area AIP (up to 25% during hold epoch). In addition to area M1, the decoding results show potential benefits of using area F5 and AIP for future brain-machine interface controlling dexterous finger movements.

4. Discussions

4.1 Summary

The goal of this study was to investigate how individuated finger movements are coded in area AIP, F5 and M1. At the single neuron level, most of the units in all three areas were “broadly tuned”, responding during multiple movements with different firing rate amplitudes. However, the specific tuning dynamics of these three areas were distinct. After the cue onset, the percentage of tuned AIP units was significantly higher than in the other two areas, while before the beginning of hold epoch the percentage of tuned M1 units significantly exceeded that of area AIP and F5. This trend was well in line with the partial correlation coefficient (pcc) between error trials and corresponding correct trials, an analysis capable of disentangling the encoding of visual and movement components. In area AIP, “cue error pcc” was higher than “movement error pcc” from cue onset till end of the hold epoch, while in area M1, “cue error pcc” was also higher than “movement error pcc” after cue onset, but “movement error pcc” exceeded “cue error pcc” shortly before the hold epoch. As a transition between AIP and M1, in area F5, the difference between “cue error pcc” and “movement error pcc” was smaller than in area AIP and the “movement error pcc” reached its maximum during the hold epoch, where the two pcc values were not significantly different. These results showed the more visual-dominant property of AIP and the more movement-dominant property of M1.

Due to the temporal complexity and heterogeneity at the single-neuron level, it was necessary to see all the units as a population. Under this perspective, each recorded unit was considered as one dimension in a state-space, and the population firing rates involving over time form a neural trajectory through this space. Plotting the first three principal components yielded a low-dimensional trajectory that can be visualized and that still represented >75% of the total variance of the original data. In area AIP and M1, the trajectories of the five conditions were quite divergent. F1 and F2 trajectories were far apart from each other and F3 trajectory was in between. F1 + F2 was closer to F2 and F2 + F3 was closer to F3, showing that the population firing rates of the double movements resembled one of the two single movements more

than the other. The differences between conditions were further quantified by the Euclidean distance between the neural trajectories. In accordance with the observation in the PCA space, the distance between F1 and F2 was the largest and the distance between F3 and F2 + F3 was the smallest. There were also discrepancies across the areas. In AIP, between the three single finger movements, the distance between F1 and F3 was the smallest, while in F5 and M1, the smallest distance was between F2 and F3. Comparing distance between F1 + F2 and its two corresponding single movements F1 and F2, the distance between F1 + F2 and F2 was smaller in AIP, but the distance between F1 + F2 and F1 was smaller in M1.

In order to separate the condition-dependent variance and the time-dependent (condition-independent) variance, we applied demixed principal component analysis (dPCA). In all three areas, the five conditions were well separated when projecting the neural data onto the decoder axes of the first two condition-dependent dPCs. However, the proportion of variance explained by the condition-dependent components in area F5 were distinct from area AIP and M1. In area AIP and M1, the proportion was about 50%, but it was 20% in area F5.

Based on the condition-dependent components separated by dPCA, we further tested the relationship between a double movement and its two corresponding single movements. If a linear combination of the two single movements can reconstruct the combined double movement better than the third single movements, the double movement can be seen as a combination of the two single movements in the neuronal state-space, instead of an independent movement type. In fact, the goodness of fit for reconstructions of the double movements was not significantly different from the goodness of fit for reconstructions of the third single movement, suggesting that both double movements should be considered as independent movement types.

We performed online decoding to investigate the potential application for a hand prosthesis capable of moving fingers independently, since most of the state-of-art prostheses only have one DOF opening and closing the hand. Using neural signal from all three areas, the real-time decoding performance during the hold epoch was 80%, and with offline manual spike sorting, the performance reached 89%. In

addition to M1, we also demonstrated the potential benefits of using area F5 and AIP for prosthesis control.

4.2 Task design and control of kinematics

The delayed finger flexion task in this study has some unique aspects compared to previous individuated finger movement tasks (Schieber, 1991; Poliakov and Schieber, 1999; Baker et al., 2009; 2010). First of all, our task paradigm had a fixation epoch (500ms) and a longer cue epoch (500ms), whereas in the previous tasks, there was no fixation epoch and the monkeys were allowed to move after the cue appeared. The idea of fixation and cue epochs were adapted from the delayed reach and grasp tasks (Murata et al., 1996; Raos et al., 2006; Churchland and Shenoy, 2007; Lehmann and Scherberger, 2013; Ames et al., 2014; Kaufman et al., 2014; Schaffelhofer and Scherberger, 2016), in which the preparatory activity could be distinguished from the movement activity. For a motor task allowing the animal to move immediately after the cue appears, the preparatory and the movement activity is compressed in a short period of time, i.e. within 100-300 ms. For example, in the study of functional grouping M1 neurons during individuated finger movements, average firing rate during the 100 ms before switch closure (comparable to the beginning of the hold epoch in reach and grasp task) was used for cluster analysis (Poliakov and Schieber, 1999). Although our task paradigm did not have a memory epoch and the length of the cue epoch was fixed, so the animal was able to anticipate the go cue during the cue epoch, a transition from preparatory state to movement state was still visible. For example, the AIP unit in Fig. 3.3 had a smaller peak after cue onset and a second peak at the beginning of the hold epoch, similar to previous studies in which the monkeys performed different grip types indicated by abstract cues (Lehmann and Scherberger, 2013) or grasped objects with different shapes and sizes (Schaffelhofer and Scherberger, 2016). Comparing the tuning dynamics of the three areas in the neuronal population, the percentage of tuned units in AIP increased earlier than the other two areas (Fig. 3.4 B). In accordance with previous studies (Fluet et al., 2010; Lehmann and Scherberger, 2013), units in all three areas started to be tuned in a

gradual manner. The partial correlation analysis also showed the transition from preparatory state into movement state. In area M1, the peaks of the “cue error pcc” and the “movement error pcc” appeared sequentially, indicating a visuomotor transformation process happened during the trial.

Another important aspect of individuated finger movement tasks is the kinematics of the fingers. Ideally, one would like to measure the possible range of the whole extension and flexion of each digit. Due to the strong mechanical coupling between the fingers, it will be difficult to extend or flex one finger to the extreme extent while maintaining the others at the resting positions. In a human study quantifying the independence of finger movements, the distance between the MCP and the DIP joints was used to guide the individuated finger movements, and this corresponded to approximately a 35-degree movement for the index and the middle finger (Häger-Ross and Schieber, 2000). In monkeys, to achieve this range of movement is difficult, because of physiological constrains, as well as training issues. In a representative study quantifying the independence of macaque monkey digits, the estimated movement ranges for thumb, index and middle finger were 3.4 mm, 4.6 mm and 3.8 mm, respectively (Schieber, 1991). These ranges represent only a small fraction of the full physiological range of natural finger movements. However, the argumentation was that such small movements were chosen to approximate the finger movements used by monkeys in fine manipulations.

For understanding the control of finger movements, the question of how the brain controls a digit to flex and extend in the full physiological range and the question of how individuated finger movements are coded in the brain are actually slightly different ones. Practically, it is easier to design animal experiments to answer the second question and it may also be the necessary first step for prosthesis application. A following decoding study showed that the small movements mentioned in the previous paragraph can be decoded with >99% accuracy using signals recorded from M1 (Ben Hamed et al., 2007). This indicates that the small movement ranges are valid to answer how individuated finger movements are coded in the brain. On the other hand, due to the mechanical coupling of fingers from the multitendoned muscles, increasing the movement range might need activation of additional

muscles to prevent the simultaneous movement of non-instructed fingers. The neural signal recorded during such a movement might be more complex and difficult to distinguish between the encoding of activating the instructed finger and the encoding of preventing the movement of non-instructed fingers. The manipulandum used in this study has a movement range slightly smaller than the ranges mentioned in the previous study (Schieber, 1991) and this movement range was fixed for all three fingers. Nevertheless, it was sufficient to answer the question of individuated finger movement coding.

4.3 Diverse neural discharge patterns during individual finger movements

As mentioned in section 4.2, previous studies of individuated finger movements rarely focused on the temporal feature of the neuronal discharge. In the study from (Poliakov and Schieber, 1999), the reaction plus movement time (RM time) was limited within 700 ms (cue onset to switch closure). Histograms of three example neurons showed that firing rates increased immediately after cue onset, reaching their maxima approximately within half of the RM time (ca. 250 ms in these examples), and dropped back to baseline level shortly after switch closure. In another study from (Egan et al., 2012), the monkey was allowed 1000-2500 ms to perform the movement. The nine example neurons (one for each instructed movement only) had their maximal firing rate changes at the time of the switch closure. Observed from our M1 recorded units, there is indeed a diversity of temporal discharge patterns during individual and combined finger movements. Differences in temporal discharge patterns could be a change of firing rate during the same movement in different neurons (e.g. Rec5-074-03m and Rec5-084-01m in Fig. 3.8), or changes of firing rate between different movements in the same neuron (e.g. Rec9-076-01s in Fig. 3.3). These two differences of temporal discharge patterns were also observed in area AIP and F5 (Fig. 3.8).

In addition to temporal discharge pattern, the maximal amplitudes for different movements in the same neuron are also diverse. This was mentioned in the study from (Poliakov and Schieber, 1999), but not emphasized in the study from (Egan et

al., 2012), since their goal was to decode finger movements using receiver operating characteristic curves for majority-voting. In our data, we also observed the diverse amplitudes for different movements, and this was true for all three areas (Fig. 3.3 and Fig. 3.8).

To characterize the tuning of neurons with such temporal and amplitude diversity, we applied the cluster-based permutation test (Fig. 3.4). By testing all the units in each area, we were able to compare the percentage of tuned units across areas. However, from a more modern neuron-population perspective, each single neuron response is only a small piece of the entire network, and heterogeneity is expected at the single neuron level.

4.4 Assessing similarities among different individual finger movements

The cluster-based permutation test was precise at showing the timing of tuning. However, describing how a neuron encodes one movement different from another is a multiple comparison question and the conditions have to be compared in pairs. The resulting ten condition pairs from five conditions made it too complex to present the changes over time like in the permutation test. We thus used averaged firing rates in each epoch for multiple comparison among conditions (Fig. 3.5). To have an easier overview of the ten condition pairs, they were classified into four categories: single-single (S-S), double-related single (D-rS), double-unrelated single (D-nrS) and double-double (D-D). Our hypothesis was that the percentage of units firing differently for the S-S category will be the highest, and for the D-rS category will be the lowest. Since the brain might care more to distinguish between different single finger movements than between double movements and one of the related single movement. This was partially true in area F5 and M1, where the percentage of units firing differently for 1-2 and 1-3 condition pairs (S-S) were the highest, and in area AIP the percentage of units firing differently for 1-12 and 3-23 condition pairs (D-rS) were the lowest.

There were some drawbacks of using ANOVA and post-hoc Tukey-Kramer test for multiple comparison described above. First, the p-value threshold of the statistic test

was arbitrarily chosen and units containing task relevant information might be ignored. A neuron not firing “significantly different” between two conditions does not mean it fires the same for these two conditions. From a population perspective, this neuron could still contribute to coding difference between these two conditions. Second, using average firing rate in an epoch might average out some significant effects, since units in all three areas started to be tuned in a gradual manner (Fig. 3.4 A). However, with Bonferroni correction, it will be difficult to further divide epochs into smaller time intervals.

A possible way to avoid setting an arbitrary p-value threshold is to calculate Euclidean distance between two conditions. (Poliakov and Schieber, 1999) measured similarity between neuron pairs by Euclidean distance measured in a 12-dimensional space defined by the 12 experimentally designed individual finger movements. However, the attempt of classifying neurons into functional groups failed. This is probably due to the fact that, compared to center out reaching, the muscle activation pattern involved in individuated finger movements are more complex (see section 1.2), and only very small proportion of neurons were clearly tuned to one or two finger movements (likely the ones represented as examples in both studies mentioned).

With the development of population analysis, each simultaneously recorded neuron can be considered as one dimension in a state-space, the discharge pattern of all neurons is then a single trajectory in this space. This allowed us to compare between condition pairs based on all simultaneously recorded neurons instead of comparing condition pairs based on discharge pattern of each single-neuron. In the study of (Ames et al., 2014), the Euclidean distance was compared between a delayed-movement trajectory and a non-delayed movement trajectory in the neuronal high dimension space, and it was concluded that the preparatory state is not necessary for the generation of movements and can be bypassed. In our study, by choosing proper time alignment, it was possible to calculate the Euclidean distance between trajectories of two conditions for each time point (Fig. 3.12, 3.13 and 3.14).

Compared to the multiple comparison based on single neurons (we consider the results in the go and the hold epochs), the state-space Euclidean distance results

were more intuitive and easier to interpret. In the S-S category, the percentages of units tuned for the 1-2, 1-3 and 2-3 condition pairs were at a similar level in all three areas (Fig. 3.5), while the normalized distance F1-F2 was significantly larger than F1-F3 in area AIP and M1 (Fig. 3.13 top row). In the F12 D-rS category (condition pairs 1-12 and 2-12), the percentage of units tuned for the 2-12 condition pair in area AIP and F5 was lower than for the 1-12 condition pair (Fig. 3.5), and was congruent with the Euclidean distance results, where the normalized distance F2-F12 was significantly smaller than F1-F12 (Fig. 3.13 middle row). As mentioned in section 3.9, there was a discrepancy between area AIP and area M1, where the normalized distance F1-F3 and F2-F12 were smaller in AIP, but F2-F3 was smaller than F1-F3, and F1-F12 was smaller than F2-F12 in M1. At the single neuron level, this trend also existed, but for comparing 1-3 and 2-3, the result were not significant (Fig. 3.5). In the F23 D-rS category (condition pairs 2-23 and 3-23), there was no inconsistency among areas. The percentage of units tuned for 3-23 was lower than 2-23 and the normalized distance F3-F23 was smaller than F2-F23 (Fig. 3.13 bottom row). The discrepancy between area AIP and M1 may reflect the transition from AIP coding abstract cues related to movements to M1 coding preparation and initiation of movements. Judging from the distance analysis results, F5 resembled more M1 than AIP.

The Euclidean distance analysis also allowed us to characterize the temporal discharge patterns of different conditions at the population level. This analysis quantified the distance between the different trajectories in Fig. 3.9. Taking the F12 movement in M1 as an example, at the initial phase of the movement, the F12 trajectory was closer to F2, but after the movement started, it was closer to F1 (Fig. 3.9). This was precisely quantified by the distance analysis in Fig. 3.13 (the right subplot in the middle row). There was a cross between the F1-F12 (blue) and the F2-F12 (magenta) line ca. 150 ms before the hold epoch. In F5, a similar “compressed” version was observed, since the distances between trajectories of different conditions were relatively small, compared to the other two areas. This result could imply the behavior of the animal. During the F12 movement, he pressed first the index finger and latter the thumb, so the F12 trajectory was first closer to F2 and

later closer to F1. On the other hand, similar phenomenon does not exist for the F23 movement, where the F23 trajectory was always closer to F3. Knowing the thumb and the index finger being more independent than the middle finger (Schieber, 1991), it is easy to image that even after intensive training, flexing the thumb and the index finger simultaneously (condition F12) is more difficult than flexing the index and middle finger together.

Another question related to assessing similarities among individual finger movements is searching the relation between double movements and corresponding single movements. Known from the reach-to-grasp task (e.g. Michaels and Scherberger, 2018), there is a large common component with high percentage of variance explained in the spiking activity. This could very likely also be the case for individuated and combined finger movements. Using the supervised dimensionality reduction method demixed principal component analysis (dPCA), we could first discard the condition-independent components (time dependent components) and probe the relation mentioned with only the condition-dependent components. We addressed this question by reconstructing the trajectories of a double movement and a third non-related single movement using multiple linear regression. It turned out that the goodness of fit of these two reconstructions were not significantly different, indicating the two double movements in this study were independent movement types, not a combination of two single movements.

In addition to the two analyses mentioned in this section, the weights (β values) of the two predictor variables (the single movements) could also be used to asses the similarity between a double movement and the two corresponding single movements. In the F2 + F3 predictor variable group, the weights of F2 and F3 met our expectation. Both F1 and F23 trajectories were closer to F3, and the weights for F3 were higher (Fig. 3.18 third and forth columns). When predicting F3 with F1 + F2, the weights of the first dPC for F1 and F2 were at a similar level and the β_1 dots (F2 β plotted against F1 β) in all three areas lay on the orthogonal line (Fig. 3.18 second column). This could be explained by looking at first condition-dependent dPCs in Fig. 3.10. In area AIP and M1, the F3 lines (yellow) were weakly modulated by movement and the normalized firing rates were near zero, while the F1 (blue) and F2 (red) lines

appeared to be symmetric, having positive and negative peaks with similar magnitudes. The multiple linear regression was performed separately for data projecting onto each dPC axis, and each dPC component explained not more than 30% of the original data variance. Thus, one should interpret the β values with caution.

In summary, the similarities among individuated and combined finger movements could be assessed both at the single neuron and the population level. Compared to the previous attempts of classifying single neurons into functional groups of different movements (Poliakov and Schieber, 1999) or movement synergies (Kirsch et al., 2014), analyses at the population level are superior to analyses of single neurons. Considering each neuron as one dimension, trajectories representing different conditions in the high-dimensional space provide a simple and robust way of comparison among conditions. In addition, supervised dimensionality reduction techniques such as dPCA allow the separation of condition-dependent components and condition-independent components, and one can use the condition-dependent part for further analyses. As can be seen by plotting the first three PCs, F1 trajectory and F2 trajectory were the most distinct movements encoded in area AIP and M1, while F3 and the two double movements lay within the space surrounded by the F1 and F2 trajectories. This indicated the importance of the thumb and the index finger for hand use, e.g. we often use these two fingers to perform precision grip for grasping small objects.

4.5 The potential roles of area AIP, F5 and M1

Previous studies showed that area AIP and F5 both encode object information (Sakata et al., 1995; Murata et al., 1997; 2000; Raos et al., 2006) and potential motor plans (Rizzolatti et al., 1988; Baumann et al., 2009; Fluet et al., 2010; Schaffelhofer and Scherberger, 2016). AIP receives information from both dorsal and ventral visual streams and potentially shares this information with F5 via reciprocal connections (Luppino et al., 1999). Both areas contribute to extraction of object affordance and are crucial in sensorimotor transformation.

In our study, units in AIP responded faster and stronger than in F5 and M1 (Fig. 3.4 B), similar to a previous study where monkeys had to fixate and grasp 50 different objects (Schaffelhofer and Scherberger, 2016). However, when the movements to be performed were indicated by abstract cues, the story was a bit different. In studies where monkeys grasped a handle either with a precision grip or a power grip (Lehmann and Scherberger, 2013; Michaels and Scherberger, 2018), the percentage of units tuned to grip type started to increase earlier in F5 than in AIP and during the cue epoch, grip type coding was also stronger in F5 than in AIP. Since our study also used abstract cues to indicate different finger movements, it seems to be a little bit contradictory. However, when examining the movement kinematics in detail, the neural activity in area F5 seems to reflect the kinematic differences between the experimentally designed movements. Comparing tasks with only precision grip and power grip with tasks grasping different objects, the kinematic difference between the two grip types is likely larger than the kinematic difference of the hand shapes grasping two objects out of an object-pool. The percentage of F5 units tuned during the cue epoch represents the differences among experimental conditions. According to (Schaffelhofer and Scherberger, 2016), F5 does not encode stereotypical grip types, stated as “vocabularies of motor prototypes” (Rizzolatti and Luppino, 2001), but a continuum of hand configurations, similar to M1. Considering the kinematics of individuated finger movement in our study, due to the small movement range of few millimeters, differences between different finger movements resembled more the object-grasping task than the two-grip-type task. Therefore the response of F5 units was slower and weaker than AIP units.

In the study of (Michaels and Scherberger, 2018), AIP and F5 tuning pattern for orientations (grasping a handle in different orientations), was different from the pattern for grip types. AIP units were tuned to orientation faster and stronger than F5 units. It is clear that orientation is a more visual-related task parameter than grip type indicated by abstract cues, and thus AIP units responded faster and stronger. To further elucidate the role of AIP and F5 in visuomotor transformation, (Schaffelhofer and Scherberger, 2016) designed a set of objects which looked different but were grasped with similar hand shapes (abstract objects). Compared to a set of objects,

which looked different and also were grasped differently (mixed objects), the percentage of tuned AIP units during object presentation of these two sets was almost identical, but units in F5 and M1 rarely responded during presentation of the abstract objects. This result strongly characterizes the affordance extraction property of area AIP.

Similar to the design of the abstract objects, we could dissociate the visual component from the movement component encoded in area AIP, F5 and M1 by looking at the partial correlation between error trials and two types of corresponding correct trials ("cue error pcc" and "movement error pcc"). Although it is not really possible to compare percentage of tuned units with partial correlation coefficient, one could imagine that the scenario of "movement error pcc" is indeed comparing trials with different visual stimuli but the same movement. If there are more units firing differently (being tuned), the partial correlation between the two conditions will be smaller (less related) and vice versa. In the abstract-object task, the percentage of tuned AIP units was higher than the percentage of tuned F5 and M1 units from the onset of cue epoch till end of the hold epoch (Schaffelhofer and Scherberger, 2016), which correlates to a low pcc value in area AIP during the trial and a peak at the beginning of the hold epoch in area M1 in our study (Fig. 3.7 blue lines). The high percentage of tuned AIP units maintained during the planning and the movement epoch was hypothesized to serve as working memory (Murata et al., 1997; Borra et al., 2017). In our error trial partial correlation results, this phenomenon could be observed by comparing the "cue error pcc" (correlation between trials with the same visual stimulus but performed different movements) with the "movement error pcc" in area AIP. The "cue error pcc" increased fast after cue onset and maintained at a high level till the end of the hold epoch, whereas the "movement error pcc" was at the baseline level and increased slightly before the beginning of the hold epoch (Fig. 3.7). This implied that neurons in this area coded more about "what was seen" than "what was performed".

On the other hand, we were able to observe a pattern in M1, which was not possible with the abstract-object task. Ideally, one would like to have a complementary task, where monkeys receive the same visual stimulus but had different actions (e.g. a

free-choice task for precision and power grip). However, this might be difficult if one aimed to have more than two movements. In our study, we had maximum five different movements after a same visual stimulus (four different error trial types and the correct trial type, Table 3.2). The "internal state" of these error trials could be different from a decision-making process (Freedman and Assad, 2016). Nevertheless, the dissociation of visual stimuli and movements from the error trials revealed different patterns in area AIP, F5 and M1. As mentioned in section 1.4, M1 might contain information more complex than driving muscle activity. Evidence was found in M1 where "cue error pcc" also increased after cue onset and dropped to baseline level during the hold epoch, while the "movement error pcc" increased later and reached its maximum at the beginning of the hold epoch (Fig. 3.7). This indicates that there was information related to the abstract cues coded in M1, otherwise the population response would be similar to the pattern in the abstract-object task, where M1 did not distinguish between the objects that look differently but are grasped identically (Schaffelhofer and Scherberger, 2016). In other words, M1 did not care about different objects that are grasped in a same way, but responded to abstract cues indicating different movements even when the indicated movements was later not performed. Although we could not know why during these selected error trials the animal did not performed the cued movements (e.g. due to attention, or mechanical constrains of the hand etc.), the "cue error pcc" pattern was a clear indication that during these trials, the animal did response to the cues and did not perform the wrong movements by chance.

Well in line with our knowledge of sensorimotor transformation, the partial correlation pattern in area F5 appeared to be a transition between AIP and M1 by having a "cue error pcc" peak with smaller magnitude compared to AIP and a "movement error pcc" peak at the beginning of the hold epoch (Fig. 3.7). Indeed, there was a diversity of F5 partial correlation patterns from different categories of error trials, and some of them had a stronger "movement error pcc" pattern similar to M1 (Fig. 3.6).

As a last point of elucidating the potential roles of area AIP, F5 and M1, I would like to compare the proportion of variance explained by condition-dependent

parameters obtained from dPCA in these three areas. Compared to delayed grasping tasks (Intveld et al., 2018; Michaels and Scherberger, 2018), the proportion of variance explained by condition-dependent components in our finger movement task was at a similar level in area F5, but much higher in area AIP and M1. However, in both types of task, the percentages of units tuned to grip types or finger movements during cue and movement epochs were similar. This implied that in area AIP and M1, the proportion of units firing differently between conditions was similar in these two types of task, but a larger proportion of firing rate variance in the grasping task was not related to experimental conditions. For area M1, this could be explained by the stereotypical reach component in the grasping task. In every trial, the instructed hand left a hand rest bottom and reached for a handle in front of the animal. In contrast, in the finger movement task, the arm of the instructed hand was restricted in a tube and only minimum movements of the wrist and the palm were allowed during finger flexion. Therefore, the kinematic variance in the finger movement task was larger than in grasping tasks with common reaching component. In area AIP, the higher variance explained by the condition-dependent components could be due to the higher number of movements in the finger movement task, which corresponded also to a more complex abstract cue structure (both finger movement task and grasping task only use positions as cues). The strong separation between the conditions lasting to the end of the trial in the first condition-dependent component could be potentially coding for working memory in area AIP (Fig. 3.10 C).

Interestingly, the large-small-large pattern of the variance explained by the condition-dependent components in the AIP-F5-M1 circuit resembles the information bottleneck in the visual system. There are about 900 times more photoreceptors than ganglion cells (e.g. in the cat visual system), and thus the number of optic nerves sending the information to the brain (Pettigrew et al., 1986). The concept of information bottleneck has been used later to describe how attention plays a role for selecting relevant information out of the large amount of sensory inputs (Öğmen et al., 2013). We hypothesize that there is such an information bottleneck between area AIP and F5 responsible for selecting a motor

plan out of the “continuum of hand configurations” in F5 mentioned earlier in this section.

4.6 Decoding the dexterous finger movements

The most representative study of decoding individuated and combined finger movement is the work from (Ben Hamed et al., 2007). In this study, they used single electrodes to record neural activity while the monkeys performed flexion and extension of finger and wrist movements (12 in total) and six combined finger movements (flexion and extension of thumb, index, ring and little finger combined with one of the adjacent fingers). Based on spike counts 100 ms preceding the end of the movement (switch closure of the manipulandum), the two-layer nonlinear softmax (SM) estimator achieved 99.6% accuracy using as few as 30 neurons to decode the single movements.

SM estimator was a modification of logistic regression (LR) by dividing each output unit (five in total, for five fingers and the wrist) into a triplet. Each triplet encoded probability distributions of the corresponding digit or wrist to be in a flexion, extension or non-movement state. The purpose of this modification was to predict the combined movements base on a decoder trained with only single-movement neural activity. This attempt failed (performance of 38% for the six combined movements with the LR estimator), and the researchers gave two explanations. First, the population activity patterns of different single-movements were overlapping. From our population analysis results, we know this is indeed not the case. Even with basic covariance dimensionality reduction methods like PCA, which contains no *a priori* information of the task dependent variables, the trajectories representing different conditions diverged in the PCA space (Fig. 3.9). What the researchers observed as “overlapping patterns” was probably the “broadly tuned units” that they described earlier with the same data set, which could not be functionally grouped according to single neuron discharge patterns (Poliakov and Schieber, 1999). Second, the neural activity patterns of the combined movements were unlikely to be simple linear combinations of the two corresponding single movement patterns. This

is in accordance with our multiple linear regression results, but stated in a slightly different way. Since the goodness of fit for reconstructing a combined movement is not better than reconstructing a third non-related single movement, combined movements are considered as independent movement types as each of the single movements. However, based on the r values, all finger movements are linearly related, even with the condition-dependent components obtained from dPCA. In our real-time decoding results, we treated the two combined movements as independent conditions, and the accuracy for F12 and F23 (flexion of the combined fingers, overlapping conditions as in (Ben Hamed et al., 2007) using combined signals from area AIP, F5 and M1 was similar to the SM estimator accuracy reported.

A later study implanted a Utah array in the M1 hand region of one monkey and was able to decode flexion of the thumb, index and middle finger with 96% accuracy (Baker et al., 2009). Spikes were binned into a 150 ms window and fed to a Naïve Bayes classifier. The slightly higher decoding accuracy compared to our study (F1: 86%, F2: 78% and F3: 85% with signal from three areas) could be due to the higher number of channels from Utah arrays, the longer time interval used for decoding (we decoded the go and the hold epoch separately with spikes binned in 40 ms windows), the less number of conditions (three in their study versus five in our study), the longer hold time (500 ms versus 100 ms), pre-selection of task relevant units based on 1-way ANOVA, and a slightly larger number of trials used for training the classifier. The same research group later reported an offline decoding result with nine different finger movements (flexion and extension of the first three fingers except thumb extension, combined two-and three-finger flexion including non-adjacent F13) with a performance of 84.7% using receiver operating characteristic (ROC) based majority-voting (Egan et al., 2012). The non-adjacent flexion F13 and the three-finger flexion F123 were finger movements not reported elsewhere. It was a pity that during the 66 sessions in this study, there was only an average of 3.3 movement types per session, and some of the cues were given in blocks instead of pseudorandomly. In addition, there was only one monkey trained. All these indicated difficulties of training macaque monkeys to perform finger movement tasks.

To our knowledge, we demonstrated the first time using neural signals from area AIP and F5 to decode individuated and combined finger movements offline, as well as in real-time. Previous studies have shown the possibility of using these areas to decode grip types (Townsend et al., 2011), continuous kinematics of the arm and the hand (Menz et al., 2015), and different objects being grasped (Schaffelhofer et al., 2015). AIP and F5 are therefore potential brain areas additional to M1 that could be used to control hand prostheses.

4.7 Conclusions and outlook

The M1 neuronal discharge patterns during individuated finger movements are diverse and heterogeneous (Poliakov and Schieber, 1999). Decoding studies of individuated finger movements successfully "read out" the movements from the M1 neuronal population (Ben Hamed et al., 2007; Baker et al., 2009; Egan et al., 2012), but the brain is still like a "black box" and the knowledge of how finger movements are encoded is limited (Poliakov and Schieber, 1999; Schieber and Santello, 2004). With analysis at the population level, considering each neuron as one dimension, we were able to visualize and compare the different finger flexion movements as neural trajectories in a state-space. Due to the complex activation pattern of the multitendoned muscles controlling finger movements, moving two fingers simultaneously is not the same as raising two arms together. The brain encodes a two-finger flexion as a unique movement type just as a single-finger movement, not by summing the movement signals of the two corresponding single fingers.

Studying how individuated finger movements are encoded in the brain is challenging mainly because of two reasons. First, comparing humans and macaque monkeys, individuated finger movements in these two species are both behaviorally and physiologically different. The degrees of independence of the fingers during manipulation of objects in monkeys are lower than during typing or playing piano in humans (Schieber and Santello, 2004). Although individuated finger movements of monkeys could be trained in experimental setups (Schieber, 1991; Baker et al., 2009), a grip type involving individuation of a single finger was hardly observed from semi-

free ranging individuals (Macfarlane and Graziano, 2009). The differences between the macaque extensor digiti quarti et quinti and the human homologue extensor digiti quinti proprious is the most representative example for anatomical differences (Schieber et al., 1997). Therefore, one could argue how much we can learn by recording neural signals from experimentally trained animals. Second, due to the first reason, training individuated finger movements in monkeys is difficult (Schieber, 1991), compared to other motor tasks such as reaching or grasping. The physiological constrains of moving fingers independently makes it hard to distinguish during training whether an animal does not understand the abstract cues indicating different movements or moving fingers independently requires such a high level of attention that during a normal training session, it is hard to achieve a behavioral successful rate comparable to other motor tasks.

Therefore, it will be helpful that future researches collect neural data of individuated finger movements from human patients either with electrocorticography (ECoG) or microelectrode arrays. Currently, recording human ECoG signal seems to be the only possibility to understand how the brain controls fingers at the full physiological range of individuation. Microelectrode array recordings from paralyzed patients are crucial for investigating the possibility of controlling a dexterous hand prosthesis with higher numbers of DOFs than the existing 1-DOF closing and opening. Our study demonstrated the neural representation of individual finger movements in macaque area AIP, F5 and M1, and the possibility of real-time decoding using neural signals from these areas.

Reference

Afshar A, Santhanam G, Yu BM, Ryu SI, Sahani M, Shenoy KV (2011) Single-trial neural correlates of arm movement preparation. Neuron 71:555–564.

Aggarwal V, Acharya S, Tenore F, Shin H-C, Etienne-Cummings R, Schieber MH, Thakor NV (2008) Asynchronous decoding of dexterous finger movements using M1 neurons. IEEE Trans Neural Syst Rehabil Eng 16:3–14.

Aggarwal V, Tenore F, Acharya S, Schieber MH, Thakor NV (2009) Cortical decoding of individual finger and wrist kinematics for an upper-limb neuroprosthesis. Conf Proc IEEE Eng Med Biol Soc 2009:4535–4538.

Ames KC, Ryu SI, Shenoy KV (2014) Neural dynamics of reaching following incorrect or absent motor preparation. Neuron 81:438–451.

Andersen P, Hagan PJ, Phillips CG, Powell TP (1975) Mapping by microstimulation of overlapping projections from area 4 to motor units of the baboon's hand. Proc R Soc Lond, B, Biol Sci 188:31–36.

Anderson KD (2004) Targeting recovery: priorities of the spinal cord-injured population. J Neurotrauma 21:1371–1383.

Baker J, Bishop W, Kellis S, Levy T, House P, Greger B (2009) Multi-scale recordings for neuroprosthetic control of finger movements. Conf Proc IEEE Eng Med Biol Soc 2009:4573–4577.

Baker JJ, Scheme E, Englehart K, Hutchinson DT, Greger B (2010) Continuous detection and decoding of dexterous finger flexions with implantable myoelectric sensors. IEEE Trans Neural Syst Rehabil Eng 18:424–432.

Barlow HB (1972) Single units and sensation: a neuron doctrine for perceptual psychology? Perception 1:371–394.

Batista AP, Buneo CA, Snyder LH, Andersen RA (1999) Reach plans in eye-centered coordinates. Science 285:257–260.

Baumann MA, Fluet M-C, Scherberger H (2009) Context-specific grasp movement representation in the macaque anterior intraparietal area. J Neurosci 29:6436–6448.

Beisteiner R, Windischberger C, Lanzenberger R, Edward V, Cunnington R, Erdler M, Gartus A, Streibl B, Moser E, Deecke L (2001) Finger somatotopy in human motor cortex. NeuroImage 13:1016–1026.

Belmalih A, Borra E, Contini M, Gerbella M, Rozzi S, Luppino G (2009) Multimodal architectonic subdivision of the rostral part (area F5) of the macaque ventral premotor cortex. J Comp Neurol 512:183–217.

Ben Hamed S, Schieber MH, Pouget A (2007) Decoding M1 neurons during multiple finger movements. J Neurophysiol 98:327–333.

Bonini L, Serventi FU, Simone L, Rozzi S, Ferrari PF, Fogassi L (2011) Grasping neurons of monkey parietal and premotor cortices encode action goals at distinct levels of abstraction during complex action sequences. J Neurosci 31:5876–5886.

Bonini L, Ugolotti Serventi F, Bruni S, Maranesi M, Bimbi M, Simone L, Rozzi S, Ferrari PF, Fogassi L (2012) Selectivity for grip type and action goal in macaque inferior parietal and ventral premotor grasping neurons. J Neurophysiol 108:1607–1619.

Borra E, Belmalih A, Calzavara R, Gerbella M, Murata A, Rozzi S, Luppino G (2008) Cortical connections of the macaque anterior intraparietal (AIP) area. Cereb Cortex 18:1094–1111.

Borra E, Belmalih A, Gerbella M, Rozzi S, Luppino G (2010) Projections of the hand field of the macaque ventral premotor area F5 to the brainstem and spinal cord. J Comp Neurol 518:2570–2591.

Borra E, Gerbella M, Rozzi S, Luppino G (2017) The macaque lateral grasping network: A neural substrate for generating purposeful hand actions. Neurosci Biobehav Rev 75:65–90.

Bremner FD, Baker JR, Stephens JA (1991) Variation in the degree of synchronization exhibited by motor units lying in different finger muscles in man. J Physiol 432:381–399.

Brochier T, Boudreau MJ, Paré M, Smith AM (1999) The effects of muscimol inactivation of small regions of motor and somatosensory cortex on independent finger movements and force control in the precision grip. Exp Brain Res 128:31–40.

Buneo CA, Jarvis MR, Batista AP, Andersen RA (2002) Direct visuomotor transformations for reaching. Nature 416:632–636.

Buys EJ, Lemon RN, Mantel GW, Muir RB (1986) Selective facilitation of different hand muscles by single corticospinal neurones in the conscious monkey. J Physiol 381:529–549.

Buzsáki G (2004) Large-scale recording of neuronal ensembles. Nat Neurosci 7:446–451.

Buzsáki G (2010) Neural syntax: cell assemblies, synapsembles, and readers. Neuron 68:362–385.

Cheney PD, Fetz EE (1985) Comparable patterns of muscle facilitation evoked by individual corticomotoneuronal (CM) cells and by single intracortical microstimuli in primates: evidence for functional groups of CM cells. J Neurophysiol 53:786–804.

Cheney PD, Fetz EE, Palmer SS (1985) Patterns of facilitation and suppression of antagonist forelimb muscles from motor cortex sites in the awake monkey. J Neurophysiol 53:805–820.

Churchland MM et al. (2010a) Stimulus onset quenches neural variability: a widespread cortical phenomenon. Nat Neurosci 13:369–378.

Churchland MM, Cunningham JP, Kaufman MT, Foster JD, Nuyujukian P, Ryu SI, Shenoy KV (2012) Neural population dynamics during reaching. Nature 487:51–56.

Churchland MM, Cunningham JP, Kaufman MT, Ryu SI, Shenoy KV (2010b) Cortical preparatory activity: representation of movement or first cog in a dynamical machine? Neuron 68:387–400.

Churchland MM, Shenoy KV (2007) Temporal complexity and heterogeneity of single-neuron activity in premotor and motor cortex. J Neurophysiol 97:4235–4257.

Collinger JL, Wodlinger B, Downey JE, Wang W, Tyler-Kabara EC, Weber DJ, McMorland AJ, Velliste M, Boninger ML, Schwartz AB (2013) High-performance neuroprosthetic control by an individual with tetraplegia. Lancet 381:557–564.

Cunningham JP, Yu BM (2014) Dimensionality reduction for large-scale neural recordings. Nat Neurosci 17:1500–1509.

Dann B, Michaels JA, Schaffelhofer S, Scherberger H (2016) Uniting functional network topology and oscillations in the fronto-parietal single unit network of behaving primates. ELife 5:2870.

Datta AK, Farmer SF, Stephens JA (1991) Central nervous pathways underlying synchronization of human motor unit firing studied during voluntary contractions. J Physiol 432:401–425.

Davare M, Kraskov A, Rothwell JC, Lemon RN (2011) Interactions between areas of the cortical grasping network. Curr Opin Neurobiol 21:565–570.

Denk W, Strickler J, Webb W (1990) Two-photon laser scanning fluorescence microscopy. Science 248:73–76.

Donoghue JP, Leibovic S, Sanes JN (1992) Organization of the forelimb area in squirrel monkey motor cortex: representation of digit, wrist, and elbow muscles. Exp Brain Res 89:1–19.

Donoghue JP, Nurmikko A, Black M, Hochberg LR (2007) Assistive technology and robotic control using motor cortex ensemble-based neural interface systems in humans with tetraplegia. J Physiol 579:603–611.

Egan J, Baker J, House PA, Greger B (2012) Decoding dexterous finger movements in a neural prosthesis model approaching real-world conditions. IEEE Trans Neural

Syst Rehabil Eng 20:836–844.

Elsayed GF, Cunningham JP (2017) Structure in neural population recordings: an expected byproduct of simpler phenomena? Nat Neurosci 20:1310–1318.

Engel KC, Flanders M, Soechting JF (1997) Anticipatory and sequential motor control in piano playing. Exp Brain Res 113:189–199.

Evangeliou MN, Raos V, Galletti C, Savaki HE (2009) Functional imaging of the parietal cortex during action execution and observation. Cereb Cortex 19:624–639.

Fagg AH, Arbib MA (1998) Modeling parietal-premotor interactions in primate control of grasping. Neural Netw 11:1277–1303.

Farina D, Holobar A, Merletti R, Enoka RM (2010) Decoding the neural drive to muscles from the surface electromyogram. Clin Neurophysiol 121:1616–1623.

Fattori P, Breveglieri R, Raos V, Bosco A, Galletti C (2012) Vision for action in the macaque medial posterior parietal cortex. J Neurosci 32:3221–3234.

Fattori P, Kutz DF, Breveglieri R, Marzocchi N, Galletti C (2005) Spatial tuning of reaching activity in the medial parieto-occipital cortex (area V6A) of macaque monkey. Eur J Neurosci 22:956–972.

Feix T, Romero J, Schmiedmayer H-B, Dollar AM, Kragic D (2016) The GRASP taxonomy of human grasp types. IEEE Trans Human-Mach Syst 46:66–77.

Fetz EE, Cheney PD (1980) Postspike facilitation of forelimb muscle activity by primate corticomotoneuronal cells. J Neurophysiol 44:751–772.

Fish J, Soechting JF (1992) Synergistic finger movements in a skilled motor task. Exp Brain Res 91:327–334.

Fitzgerald PJ, Lane JW, Thakur PH, Hsiao SS (2004) Receptive field properties of the macaque second somatosensory cortex: evidence for multiple functional representations. J Neurosci 24:11193–11204.

Fluet M-C, Baumann MA, Scherberger H (2010) Context-specific grasp movement representation in macaque ventral premotor cortex. J Neurosci 30:15175–15184.

Fogassi L, Gallese V, Buccino G, Craighero L, Fadiga L, Rizzolatti G (2001) Cortical mechanism for the visual guidance of hand grasping movements in the monkey: A reversible inactivation study. Brain 124:571–586.

Freedman DJ, Assad JA (2016) Neuronal mechanisms of visual categorization: an abstract view on decision making. Annu Rev Neurosci 39:129–147.

Freiwald WA, Tsao DY, Livingstone MS (2009) A face feature space in the macaque

temporal lobe. Nat Neurosci 12:1187–1196.

Gallese V, Murata A, Kaseda M, Niki N, Sakata H (1994) Deficit of hand preshaping after muscimol injection in monkey parietal cortex. Neuroreport 5:1525–1529.

Georgopoulos AP, Kalaska JF, Caminiti R, Massey JT (1982) On the relations between the direction of two-dimensional arm movements and cell discharge in primate motor cortex. J Neurosci 2:1527–1537.

Georgopoulos AP, Pellizzer G, Poliakov AV, Schieber MH (1999) Neural coding of finger and wrist movements. J Comput Neurosci 6:279–288.

Gerbella M, Belmalih A, Borra E, Rozzi S, Luppino G (2011) Cortical connections of the anterior (F5a) subdivision of the macaque ventral premotor area F5. Brain Struct Funct 216:43–65.

Goodale MA, Milner AD (1992) Separate visual pathways for perception and action. Trends Neurosci 15:20–25.

Gould HJ, Cusick CG, Pons TP, Kaas JH (1986) The relationship of corpus callosum connections to electrical stimulation maps of motor, supplementary motor, and the frontal eye fields in owl monkeys. J Comp Neurol 247:297–325.

Grafton ST (2010) The cognitive neuroscience of prehension: recent developments. Exp Brain Res 204:475–491.

Grynkiewicz G, Poenie M, Tsien RY (1985) A new generation of Ca2+ indicators with greatly improved fluorescence properties. J Biol Chem 260:3440–3450.

Häger-Ross C, Schieber MH (2000) Quantifying the independence of human finger movements: comparisons of digits, hands, and movement frequencies. J Neurosci 20:8542–8550.

Hebb DO (1949) The Organization of Behavior. New York: Wiley.

Hochberg LR, Bacher D, Jarosiewicz B, Masse NY, Simeral JD, Vogel J, Haddadin S, Liu J, Cash SS, van der Smagt P, Donoghue JP (2012) Reach and grasp by people with tetraplegia using a neurally controlled robotic arm. Nature 485:372–375.

Hong K-S, Aziz N, Ghafoor U (2018) Motor-commands decoding using peripheral nerve signals: a review. J Neural Eng:1–49.

Hoshi E, Shima K, Tanji J (1998) Task-dependent selectivity of movement-related neuronal activity in the primate prefrontal cortex. J Neurophysiol 80:3392–3397.

Hubel DH (1957) Tungsten microelectrode for recording from single units. Science 125:549–550.

Hubel DH, Wiesel TN (1962) Receptive fields, binocular interaction and functional architecture in the cat's visual cortex. J Physiol 160:106–154.2.

Intveld RW, Dann B, Michaels JA, Scherberger H (2018) Neural coding of intended and executed grasp force in macaque areas AIP, F5, and M1. Sci Rep 8:17985.

Jackson A, Gee VJ, Baker SN, Lemon RN (2003) Synchrony between neurons with similar muscle fields in monkey motor cortex. Neuron 38:115–125.

Janssen P, Scherberger H (2015) Visual guidance in control of grasping. Annu Rev Neurosci 38:69–86.

Jeannerod M (1986) The formation of finger grip during prehension. A cortically mediated visuomotor pattern. Behav Brain Res 19:99–116.

Kakei S, Hoffman DS, Strick PL (1999) Muscle and movement representations in the primary motor cortex. Science 285:2136–2139.

Kandel E, Schwartz J, Jessell T, Siegelbaum S, Hudspeth AJ (2013) Principles of neural science. New York: McGraw-Hill.

Kaufman MT, Churchland MM, Ryu SI, Shenoy KV (2014) Cortical activity in the null space: permitting preparation without movement. Nat Neurosci 17:440–448.

Kaufman MT, Churchland MM, Ryu SI, Shenoy KV (2015) Vacillation, indecision and hesitation in moment-by-moment decoding of monkey motor cortex. ELife 4:e04677–21.

Kilbreath SL, Gandevia SC (1994) Limited independent flexion of the thumb and fingers in human subjects. J Physiol 479:487–497.

Kimura D, Vanderwolf CH (1970) The relation between hand preference and the performance of individual finger movements by left and right hands. Brain 93:769–774.

Kirsch E, Rivlis G, Schieber MH (2014) Primary motor cortex neurons during individuated finger and wrist movements: correlation of spike firing rates with the motion of individual digits versus their principal components. Front Neurol 5:70.

Ko H, Hofer SB, Pichler B, Buchanan KA, Sjöström PJ, Mrsic-Flogel TD (2011) Functional specificity of local synaptic connections in neocortical networks. Nature 473:87–91.

Kobak D, Brendel W, Constantinidis C, Feierstein CE, Kepecs A, Mainen ZF, Qi X-L, Romo R, Uchida N, Machens CK (2016) Demixed principal component analysis of neural population data. ELife 5:9424.

Komatsu H, Ideura Y (1993) Relationships between color, shape, and pattern selectivities of neurons in the inferior temporal cortex of the monkey. J Neurophysiol 70:677–694.

Kubánek J, Miller KJ, Ojemann JG, Wolpaw JR, Schalk G (2009) Decoding flexion of

individual fingers using electrocorticographic signals in humans. J Neural Eng 6:066001–066015.

Kubota K (1996) Motor cortical muscimol injection disrupts forelimb movement in freely moving monkeys. Neuroreport 7:2379–2384.

Lang CE, Schieber MH (2003) Differential impairment of individuated finger movements in humans after damage to the motor cortex or the corticospinal tract. J Neurophysiol 90:1160–1170.

Lawrence DG, Kuypers HGJM (1968) The functional organization of the motor system in the monkey I. The effects of the bilateral pyramidal lesions. Brain 91:1–14.

Lehmann SJ, Scherberger H (2013) Reach and gaze representations in macaque parietal and premotor grasp areas. J Neurosci 33:7038–7049.

Liao K, Xiao R, Gonzalez J, Ding L (2014) Decoding individual finger movements from one hand using human EEG signals. PLoS ONE 9:e85192.

Luppino G, Murata A, Govoni P, Matelli M (1999) Largely segregated parietofrontal connections linking rostral intraparietal cortex (areas AIP and VIP) and the ventral premotor cortex (areas F5 and F4). Exp Brain Res 128:181–187.

Luppino G, Rizzolatti G (2000) The organization of the frontal motor cortex. Physiology 15:219–224.

Macfarlane NBW, Graziano MSA (2009) Diversity of grip in Macaca mulatta. Exp Brain Res 197:255–268.

Machens CK, Romo R, Brody CD (2010) Functional, but not anatomical, separation of "what" and “when” in prefrontal cortex. J Neurosci 30:350–360.

Mante V, Sussillo D, Shenoy KV, Newsome WT (2013) Context-dependent computation by recurrent dynamics in prefrontal cortex. Nature 503:78–84.

Maranesi M, Rodà F, Bonini L, Rozzi S, Ferrari PF, Fogassi L, Coudé G (2012) Anatomo-functional organization of the ventral primary motor and premotor cortex in the macaque monkey. Eur J Neurosci 36:3376–3387.

Mason CR, Gomez JE, Ebner TJ (2001) Hand synergies during reach-to-grasp. J Neurophysiol 86:2896–2910.

Maunsell JH, Van Essen DC (1983) Functional properties of neurons in middle temporal visual area of the macaque monkey. I. Selectivity for stimulus direction, speed, and orientation. J Neurophysiol 49:1127–1147.

Menz VK, Schaffelhofer S, Scherberger H (2015) Representation of continuous hand and arm movements in macaque areas M1, F5, and AIP: a comparative decoding study. J Neural Eng 12:056016–056020.

Michaels JA, Scherberger H (2018) Population coding of grasp and laterality-related information in the macaque fronto-parietal network. Sci Rep 8:1710.

Murata A, Fadiga L, Fogassi L, Gallese V, Raos V, Rizzolatti G (1997) Object representation in the ventral premotor cortex (area F5) of the monkey. J Neurophysiol 78:2226–2230.

Murata A, Gallese V, Kaseda M, Sakata H (1996) Parietal neurons related to memory-guided hand manipulation. J Neurophysiol 75:2180–2186.

Murata A, Gallese V, Luppino G, Kaseda M, Sakata H (2000) Selectivity for the shape, size, and orientation of objects for grasping in neurons of monkey parietal area AIP. J Neurophysiol 83:2580–2601.

Murray EA, Bussey TJ, Wise SP (2000) Role of prefrontal cortex in a network for arbitrary visuomotor mapping. Exp Brain Res 133:114–129.

Musallam S, Bak MJ, Troyk PR, Andersen RA (2007) A floating metal microelectrode array for chronic implantation. J Neurosci Methods 160:122–127.

Nicolelis MAL, Dimitrov D, Carmena JM, Crist R, Lehew G, Kralik JD, Wise SP (2003) Chronic, multisite, multielectrode recordings in macaque monkeys. Proc Natl Acad Sci U S A 100:11041–11046.

Nicolelis MAL, Lebedev MA (2009) Principles of neural ensemble physiology underlying the operation of brain-machine interfaces. Nat Rev Neurosci 10:530–540.

Nordhausen CT, Maynard EM, Normann RA (1996) Single unit recording capabilities of a 100 microelectrode array. Brain Res 726:129–140.

Norman J (2003) Two visual systems and two theories of perception: An attempt to reconcile the constructivist and ecological approaches. Behav Brain Sci:1–72.

Öğmen H, Ekiz O, Huynh D, Bedell HE, Tripathy SP (2013) Bottlenecks of motion processing during a visual glance: the leaky flask model. PLoS ONE 8:e83671.

Perry CJ, Fallah M (2014) Feature integration and object representations along the dorsal stream visual hierarchy. Front Comput Neurosci 8:1–17.

Pettigrew JP, Sandersonand KJ, Levick WR (1986) Visual Neuroscience. Cambridge University Press.

Poliakov AV, Schieber MH (1999) Limited functional grouping of neurons in the motor cortex hand area during individuated finger movements: A cluster analysis. J Neurophysiol 82:3488–3505.

Porter R (1985) The corticomotoneuronal component of the pyramidal tract: corticomotoneuronal connections and functions in primates. Brain Res 357:1–26.

Rajalingham R, Musallam S (2017) Characterization of neurons in the primate medial intraparietal area reveals a joint representation of intended reach direction and amplitude. PLoS ONE 12:e0182519.

Raos V, Umiltá M-A, Murata A, Fogassi L, Gallese V (2006) Functional properties of grasping-related neurons in the ventral premotor area F5 of the macaque monkey. J Neurophysiol 95:709–729.

Reilly KT, Schieber MH (2003) Incomplete functional subdivision of the human multitendoned finger muscle flexor digitorum profundus: an electromyographic study. J Neurophysiol 90:2560–2570.

Rizzolatti G, Camarda R, Fogassi L, Gentilucci M, Luppino G, Matelli M (1988) Functional organization of inferior area 6 in the macaque monkey. Exp Brain Res 71:491–507.

Rizzolatti G, Luppino G (2001) The cortical motor system. Neuron 31:889–901.

Romero MC, Pani P, Janssen P (2014) Coding of shape features in the macaque anterior intraparietal area. J Neurosci 34:4006–4021.

Romero MC, Van Dromme ICL, Janssen P (2013) The role of binocular disparity in stereoscopic images of objects in the macaque anterior intraparietal area. PLoS ONE 8:e55340.

Rossini PM, Micera S, Benvenuto A, Carpaneto J, Cavallo G, Citi L, Cipriani C, Denaro L, Denaro V, Di Pino G, Ferreri F, Guglielmelli E, Hoffmann K-P, Raspopovic S, Rigosa J, Rossini L, Tombini M, Dario P (2010) Double nerve intraneural interface implant on a human amputee for robotic hand control. Clin Neurophysiol 121:777–783.

Rousche PJ, Normann RA (1998) Chronic recording capability of the Utah Intracortical Electrode Array in cat sensory cortex. J Neurosci Methods 82:1–15.

Sadtler PT, Quick KM, Golub MD, Chase SM, Ryu SI, Tyler-Kabara EC, Yu BM, Batista AP (2014) Neural constraints on learning. Nature 512:423–426.

Sakata H, Taira M, Murata A, Mine S (1995) Neural mechanisms of visual guidance of hand action in the parietal cortex of the monkey. Cereb Cortex 5:429–438.

Sanes J, Donoghue J, Thangaraj V, Edelman R, Warach S (1995) Shared neural substrates controlling hand movements in human motor cortex. Science 268:1775–1777.

Santello M, Flanders M, Soechting JF (1998) Postural hand synergies for tool use. J Neurosci 18:10105–10115.

Schaffelhofer S, Agudelo-Toro A, Scherberger H (2015) Decoding a wide range of hand configurations from macaque motor, premotor, and parietal cortices. J Neurosci 35:1068–1081.

Schaffelhofer S, Scherberger H (2016) Object vision to hand action in macaque parietal, premotor, and motor cortices. ELife 5:6436.

Scherberger H (2009) Neural control of motor prostheses. Curr Opin Neurobiol 19:629–633.

Schieber MH (1991) Individuated finger movements of rhesus monkeys: a means of quantifying the independence of the digits. J Neurophysiol 65:1381–1391.

Schieber MH (1995) Muscular production of individuated finger movements: the roles of extrinsic finger muscles. J Neurosci 15:284–297.

Schieber MH (1999) Somatotopic gradients in the distributed organization of the human primary motor cortex hand area: evidence from small infarcts. Exp Brain Res 128:139–148.

Schieber MH (2001) Constraints on somatotopic organization in the primary motor cortex. J Neurophysiol 86:2125–2143.

Schieber MH (2004) Motor control: basic units of cortical output? Curr Biol 14:R353–R354.

Schieber MH (2011) Dissociating motor cortex from the motor. J Physiol 589:5613–5624.

Schieber MH, Chua M, Petit J, Hunt CC (1997) Tension distribution of single motor units in multitendoned muscles: comparison of a homologous digit muscle in cats and monkeys. J Neurosci 17:1734–1747.

Schieber MH, Hibbard LS (1993) How somatotopic is the motor cortex hand area? Science 261:489–492.

Schieber MH, Poliakov AV (1998) Partial inactivation of the primary motor cortex hand area: effects on individuated finger movements. J Neurosci 18:9038–9054.

Schieber MH, Santello M (2004) Hand function: peripheral and central constraints on performance. J Appl Physiol 96:2293–2300.

Sejnowski TJ, Churchland PS, Movshon JA (2014) Putting big data to good use in neuroscience. Nat Neurosci 17:1440–1441.

Serlin DM, Schieber MH (1993) Morphologic regions of the multitendoned extrinsic finger muscles in the monkey forearm. Acta Anat (Basel) 146:255–266.

Shaikhouni A, Annetta NV, Bockbrader MA, Friedenberg DA, Nielson DM, Sederberg PB, Glenn BC, Mysiw WJ, Morgan AG, Deogaonkar M, Rezai AR, Bouton CE, Sharma G (2016) Restoring cortical control of functional movement in a human with quadriplegia. Nature 533:247–250.

Sherrington CS (1906) Observations on the scratch-reflex in the spinal dog. J Physiol

34:1–50.

Shinoda Y, Zarzecki P, Asanuma H (1979) Spinal branching of pyramidal tract neurons in the monkey. Exp Brain Res 34:59–72.

Srivastava S, Orban GA, De Mazière PA, Janssen P (2009) A distinct representation of three-dimensional shape in macaque anterior intraparietal area: fast, metric, and coarse. J Neurosci 29:10613–10626.

Taira M, Mine S, Georgopoulos AP, Murata A, Sakata H (1990) Parietal cortex neurons of the monkey related to the visual guidance of hand movement. Exp Brain Res 83:29–36.

Takahashi K, Best MD, Huh N, Brown KA, Tobaa AA, Hatsopoulos NG (2017) Encoding of both reaching and grasping kinematics in dorsal and ventral premotor cortices. J Neurosci 37:1733–1746.

Taylor DM, Tillery SIH, Schwartz AB (2002) Direct cortical control of 3D neuroprosthetic devices. Science 296:1829–1832.

Tenore FVG, Ramos A, Fahmy A, Acharya S, Etienne-Cummings R, Thakor NV (2009) Decoding of individuated finger movements using surface electromyography. IEEE Trans Biomed Eng 56:1427–1434.

Theys T, Pani P, van Loon J, Goffin J, Janssen P (2012) Selectivity for three-dimensional shape and grasping-related activity in the macaque ventral premotor cortex. J Neurosci 32:12038–12050.

Theys T, Pani P, van Loon J, Goffin J, Janssen P (2013) Three-dimensional shape coding in grasping circuits: a comparison between the anterior intraparietal area and ventral premotor area F5a. J Cogn Neurosci 25:352–364.

Todorov E (2000) Direct cortical control of muscle activation in voluntary arm movements: a model. Nat Neurosci 3:391–398.

Townsend BR, Subasi E, Scherberger H (2011) Grasp movement decoding from premotor and parietal cortex. J Neurosci 31:14386–14398.

Umilta MA, Escola L, Intskirveli I, Grammont F, Rochat M, Caruana F, Jezzini A, Gallese V, Rizzolatti G (2008) When pliers become fingers in the monkey motor system. Proc Natl Acad Sci USA 105:2209–2213.

Umilta MA, Kohler E, Gallese V, Fogassi L, Fadiga L, Keysers C, Rizzolatti G (2001) I know what you are doing. a neurophysiological study. Neuron 31:155–165.

Vargas-Irwin CE, Shakhnarovich G, Yadollahpour P, Mislow JMK, Black MJ, Donoghue JP (2010) Decoding complete reach and grasp actions from local primary motor cortex Populations. J Neurosci 30:9659–9669.

Velliste M, Perel S, Spalding MC, Whitford AS, Schwartz AB (2008) Cortical control of

a prosthetic arm for self-feeding. Nature 453:1098–1101.

Wallis JD, Anderson KC, Miller EK (2001) Single neurons in prefrontal cortex encode abstract rules. Nature 411:953–956.

Wessberg J, Stambaugh CR, Kralik JD, Beck PD, Laubach M, Chapin JK, Kim J, Biggs SJ, Srinivasan MA, Nicolelis MAL (2000) Real-time prediction of hand trajectory by ensembles of cortical neurons in primates. Nature 408:361–365.

Wilson JW (1947) Virchow's contribution to the cell theory. J Hist Med Allied Sci II:163–178.

Yu BM, Cunningham JP, Santhanam G, Ryu SI, Shenoy KV, Sahani M (2009) Gaussian-process factor analysis for low-dimensional single-trial analysis of neural population activity. J Neurophysiol 102:614–635.

Yuste R (2015) From the neuron doctrine to neural networks. Nat Neurosci 16:487–497.